

Quantum effects in Molecular Magnets

Zur Erlangung des akademischen Grades eines
DOKTORS DER NATURWISSENSCHAFTEN
von der KIT-Fakultät für Physik des
Karlsruher Instituts für Technologie (KIT)

genehmigte
Dissertation
von

M. Sc. Gheorghe Taran

Tag der mündlichen Prüfung: 23. October 2020
Referent: Prof. Dr. Wolfgang Wernsdorfer
Korreferent: Prof. Dr. Mario Ruben

for Eliza

Contents

| | | |
|----------|--|------------|
| 1 | Introduction | 1 |
| 1.1 | Spin Hamiltonian Formalism | 6 |
| 1.2 | Quantum Tunneling of Magnetization | 15 |
| 1.3 | Spin Parity and Quantum Phase Interference | 18 |
| 1.4 | Quantum Coherence in Molecular Magnets | 20 |
| 1.5 | Molecular Quantum Spintronics | 22 |
| 2 | Experimental Details | 25 |
| 3 | Tb³⁺ molecular magnets | 35 |
| 3.1 | The role of quadrupolar interaction in tunneling dynamics of TbPc ₂ SIMM | 35 |
| 3.2 | Decoherence Measurements in TbPc ₂ SIMM | 44 |
| 3.3 | Nuclear spin lattice relaxation | 56 |
| 3.4 | Electronic and nuclear spin dynamics in Tb ₂ Pc ₃ dinuclear SMM | 65 |
| 4 | Hyperfine enhanced phonon assisted tunneling | 73 |
| 4.1 | Dy ₂ dpm isotopologue SMMs | 75 |
| 4.2 | Phonon assisted tunneling in Ho ^{III} F ₂ [15-MC _{Ni} -5] | 84 |
| 4.3 | Phonon assisted tunneling in Mn ₁₂ -ac | 90 |
| 5 | μSQUID-EPR on Gd³⁺ SIMMs | 101 |
| 5.1 | Et ₄ N[¹⁶⁰ GdPc ₂] SIMM | 102 |
| 5.2 | Measurements on ¹⁵⁷ Gd(tmhd) ₃ Phen | 119 |
| 6 | Conclusions and Outlook | 123 |
| | Bibliography | 127 |
| | List of Publications | 143 |
| | Acknowledgements | 145 |

1 Introduction

Traditionally, the word *magnet* evokes a material in which a long-range magnetic order arises from local exchange interactions. The observed magnetic properties, like remanence and hysteresis, result from a collective behavior. However, developments in the last two decades showed that isolated molecules can bear large magnetic moments that exhibit bistability like traditional magnets. They have therefore been called single-molecule magnets (SMMs).

The field of SMMs started with the discovery of the large magnetic moment of the $\text{Mn}_{12}\text{O}_{12}(\text{CH}_3\text{COO})_{16}(\text{H}_2\text{O})_4$ (here denoted as $\text{Mn}_{12}\text{-ac}$, Fig. 1.1) molecular cluster [1] and the observation of its magnetic bistability [2]. Later, quantum tunneling of magnetization (QTM) [3, 4] was evidenced in $\text{Mn}_{12}\text{-ac}$, as well as ground state quantum tunneling [5] and topological quantum phase interference effects [6] in $[\text{Fe}_8\text{O}_2(\text{OH})_{12}(\text{tacn})_6]^{8+}$ (or simply Fe_8 , Fig. 1.1). These first discovered SMMs lead to breakthrough observations and to this day remain amongst the most investigated systems [7, 8].

SMMs are constituted by an inner core of magnetic ions which is surrounded by a shell of organic ligands. They come in a variety of shapes and sizes and permit selective substitution of the ligands in order to alter the coupling to the environment. It is also possible to replace the magnetic ions, thus changing the magnetic properties without greatly modifying the structure and the interaction with its surroundings.

The main technological interest in the field of SMMs is fueled by the desire to integrate molecular structures in quantum information processing devices as memory units and quantum bits (qubits). There are currently two different approaches that try to satisfy the miniaturization tendencies in the current state of the art technology. The first one is a top-down approach in which the nanometer-sized objects are obtained by reducing the dimensions of a bulk material (a common way for obtaining magnetic nanoparticles). The second method is a bottom-up approach [9] which for the field of SMMs means enhancing the magnetic moment of the molecule by ion substitution or through adding new magnetic centres to the molecule. One big advantage of SMMs over magnetic nanoparticles is their monodisperse properties, as chemical synthesis yields a large number of molecules with identical characteristics.

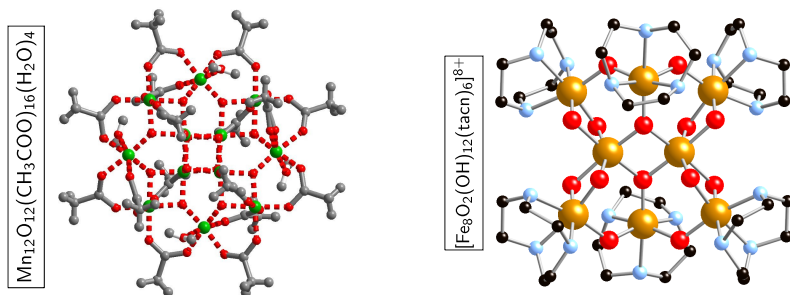


Figure 1.1: *Left:* Structure of the Mn₁₂ SMM with the formula [Mn₁₂O₁₂(CH₃COO)₁₆(H₂O)₄]. *Right:* Structure of the Fe₈ SMM with the formula [Fe₈O₂(OH)₁₂(tacn)₆]⁸⁺ where tacn is a macrocyclic ligand.

In many cases, the SMMs can be made to form insulating monocrystals, thus the environment of each molecule is very similar. This gives access to the properties of a single molecule from the measurements performed on the ensemble. The found alignment between the magnetic principal axis of the molecule and the crystallographic axes [10] is especially important when determining the intrinsic characteristics of the magnetic centres.

Most of the earlier experimental and theoretical investigations of the physics of molecular magnets were done using 3d transition metal ion complexes as model systems. However, the last decade saw the rise of molecular complexes that employ lanthanide ions as magnetic centers and at the moment one can make an argument that this class of SMMs are amongst the most promising ones. Recent achievements include the observation of magnetic bistability of a Dy complex at temperatures well above liquid nitrogen [11] and the implementation of the quantum Grover algorithm at the single molecule level [12]. Unquenched orbital angular momentum, large single ion anisotropy and a strong hyperfine interaction are just some characteristics that distinguish lanthanide complexes in the field of molecular magnetism [13].

In this thesis I discuss measurements on lanthanide single-molecule magnets model systems that we used to explore quantum phenomenologies at mesoscopic scale (referring to the vector space associated with the spin degree of freedom) where properties from both the quantum and the classical worlds transpire. The interest of working in this dimensional range comes from the desire to use quantum properties that characterize microscopic systems while being able to address and manipulate them with simple means.

I start with a short account of the dominant intramolecular interactions at sub-Kelvin temperatures in the framework of spin Hamiltonian models. The application of the general formalism to mononuclear and polynuclear complexes is used to illustrate

the power of the spin models in explaining both static properties (e.g., magnetic bistability) and dynamic ones (e.g., quantum tunneling of magnetization). I show how SMMs were used as a vehicle to explore quantum phenomenologies like nonadiabatic spin transitions, spin parity effect, Berry phase interference and quantum coherence while covering milestone results that brought the field closer to providing basic components of quantum devices. In the last section of this introductory chapter I give a short overview of the recent achievements in the field of molecular spintronics that allowed the implementation of Grover's quantum algorithms at the single molecule level.

In chapter 2 an overview of the μ SQUID technique is given as most of the studies presented in the subsequent sections are based on sub-kelvin μ SQUID measurements. Details are given on our efforts towards the automation of the measurement protocol. I also discuss the inclusion of an EPR module used to induce resonant excitations in single-molecule crystals.

I continue by presenting our theoretical and experimental investigation of the archetypical TbPc_2 SMM taken as a prototype for other lanthanide molecular magnets that are considered as potential candidates for quantum information processing devices. After a short review of the low temperature magnetic properties of the TbPc_2 complex we take an in depth look at the factors that can promote quantum tunneling dynamics. We first show that the commonly considered transverse interactions originating in the ligand field and in the spin bath fail to explain the observed dynamics. Further analysis highlights the importance of the nuclear spin in quenching the transitions that do not conserve its magnitude. Finally, we propose through nuclear quadrupolar interaction a viable mechanism that mixes the hyperfine states.

In the next section is shown that low temperature magnetometry (in our case μ SQUID measurements) can be used to obtain the decoherence rates in crystals of molecular magnets, thus providing an alternative to resonant techniques. For this, we model the magnetic hysteresis loops of the TbPc_2 diluted in an isostructural, diamagnetic matrix and obtain the tunneling transition rates. The tunneling probabilities are analyzed in the framework of the recently proposed model for incoherent Landau-Zener dynamics leading to experimental estimates of both the intrinsic tunneling time and the dephasing time. The presented approach to measuring decoherence should be applied to molecular systems that show promise as quantum bits and thus, provide important feedback to further improve them by chemical methods.

We then investigate the thermalization of the ^{159}Tb nuclear spins. The acquired understanding on the TbPc_2 's Landau-Zener dynamics is used to develop a read out technique for the population of the hyperfine states. It was found that a direct

process that involves phonon modulation of the hyperfine interaction is sufficient to explain the magnitude of the determined relaxation rates. To our knowledge, this is the first time the direct link between the phonon bath and the nuclear spins was shown to dominate the relaxation of a nuclear spin embedded in a molecular magnet. The highlighted relaxation mechanism is important to explain the observed isotopic enhanced dynamics in lanthanide compounds and will be further discussed in Chap. 4.

In the last section of Chap. 3, measurements on a closely related dinuclear Ln SMM, $\text{Tb}_2\text{Pc}^{\text{Hx8}}\text{Pc}_2$, are used to illustrate that the phenomenologies uncovered in the previous sections are important to rationalize its dynamics. It is shown that the spin-spin interactions together with transverse ligand field interactions induce the reversal of the electronic spins at the hyperfine crossings that conserve the nuclear spin. While the quadrupolar interaction between the electronic and nuclear spins induces co-flipping events that do not conserve the nuclear spin moment. Also, the ^{159}Tb nuclear spins in the molecular environment of the $\text{Tb}_2\text{Pc}^{\text{Hx8}}\text{Pc}_2$ thermalize on the same time scale as when it is embedded in the TbPc_2 molecule. The observed quantum phenomenologies have to be accounted in potential applications of the $\text{Tb}_2\text{Pc}^{\text{Hx8}}\text{Pc}_2$ complex in spintronics devices.

In chapter 4 we pursue the relationship between the isotopic composition of the Ln ions and the relaxation of the molecular spins in crystalline environments. Two model systems are discussed: $\text{Dy}(\text{tmhd})_3)_2\text{bpm}$ and $\text{Ho}^{\text{III}}\text{F}_2[15\text{-MC}_{\text{Ni}}\text{-5}]$.

In the first section I will present our analysis on $(^{163}\text{Dy}(\text{tmhd})_3)_2\text{bpm}$ and $(^{164}\text{Dy}(\text{tmhd})_3)_2\text{bpm}$ isotopologues and highlight the strong effect of the nuclear spins on the relaxation dynamics in intermediate temperature range, that is, when molecular spin tunneling and phonon assisted transition rates are comparable.

To further explore, through experimental means, the effect of the nuclear spin on the phonon-assisted tunneling in Ln compounds, we also discuss our measurements on $\text{Ho}^{\text{III}}\text{F}_2[15\text{-MC}_{\text{Ni}}\text{-5}]$ SIMM. The advantage of $\text{Ho}^{\text{III}}\text{F}_2[15\text{-MC}_{\text{Ni}}\text{-5}]$ compared to $\text{Dy}(\text{tmhd})_3)_2\text{bpm}$ lies in the well resolved structure of the hyperfine steps and in the unusual ground state splitting due to the interaction between the Ho ion and Ni_5 metallocrown. While the disadvantage is the simplex natural abundance of ^{165}Ho nucleus that does not allow isotopic purification.

In the last section I explain the observed temperature and field dependence of the relaxation rate of the molecular spin through phonon assisted quantum tunneling dynamics enhanced by hyperfine fluctuations. I show that the relaxation channel between the nuclear spins and the phonon-bath through the modulation of the hyperfine interaction is key in understanding the dynamics of both $\text{Dy}(\text{tmhd})_3)_2\text{bpm}$ and $\text{Ho}^{\text{III}}\text{F}_2[15\text{-MC}_{\text{Ni}}\text{-5}]$.

The last chapter is devoted to resonant photon absorption in two Gd^{3+} SIMMs, namely, $\text{Et}_4\text{N}[\text{}^{160}\text{GdPc}_2]$ and $^{157}\text{Gd}(\text{tmhd})_3\text{Phen}$.

In particular, measurements on $\text{Et}_4\text{N}[\text{}^{160}\text{GdPc}_2]$ are used to display the power of the combined μSQUID and EPR techniques to rationalize the observed magnetic phenomenology while the investigation of $^{157}\text{Gd}(\text{tmhd})_3\text{Phen}$ showcases the potential of these measurements to establish magnetostructural correlations. The "high resolution" of the measured energy spectrum allows for a detailed analysis of the magnetism of the compounds through the spin Hamiltonian formalism.

1.1 Spin Hamiltonian Formalism

In this thesis, I will discuss quantum phenomenologies observed in mononuclear and dinuclear lanthanide single molecule magnets. Thus, it is useful to start with a short overview of the general properties of lanthanide complexes and summarize the basic theoretical framework in which their magnetic properties are investigated.

Ln^{3+} compounds

The general problem to consider is a magnetic center placed in a molecular environment and manipulated by DC and RF magnetic fields. The characteristic Hamiltonian can be written formally as:

$$\mathcal{H} = \mathcal{H}_0 + \mathcal{H}_{ee} + \mathcal{H}_{\text{SO}} + \mathcal{H}_{\text{LF}} \quad (1.1)$$

Where

$$\mathcal{H}_0 = \sum_k \left[\frac{1}{2m} (\mathbf{p}_k + e\mathbf{A})^2 + g_e \mu_B (\nabla \times \mathbf{A}) \cdot \mathbf{s}_k - \frac{Z^* e^2}{r_k} \right] \quad (1.2)$$

is the sum of hydrogen like terms that takes into account the effect of the hyperfine and Zeeman interaction through the magnetic potential, \mathbf{A} ,

$$\mathcal{H}_{ee} = \sum_{k < l} \frac{e^2}{r_{kl}} \quad (1.3)$$

is the interelectronic repulsion,

$$\mathcal{H}_{\text{SO}} = \sum_k \zeta(r_k) \mathbf{s}_k \cdot \mathbf{l}_k \quad (1.4)$$

is the spin orbit coupling and

$$\mathcal{H}_{\text{LF}} = -e \sum_k \int \frac{\rho(\mathbf{R})}{|\mathbf{R} - \mathbf{r}_i|} d\tau \quad (1.5)$$

is the ligand field interaction.

The Schrodinger equation, $\mathcal{H}\Psi = E\Psi$, does not know an analytical solution and thus, a perturbative approach [14] was developed to take advantage of the fact that the interactions highlighted in Eq. 1.1 operate on different energy scales (see also Fig. 1.3).

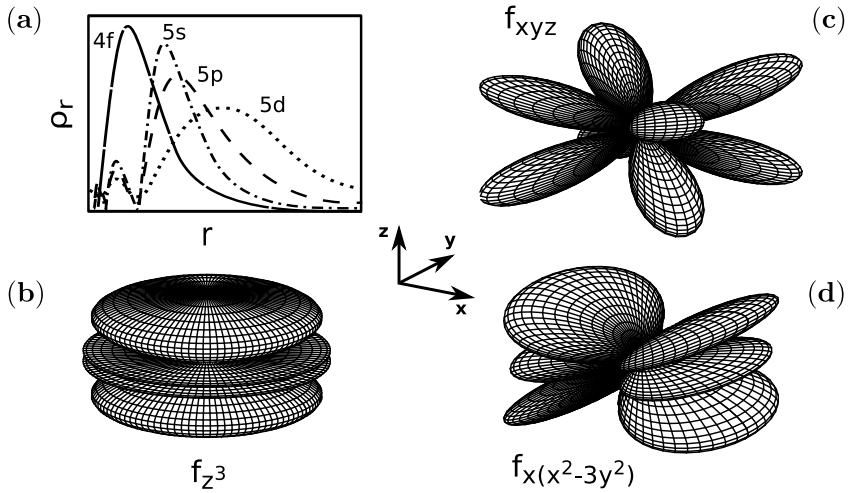


Figure 1.2: **a)** Schematic representation of the radial charge density ρ_r for the 5s, 5p, 4f and 5d electronic shells of the Gd^{3+} ion. The angular distribution of the 4f orbitals is depicted in panel **b)** f_{z^3} (similar to f_{x^3} , and f_{y^3} which extend along the x- and y-axes, instead). **c)** f_{xyz} (similar to $f_{xz^2-y^2}$, $f_{y(z^2-y^2)}$ and $f_{z(x^2-y^2)}$ which are produced by a 45° rotation about the x, y and z-axes respectively) and **d)** $f_x(x^2-3y^2)$ (similar to $f_{y(3x^2-y^2)}$ formed by a 90° clockwise rotation round the z-axis).

Thus, one solves $\mathcal{H}_0\Psi = E\Psi$ with $\mathbf{A} = 0$ Vs/m. The eigenfunctions are written as a product of hydrogen like wavefunctions:

$$\phi(\mathbf{r}) \sim r^{-1}R_{nl}(r)Y_l^m(\theta, \phi) \quad (1.6)$$

where R_{nl} and $Y_l^m(\theta, \phi)$ are the radial and angular dependence, respectively. The energy is a function of n and l only ($n = 4$ and $l = 3$ for the magnetic orbitals of the Ln ions). Thus, the lanthanide ions are characterized by the progressive filling of the 4f subshell, with the electronic configuration $[\text{Xe}]4f^n6s^2$ (or $[\text{Xe}]4f^{n-1}5d^16s^2$). Their distinct properties (e.g., prevalence of the +3 oxidation state, 4f contraction of the atomic radius, unquenched orbital angular momentum, relative easy ligand substitution, etc.) originate mainly in the well shielded nature of the magnetic electrons (Fig. 1.2a). Also, the angular distribution of the 4f orbitals (see Fig. 1.2b-d) plays an important role in determining the magnetic anisotropy of Ln^{3+} complexes. For example, it was used to explain why different ligation geometries lead to an either easy plane or easy axis anisotropy in a $\text{Ln}^{3+}\text{Pc}_2$ isostructural series [15].

For lanthanide ions the inter-electronic interaction is dominant over the spin-orbit interaction and thus Russel-Saunders coupling scheme is applied. That is, we first couple the electronic spin moments to a total spin angular momentum, S , and the

electronic orbital moments to a total orbital momentum, L . Thus, \mathcal{H}_{ee} interaction lifts the degeneracy of the $[\text{Xe}]4f^n$ ground states leading to terms of the form, ^{2S+1}L .

The total angular momentum, J , takes $2L + 1$ (if $L > S$) or $2S + 1$ (if $S > L$) degenerate values: $J = |L - S|, \dots, (L + S)$. The degeneracy is broken by taking into account the spin-orbit interaction:

$$\mathcal{H}_{SO} = \lambda \mathbf{S} \cdot \mathbf{L} \quad (1.7)$$

The states characterized by the same L , S and different J , are split according to the relation:

$$E(S, L; J) = \lambda/2[J(J + 1) - L(L + 1) - S(S + 1)] \quad (1.8)$$

with consecutive states separated by:

$$\Delta E = E(S, L; J + 1) - E(S, L; J) = \lambda J \quad (1.9)$$

where $\lambda = \pm \zeta/2S$, is positive for $n < 7$ and negative for $n > 7$. Thus, the ground state is $|L - S|$ for the Ln ions with less than half-filled shell and $(L + S)$ for the Ln ions with more than half-filled shell.

The procedure used to obtain the total angular momentum corresponding to the ground electronic state of a free Ln^{3+} ion are summarized by the Hund's rules, that should be applied in the following order:

- Between all possible electronic configurations, the ground state corresponds to states that maximizes S .
- L corresponds to the maximum allowed angular momentum.
- Finally, the total angular momentum is $|L - S|$ for $n < 7$ and $(L + S)$ for $n > 7$ with the term represented by $^{2S+1}L_J$.

Note that, the research field of molecular magnets is biased towards the elements in the second half of the lanthanide series due to their large total angular momentum and thus large magnetic moment. Also, for most Ln ions, the spin orbit coupling leads to a large separations between the ground, $^{2S+1}L_J$, and first excited term, $^{2S+1}L_{J+1}$, and thus at room temperature only the ground state is occupied.

Ligand field interaction

A lanthanide SMM contains a Ln^{3+} ion embedded in a molecular environment with the effect of the coordinated ions usually described in the framework of the ligand field formalism. The ligand field Hamiltonian, \mathcal{H}_{LF} (Eq. 1.5), describes an

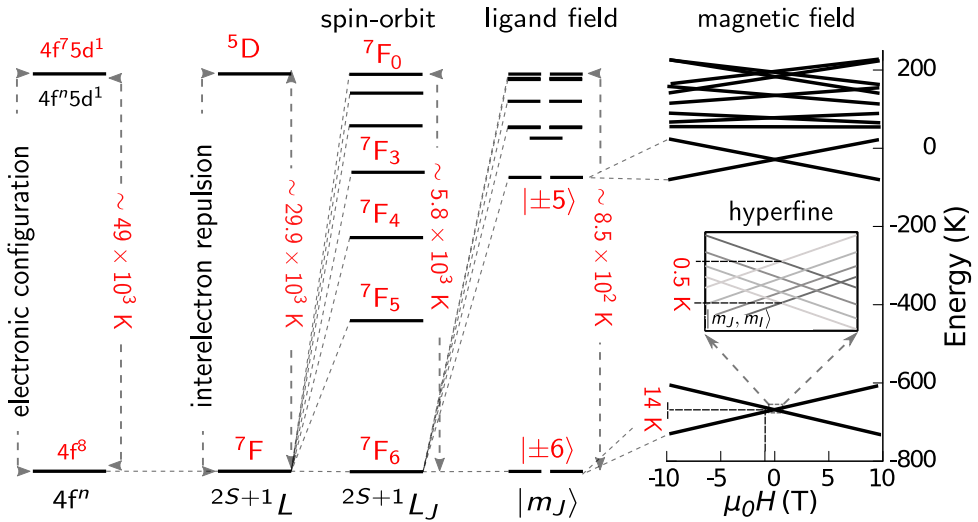


Figure 1.3: Schematic representation of the dominant intramolecular interactions in the TbPc₂ single molecule magnet. An excitation with energy larger than 49×10^3 K is needed to induce the $4f^8 - 4f^7 5d^1$ transition. In the LS-coupling scheme, the electrostatic repulsion results in the ground term, 7F , being separated by 29.9×10^3 K from the excited one, 5D . The degenerate states characterized by, $S = 3$, $L = 6$ and a total angular momentum, $J = 0, 1, \dots, 6$, are in turn split by the spin orbit coupling leading to the ground state term, 7F_6 , separated by ~ 2900 K from 7F_5 excited term. The degeneracy is further removed by the interaction with the ligand ions leading to a ground doublet $m_j = \pm 6$ separated by more than 600 K from the first excited one $m_j = \pm 5$. Finally, the ground doublet is split by the interaction with an externally applied field (e.g., 14 K energy splitting in $B_z = 10$ T) and by the interaction with the nuclear spin.

electrostatic potential created by the ligated ions. For molecular complexes this approximation is often not sufficient and covalent effects have to be included.

To evaluate the ligand field in a perturbative approach one has to compute the following matrix elements:

$$\langle \psi_l | \mathcal{H}_{LF} | \psi_k \rangle \quad (1.10)$$

Due to the spherical nature of the $|\psi\rangle$ eigenstates it is useful to expand the potential as spherical Harmonics. Thus,

$$\frac{1}{|\mathbf{r} - \mathbf{R}|} = \sum_{k=0}^{\infty} \frac{4\pi}{2k+1} \frac{r^k}{R^{k+1}} \sum_{q=-k}^k Y_k^q(\Theta, \Phi) Y_k^q(\theta, \phi) \quad (1.11)$$

where R, Θ and Φ are spherical coordinates that correspond to the ligated ions while r, θ and ϕ describe the 4f electrons. Thus, the ligand field operator can be written as:

$$\mathcal{H}_{LF} = \sum_{k=0}^{\infty} \sum_{q=-k}^k r^k \left(\frac{4\pi}{2k+1} \int \frac{\rho(\mathbf{R})}{4\pi\epsilon_0 R^{k+1}} Y_k^q(\Theta, \Phi) d\tau \right) Y_k^q(\theta, \phi) \quad (1.12)$$

We can separate the ligand degrees of freedom from the ones describing the 4f electrons with

$$A_k^q = \frac{4\pi}{2k+1} \int \frac{\rho(\mathbf{R})}{4\pi\epsilon_0 R^{k+1}} Y_k^q(\Theta, \Phi) d\tau \quad (1.13)$$

being the ligand field parameters.

Finally, by using the irreducible tensor formalism Y_k^q can be expressed as a function of equivalent spin operators [16, 14]:

$$\mathcal{H}_{\text{LF}} = \sum_k \sum_{q=-k}^k \alpha_k (1 - \sigma_k) A_k^q \langle r^k \rangle O_k^q = \sum_k \sum_{q=-k}^k B_k^q O_k^q \quad (1.14)$$

where O_k^q are equivalent Steven's operators, B_k^q are Steven's coefficients, α_k are the proportionality constants between Y_k^q and O_k^q , and σ_k is a screening constant.

The Steven's operators are functions of J_z, J_-, J_+ and are listed in [16, 14]. The index k represents the order of the operators. The sum includes only even terms as only even terms generate non-zero matrix elements. The subscript q denotes the operator's rotational symmetry.

The coupling between \mathbf{J} and the external magnetic field (\mathbf{H}) is modelled through the Zeeman term:

$$\mathcal{H}_Z = g_J \mu_B \mu_0 \mathbf{H} \cdot \mathbf{J} \quad (1.15)$$

where μ_B is the Bohr magneton and:

$$g_J = \frac{g_L [J(J+1) + L(L+1) - S(S+1)] + g_S [J(J+1) + S(S+1) - L(L+1)]}{2J(J+1)} \quad (1.16)$$

Hyperfine interaction

If the Ln ion has a non-zero nuclear spin, I , it couples to the surrounding electronic shell and further splits the electronic levels in a manifold of hyperfine levels. The interaction is modelled by adding a hyperfine and a nuclear quadrupolar contribution to the spin Hamiltonian:

$$\mathcal{H}_n = A_{\text{hyp}}(\mathbf{J} \cdot \mathbf{I}) + \mathbf{I} \hat{P}_{\text{quad}} \mathbf{I} \quad (1.17)$$

The isotropic hyperfine interaction, $A_{\text{hyp}}(\mathbf{J} \cdot \mathbf{I})$, has three components:

(1) the Fermi contact interaction

$$\mathcal{H}_n^F = \frac{2g_n g_J \mu_0 \mu_B^2}{3} (\mathbf{I} \cdot \mathbf{J}) \delta(\mathbf{r}) \quad (1.18)$$

(2) the paramagnetic spin-orbit contribution

$$\mathcal{H}_n^P = \frac{g_n \mu_0 \mu_B^2}{2\pi} \frac{\mathbf{L} \cdot \mathbf{I}}{r^3} \quad (1.19)$$

(3) and the dipole-dipole component

$$\mathcal{H}_n^D = \frac{g_n g_J \mu_0 \mu_B^2}{4\pi r^3} \left[\mathbf{I} \cdot \mathbf{J} - \frac{(\mathbf{I} \cdot \mathbf{r})(\mathbf{J} \cdot \mathbf{r})}{r^2} \right] \quad (1.20)$$

The quadrupolar term, $\mathbf{I} \hat{P}_{\text{quad}} \mathbf{I}$, results from the interaction between nucleus quadrupolar moment and the electrostatic ligand field gradient and thus is present only for ions with $I > 1/2$ that are placed in non-spheric environments:

$$P_{\alpha\beta} = \frac{Q}{2I(2I-1)} \langle V_{\alpha\beta} \rangle \quad (1.21)$$

where Q is the nuclear quadrupole moment and $V_{\alpha\beta}$ is the electrostatic tensor gradient.

TbPc₂ molecule

As a first example let's consider shortly the terbium(III) bis(phtalocyanine) (TbPc₂) complex. It will be discussed in greater detail in Chap. 3.

The Tb³⁺ ion, found at the core of the molecule, exhibits the [Xe]4f⁸ electronic structure which leads to a spin $S = 3$ and an orbital angular momentum $L = 3$. The ground state of the Tb³⁺ ion is thus $J = L + S = 6$. The strong spin orbit coupling leads to a separation of about 2900 K between the ground state and the excited state ($J = 5$) (see Fig. 1.3). Therefore, at low temperatures, the spin is confined to the ground state multiplet, $J = 6$, comprised of $2J + 1$ (degenerate) substates, $|J, m_J\rangle$.

The interaction with the phtalocyanine (Pc) planes further splits the energy levels in the ground multiplet. The crystal field interaction generates a quantization axis oriented perpendicular to the Pc planes and was modelled by the following Hamiltonian [17]:

$$\mathcal{H}_{\text{lf}} = B_2^0 O_2^0 + B_4^0 O_4^0 + B_4^4 O_4^4 + B_6^0 O_6^0 + B_6^4 O_6^4 \quad (1.22)$$

The ligand field parameters, A_q^k , were determined experimentally by the simultaneous fit of the NMR and magnetic susceptibility measurements performed on a LnPc₂ isostructural series[17]:

$$A_k^q \langle r^k \rangle = a_k^q + b_k^q (n - n_0) \quad (1.23)$$

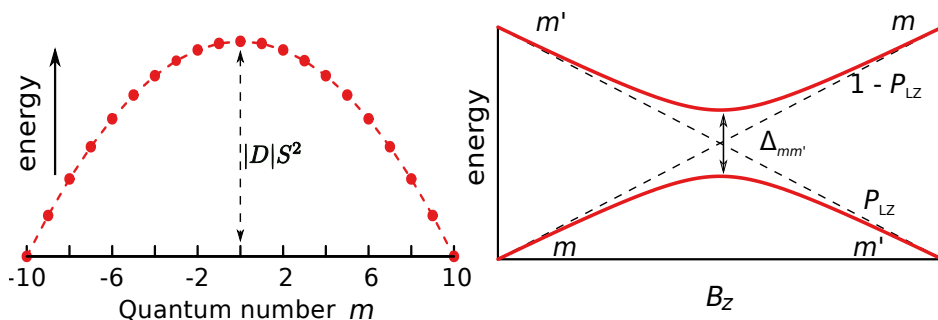


Figure 1.4: *Left:* Energy levels of a spin $S = 10$ subject to the ZFS term. *Right:* A zoom of the energy level diagram near an avoided level crossing where m and m' are the quantum numbers of the energy levels. P_{LZ} is the Landau-Zener tunnel probability when sweeping the applied field from the left to the right over the anticrossing. The greater the gap $\Delta_{m,m'}$ and the slower the sweeping rate, the higher is the tunnel probability P_{LZ} (Eq. 1.30).

when n is the order of the lanthanide in the series and a_k^q and b_k^q are the fit parameters.

The Tb^{3+} ion also has a nucleus with a non-zero spin, $I = 3/2$. The strong interaction between the electronic shell and ^{159}Tb nucleus is described by the hyperfine term, $(A_{\text{hyp}} I_z J_z)$, and the quadrupolar term, $(P_{\text{quad}} I_z^2)$, added to the total Hamiltonian. The resulting hyperfine structure is shown in Fig. 1.3.

Transition Metal Ion compounds

To illustrate the power of the ligand field formalism let's consider a transition metal ion compound that is characterized by a quenched orbital angular momentum. As a consequence, the Hamiltonian, in a first approximation, can be written using only spin degrees of freedom. The spin-orbit interaction, treated as a perturbation of second order, is nonetheless very important because it couples the magnetic ions to the surrounding organic ligands, leading to critical contributions to the anisotropy of the molecule. By considering only the quadratic terms from Eq. 1.14 in zero external magnetic field, the Hamiltonian of the system is given by:

$$\mathcal{H} = DS_z^2 + E(S_x^2 - S_y^2) \quad (1.24)$$

where D and E are commonly used notations that stand for the Steven's coefficients $3B_2^0$ and B_2^2 , respectively. D is negative when z-axis is chosen to coincide with the easy axis of the molecule, which will be assumed in the following, and $|E| \ll |D|$ in most cases.

Considering only the first term in the above Hamiltonian, we see that the states pertaining to the S multiplet and labeled by the quantum number $m = -S, \dots, S$, are only doubly degenerate: $E(\pm m) = -|D|m^2$. For this reason, the magnetic anisotropy constant D is often denoted as zero field splitting (ZFS).

The discrete energy levels follow a parabola, illustrated in the Fig. 1.4. $U = |D|S^2$ is called the anisotropy barrier. The two sides of the barrier correspond to opposite orientations of the magnetic moment, thus the ZFS term gives the approximate energy barrier the spin has to overcome to flip its orientation.

The height of the barrier and the characteristic time of the experiment lead to the definition of the blocking temperature (T_B), as the temperature under which the phonons do not have sufficient energy to promote reversal processes (e.g., for $\text{Mn}_{12}\text{-ac}$, $T_B \sim 4$ K for a characteristic time of the experiment of 1 s). Increasing the blocking temperature remains a central research goal in the field of SMMs [18, 19, 20] with the current record anisotropy barrier being 1,760 K and $T_B \sim 60$ K [11, 21]. The last term in (1.24) breaks the axial symmetry of the system and strongly affects the low temperature relaxation of the magnetization (Sect. 1.2).

Multi-spin Hamiltonian

Although, a number of molecules having a single magnetic ion have been synthesized [22], most SMMs contain multiple magnetic centers within their organic shell, and their description thus requires a multi-spin Hamiltonian.

For a pair of spins coupled through exchange interaction, the Hamiltonian can be written as [23]:

$$\mathcal{H}_{\text{exc}} = \mathbf{S}_1 \hat{J}_{12} \mathbf{S}_2 \quad (1.25)$$

In general, the interaction tensor \hat{J}_{12} is not symmetric, so it is customary to put the above equation in a form that highlights an isotropic term ($J_{12} \mathbf{S}_1 \cdot \mathbf{S}_2$) that favours a parallel alignment of the spins, an anisotropic, symmetric component ($\mathbf{S}_1 \hat{D}_{12} \mathbf{S}_2$) that tends to align the spins along a certain direction in space, and Dzyaloshinsky-Moriya term ($\mathbf{d}_{12} \cdot (\mathbf{S}_1 \times \mathbf{S}_2)$) that works toward orienting the spins perpendicular to each other. Usually, the isotropic term is significantly larger than the others and its sign will dictate the ferromagnetic or antiferromagnetic character of the ground state.

The generalization to a system containing an arbitrary number of spins is done by putting together the single ion anisotropies with the pairwise exchange interactions, leading to the following multi-spin Hamiltonian:

$$\mathcal{H} = \sum_i \mathbf{S}_i \hat{D}_i \mathbf{S}_i + \sum_{ij} \mathbf{S}_i \hat{J}_{i,j} \mathbf{S}_j \quad (1.26)$$

where we considered only the quadratic term in the ligand field Hamiltonian. Even with this simplification, the number of parameters involved can be quite large, especially for clusters with high nuclearity. This difficulty cannot be completely eliminated, even when one considers a very symmetric molecule. As an example let's consider the archetypal $\text{Mn}_{12}\text{-ac}$ molecule (Fig. 1.1). It contains an inner ring of four Mn(IV) ions ($S_4 = 3/2$) and an outer ring of eight Mn(III) ($S_3 = 2$) coupled together through superexchange interactions involving oxygen bridges. The number of states that characterizes the system is: $(2S_4 + 1)^4(2S_3 + 1)^8$, which yields an overwhelming 10^8 eigenstates. Because the $\text{Mn}_{12}\text{-ac}$ molecules crystallize in a body-centred tetragonal crystal, the unit cell contains two equivalent Mn ions so one independent zero-field splitting tensor is needed. When choosing a coupling scheme with only isotropic interactions[2], another four exchange parameters are required. Adjusting this model to experimental results, such as electron paramagnetic resonance (EPR) measurements, is far from trivial. Nevertheless, this model is valuable for low nuclearity systems[24]. A common way to shrink the dimension of the Hilbert space in which we have to study the system is done by replacing pairs of strongly interacting spins with a single equivalent spin.

Giant Spin Hamiltonian

Applying the above procedure recursively to all spin pairs leads to the giant spin approximation, which describes in an effective way the ground state multiplet. This simplification works especially well when the temperature is low enough so that the dominant energy in the system is the exchange interaction. In this case, the system is always found in its spin ground state (e.g., $S = 10$ for Fe_8 and $\text{Mn}_{12}\text{-ac}$), allowing the use of the single ion model presented at the beginning of this section. Therefore, we write the giant spin model:

$$\mathcal{H}_{GS} = DS_z^2 + g\mu_B\mu_0H_zS_z + \mathcal{H}_T \quad (1.27)$$

where D and g are now effective parameters, and \mathcal{H}_T describes non-axial interactions and can be written as a function of rising and lowering spin operators (S_+ , S_-). In order to relate the effective parameters of the giant spin model and the parameters characterizing each individual magnetic center one can use projection techniques[25], where single ion anisotropies are projected onto the vector space corresponding to the molecular ground state. This method is less accurate when the Hilbert space is very large, like in the case of $\text{Mn}_{12}\text{-ac}$, but the model retains its use because of its simplicity and intuitive form.

The energy range in which the giant spin model is valid can be found in the multi-spin Hamiltonian. Indeed, the weakest exchange link gives with a good approximation

the upper temperature limit to which the predictions are expected to be accurate. Experimentally one can observe the crossover to higher spin subspace by determining the magnetic moment associated with the molecular cluster[26, 27].

1.2 Quantum Tunneling of Magnetization

For a ligand field Hamiltonian described only by the ZFS term, the magnetic field lifts the two-fold degeneracy of the $\pm m$ energy levels. However, two different levels (denoted by m and m'), align for specific field values $H_r^{m,m'}$, applied along the magnetic principal axis:

$$H_r^{m,m'} = \frac{|D|(m + m')}{g\mu_B\mu_0} \quad (1.28)$$

Due to transverse terms of the spin Hamiltonian, the degeneracy can be transformed into an avoided level crossing, see Fig. 1.4. The energy separation is called the tunnel splitting, $\Delta_{m,m'}$, and is a central parameter that characterizes the quantum tunneling dynamics of spins.

There are several theoretical tools that can be used to determine the tunnel splitting, including path integral formalism[28, 29], perturbation theory[30, 31], and numerical methods. The latter allows the possibility to consider arbitrarily complex spin Hamiltonians but leaves little intuition on the system's behaviour. Thus, a combination of the above techniques is to be preferred when performing both a quantitative and qualitative analysis of the magnetic properties of SMMs.

At an avoided level crossing, the eigenvectors of the Hamiltonian are a linear combination of the base vectors that correspond to negative and positive spin projections. This means that in these states, the magnetization of the spin has a non-zero probability to be found on either side of the barrier. This behaviour is called spin tunneling, that is, the spin is in quantum resonance between the opposite orientation states.

At a constant field tuned at an avoided level crossing, a spin initially situated on one side of the well will oscillate coherently between the mixed states with a characteristic angular frequency, $\omega_T^{m,m'}$, related to the tunnel splitting through the relation: $\Delta_{m,m'} = 2\hbar\omega_T^{m,m'}$. The field interval where this behaviour is predicted to happen is given by[23]:

$$\delta H_0 = \frac{\Delta_{m,m'}}{g\mu_B\mu_0|m - m'|} \quad (1.29)$$

. This quantity is called the bare tunnel width and can be as small as 10^{-9} T. However, environmental interactions broaden the observed width of the resonance and hinder coherent oscillations[32, 33, 34, 35].

Landau-Zener-Stückelberg(LZS) Model

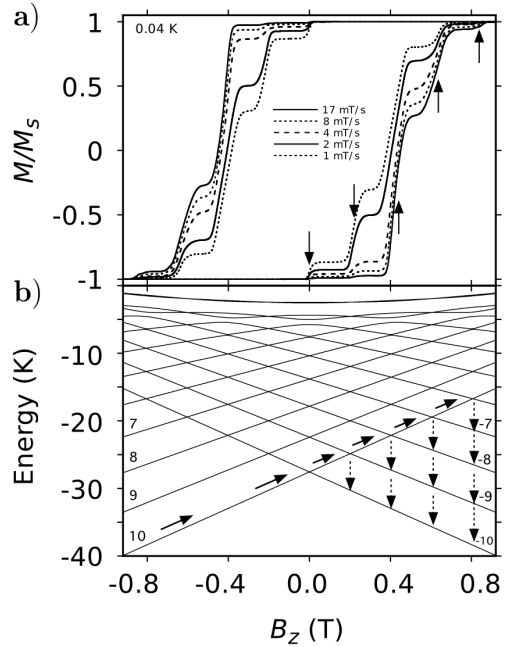
The nonadiabatic transition between the states of a two-level system was first discussed by Landau, Zener, and Stückelberg[36, 37, 38]. The original work by Zener concentrates on the electronic states of a bi-atomic molecule while Landau and Stückelberg considered two atoms that undergo a scattering process. Their solution to the time-dependent Schrödinger equation of a two-level system driven through resonance has been applied to many physical systems and it became an important tool for studying tunneling transitions. The LZS model was used to analyze spin tunneling in nanoparticles and clusters[39, 40, 41, 42]. The tunneling probability, P_{LZ} , between the states m and m' , after sweeping the applied field at a constant rate, α , through the resonance (Fig. 1.4), is given by:

$$P_{LZ} = 1 - \exp\left(-\pi\omega_T \frac{\delta H_0}{\alpha}\right) \quad (1.30)$$

With the LZS model in mind, we can now start to understand qualitatively the hysteresis loops of SMMs (Fig. 1.5), which exhibit steps of fast relaxation separated by regions where the magnetization is almost constant. The steps happen at specific fields where the levels from both sides of the well are mixed by transverse terms in the spin Hamiltonian, as discussed in the previous section.

Let us start at a large negative magnetic field H_z . At very low temperature, all molecules are in the $m = 10$ ground state (Fig. 1.5). As the applied field H_z is ramped down to zero, all molecules will stay in the $m = 10$ ground state. When ramping the field over the $\Delta_{10,-10}$ region, at $H_z \approx 0$, there is a Landau-Zener probability, $P_{10,-10}$, for the spins to tunnel from the $m = 10$ to the $m' = -10$ state. $P_{10,-10}$ depends on the sweeping rate (1.30), the slower the sweeping rate the larger is the tunneling probability. This is clearly demonstrated in the hysteresis loop measurements showing larger steps for slower sweeping rates [43, 6]. When the field H_z is now further increased, there is a remaining fraction of molecules in now metastable $m = 10$ state. The next chance to escape from this state is when the field reaches the $\Delta_{10,-9}$ region. There is a Landau-Zener tunnel probability $P_{10,-9}$ to tunnel from the $m = 10$ to the $m' = -9$ state. As $m' = -9$ is an excited state, the molecules in this state relax quickly to the $m' = -10$ state by emitting a phonon. An analogous procedure happens when the applied field reaches the $\Delta_{10,-10+n}$ regions ($n = 2, 3, \dots$) until all molecules are in the $m' = -10$ ground state, that is,

Figure 1.5: **a)** Hysteresis loops of a single crystal of Fe_8 molecular clusters at 0.04 K and different field sweep rates. The loops display a series of steps, separated by plateaus. The arrows indicate the resonance transitions highlighted in the figure below. **b)** Zeeman diagram of the $S = 10$ manifold of Fe_8 as a function of the field applied along the easy axis. From bottom to top, the levels are labeled with quantum numbers $m = \pm 10, \pm 9, \dots$. The levels cross at equidistant field values given by $\mu_0 H_z \approx n \times 0.22$ T with $n = 1, 2, 3, \dots$

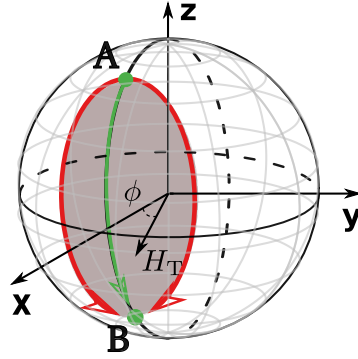


the magnetic moment of all molecules is reversed. As phonon emission can only change the molecule state by $\Delta m = \pm 1$ or ± 2 , there is a phonon cascade for higher applied fields.

When using the above formalism for a quantitative analysis, one should keep in mind that the LZS model is exact only for an isolated spin. Deviations from the ideal coherent dynamics are due to environmental interactions of both elastic (dephasing) and inelastic (relaxation and excitation) nature [5]. Thus, in order to try to search an agreement with LZS theory one should use large sweeping rates, so that in the time the resonance is swept, the local environmental field does not change significantly. The model also doesn't include relaxation through phonons so one should work at very low temperatures and focus on ground state tunneling.

LZS theory was successfully used to determine the tunnel splitting in molecular systems such as Fe_8 [6] and Mn_4 [43]. As mentioned, the agreement with the experiment must be searched in the fast sweeping rate regime, which has the drawback of a small sensitivity. To overcome this difficulty, the resonance can be swept repeatedly. This way, the probability for the spin to remain in the original state, for small variations of the magnetization, after n back and forth sweeps, is proportional to $(1 - 2nP_{LZ})$, with P_{LZ} given by (1.30).

Figure 1.6: The unit sphere that shows the degenerate minima **A** and **B** joined by two tunnel paths (red lines). The easy, medium and hard anisotropy axes are taken along the z -, y -, and x -direction, respectively. The constant transverse magnetic field H_T , used to tune the tunnel splitting, is applied in the xy -plane at an angle, ϕ . A quench of the tunnel splitting occurs when the area enclosed by the two paths is an odd integer of π/S .



1.3 Spin Parity and Quantum Phase Interference

When discussing quantum tunneling of magnetization it was emphasized that transverse terms remove the degeneracy of the eigenstates at a level crossing ($H_z = H_r$) and thus promote relaxation. Actually, the general problem of eigenvalue degeneracy is discussed by the von Neumann-Wigner theorem [45, 46] which states the need of at least two parameters (e.g., the components of the magnetic field), to control the degeneracy property of a Hermitian matrix. In this section we discuss the cases when the degeneracy is predicted theoretically and in some cases observed experimentally through the absence of tunneling at level intersections.

Spin Parity

The general form of a transverse term of order n is $B_n S_{\pm}^n$, thus a transition between the levels m and m' is made possible by applying S_{\pm}^n operator an integer number of times. Consequently, the degeneracy is removed only when the change in the spin projection is a multiple of the perturbation's order: $n | (m - m')$.

The above quantum tunneling selection rule is called spin parity effect and has its origin in the symmetry of the non-axial Hamiltonian term. For example, in the case of the Mn_3 cluster[47], with a C_3 rotational symmetry, level splitting should occur only if the selection rule: $m - m' = 3k$ is satisfied.

Another interesting example is the observation of Kramer's degeneracy in half-integer spin molecular clusters[48], which tells us that in zero transverse field, the ground state is at least doubly degenerate. This degeneracy can be lifted by a transverse field (a first order perturbation) of external or internal origin (e.g., dipolar and hyperfine field).

In general, the selection rules are rarely observed. Possible explanations involve asymmetries introduced by crystal defects, solvent disorder[49], above mentioned dipolar and hyperfine interactions, or Dzyaloshinsky-Moriya interaction[50] fuelled by low molecular symmetry and strong exchange coupling. In the case when one gets to control the above factors the spin parity effect can be clearly evidenced, as seen for Mn_3 [47].

Quantum Phase Interference

Suppression of tunneling can also occur for certain values of the transverse field, without involving the above presented selection rule.

The interference effect in spin systems was predicted theoretically[28] and then observed experimentally[6] using LZS approach and is generally called *Berry phase interference*. The mechanics behind the explanation of this phenomena makes it similar to the observation of critical current oscillations in Josephson junctions[51, 52] and Bohm-Aharonov oscillations[53].

A semi-classical description, which has a rather intuitive picture associated with it, describes the tunneling motion of the spin with the help of the path integral formalism [28]. The initial and final states are represented by two points on the Bloch sphere (Fig. 1.6). The interference is due to a non-zero phase difference acquired by moving in the parametric space along a closed path containing these two points.

The magnetic field has the ability to modulate the phase by modifying the paths, so an interference pattern is observed as the transverse field is increased.

Figure 1.7 shows the tunnel splitting as a function of the applied transverse field for several azimuth angles and for different level anticrossings computed by numerical diagonalization of the Fe_8 spin Hamiltonian . The anisotropy of the Fe_8 molecule, similar to many low symmetry molecules, is modelled by adding a biaxial crystal field ($\mathcal{H}_T^{LF} = E(S_x^2 - S_y^2)$) to the uniaxial term (Eq. 1.27). When the tunnel splitting between the levels S and $S - n$ is determined, the spin parity effect is observed (the second order transverse anisotropy term forbids odd resonances at zero field). Also, a monotonic increase of Δ with n is observed: the lower is the energy barrier the higher are the tunneling rates. The field separation between two consecutive minima of the tunnel splitting when we consider only the biaxial term is given by:

$$\Delta H = \frac{2}{g\mu_B} \sqrt{2E(E + D)} \quad (1.31)$$

Other systems in which it was possible to observe Berry phase interference include Mn_{12} complexes[54, 55, 56], Mn_4 [57], and dimer molecular magnets[58].

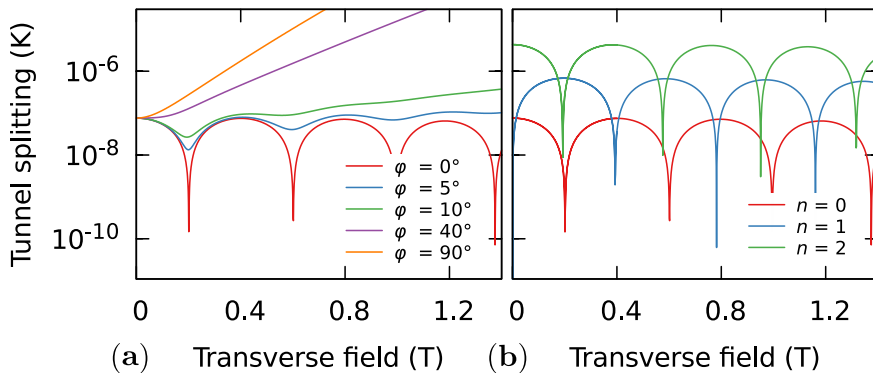


Figure 1.7: The tunnel splitting, Δ , as a function of a transverse field applied at **a)** several azimuth angles, φ , at $m = \pm 10$ anticrossing and **b)** quantum transition between $m = -10$ and $(10 - n)$ for $\varphi = 0^\circ$ computed by numerical diagonalization of the Fe_8 spin Hamiltonian (Eq. 1.27) with $\mathcal{H}_T = E(S_x^2 - S_y^2) + g\mu_B(S_x B_x + S_y B_y)$. The spin parity effect for $n = 1$ is analogous to the suppression of tunneling dynamics predicted for Kramer's ions.

1.4 Quantum Coherence in Molecular Magnets

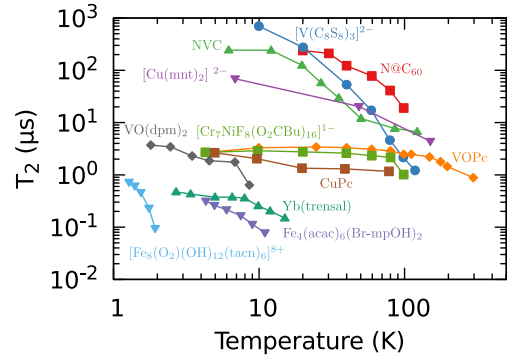
The study of coherence in molecular magnets is very important for the potential applications in the field of quantum information processing. Here we briefly account on the quest for the observation of coherent time evolution of molecular spins under electromagnetic (EM) radiation.

Resonant Photon Absorption

In EPR experiments involving molecular magnets[59, 60, 61], transitions between the m and m' states of the S multiplet happen when the energy of the incoming photons is equal to the energy difference between the states: $h\nu = |E(m) - E(m')|$, obeying the selection rule $\Delta m = \pm 1$. An important question that had to be answered concerns the effect of the photon-induced excitations on tunneling.

The first important results[62] were obtained when a Fe_8 complex was investigated using micro-Hall bars in a dilution refrigerator. The study proved that the lifetime of the excited states is large enough (relative to the tunneling time) for an enhanced relaxation to be observed. In order to clearly show the photon assisted quantum tunneling regime, circular polarized microwave radiation was used because it allows to select the $\Delta m = +1$ or $\Delta m = -1$ transitions. Thus, an asymmetric hysteresis loop is observed. From the dependence of the transition rates on the power of the microwave

Figure 1.8: Comparison of state-of-the-art T_2 values of notable molecular and solid state electronic spin qubits.



source used, it was shown that the effective spin temperature (the parameter that describes the occupation number of the excited states) depends linearly on the power of the EM field. Subsequent experimental work further proved the photon assisted tunneling regime[63, 64, 65] leading towards eventual observation of Rabi oscillations[61].

Rabi Oscillations

The coherent evolution of the system between two eigenstates coupled by the EM field is described by the Rabi model[66, 67]. If the system's initial state is $|m\rangle$, then the probability to find it in the state $|m'\rangle$, at time t , is proportional to $\sin^2(\Omega_R t)$. The Rabi frequency, Ω_R , is proportional to the amplitude of the perturbative field. This property is used in the spin-echo measurements protocols[68] to determine the characteristic relaxation times of the system.

The longitudinal relaxation time (T_1) is obtained from the recovery of the equilibrium magnetization after an inversion pulse, $\pi - T - \frac{\pi}{2} - \tau - \pi - \tau - \text{echo}$, is applied, where the variable is T and τ is being kept constant. T_1 is directly connected to the coupling of the spins to the phonon bath and thus can be significantly long at mK temperatures.

The second important characteristic time is the phase coherence time (T_2) and is determined by spin-spin interactions. As the name suggests, it tell us the time over which the memory of the quantum phase is preserved, so the quantum properties of the spin can be exploited. Employing a similar Hahn-echo sequence, $\frac{\pi}{2} - \tau - \pi - \tau - \text{echo}$, with τ variable, T_2 is obtained from the echo signals that are fitted to a stretched exponential,

$$I(\tau) = I(0) \exp(-(2\tau/T_2)^x) \quad (1.32)$$

The interaction with environmental spins of nuclear and electronic origin, phonons, and photons, represents the main sources of decoherence[69] in SMMs[70, 71], and thus limit T_2 . In order to reduce the dipolar interactions, one usually chooses a system with a small collective spin[64, 72, 61] because the magnitude of the interactions scales as the square of the spin magnitude. Then, SMMs can be diluted without greatly effecting their individual properties[72, 61, 73]. Also, the initial choice of a molecular complex with $S = 1/2$ [72], avoided the problems associated with the distribution of the anisotropy axis.

The above measurements led to the first observations of a long phase coherence time in Cr_7Ni ($S = 1/2$) and Cr_7Mn ($S = 1$) clusters[72]. Afterwards, Rabi oscillations were observed in V_{15} [61, 74] and T_2 on μs scale was measured in Fe_8 [75] through the application of a high transverse magnetic field.

Recent developments showed that a strict control over lattice rigidity and hyperfine interactions can lead to significantly large phase coherence times, even when compared to other qubit candidates ([73] and Fig. 1.8). The coherence also has been shown to be preserved at room temperature[76, 77]. These are valuable observations that encourage possible spintronics applications.

1.5 Molecular Quantum Spintronics

Molecular quantum spintronics is a relatively new research field that combines spintronics, molecular electronics and quantum computing with the aim of creating new spintronics molecular devices that exploit the quantum properties seen at the microscopic level[78, 79, 80]. These devices facilitate the read-out and manipulation of the spin states pertaining to a molecular magnet, leading to structures that can perform basic quantum operations.

The idea of using SMMs as magnetic centers in spintronics devices is supported by their unique characteristics, namely, weak spin-orbit coupling in transition metal ion compounds, tunable environmental interactions that can lead to a long coherence time (Sect. 1.4), chemically controlled functionalities like switchability with light or electric field[81]. The coupling to external structures can be facilitated by choosing an appropriate ligand. Delocalized bonds, that mediate the interaction between the magnetic ions, often imply great conduction properties.

The above outlined properties allowed the realization of some essential circuit elements, like[79]: molecular spin transistors[82, 83], molecular spin valves[84] and spin filters, and molecular double dot devices.

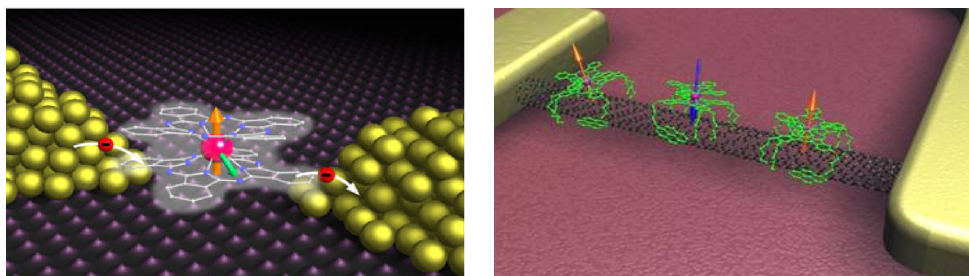


Figure 1.9: Artist view of (*left*) a nuclear spin qubit transistor based on a single TbPc_2 molecular magnet, coupled to source, drain, and gate (not shown) electrodes, and (*right*) a three spin-dot device (reprinted from[83]).

Quantum Algorithms

The research aimed at using molecular magnets for qubit encoding started mainly after the theoretical proposal of Leuenberger & Loss[85, 86] followed by others[87, 88, 89, 90, 91, 92]. We shall follow DiVincenzo[93] to summarize the steps taken towards successful implementation of a quantum computer using molecular magnets.

To use molecular magnets as qubits, external constraints (e.g., temperature, electric or magnetic field) should be applied in order to confine the system to a subset of two levels ($|0\rangle$ and $|1\rangle$). The scalability of the system is facilitated by the synthetic bottom-up fabrication process that guarantees cheap production of identical molecular units.

The implementation of proposed quantum algorithms[94, 95, 96, 97] involves the use of one-qubit and two-qubit gates. The former represents a rotation on the Bloch sphere. The output of the gate, after realizing an electric or magnetic coupling to the spin and applying an EM pulse sequence (Sec. 1.4), is the state: $\alpha|0\rangle + \beta|1\rangle$. A strong-coupling regime, at high temperatures, between a molecular spin ensemble and microwave resonators, has been achieved. The possibility of coupling strongly with single molecules has been put forward and experiments are in progress. This opens a way to develop scalable architectures using molecular spins coupled to quantum circuits[98, 99, 100, 101, 102]. Moreover, by molecular engineering of the crystal field, molecular spins can also be manipulated by electric fields[103, 104, 105, 82, 106].

A two-qubit gate can be implemented by controlling the exchange interaction between the spins. Schemes and compounds for switchable effective qubit-qubit interactions in the presence of permanent exchange couplings are now available[107, 108]. Spin entanglement between and within molecules was shown by different techniques.

Molecular spin clusters/arrays offer an incredible variety of spin topologies to test entanglement at the molecular scale[104].

It is necessary that the system remains in a coherent state (preserve α and β), for a time considerably larger than the computational *clock* time. This is an important requirement for the system to be amenable to quantum error corrections. As noted in Sect. 1.4, long coherence time (T_2) at low temperature have been reported for many ensembles of molecular spin systems with T_2 approaching 1 ms in nuclear spin-free environments[72, 109, 70]. Recent reports have shown microsecond coherence times and Rabi oscillations at room temperature[76, 110, 73, 111, 112, 77]. Strategies to protect spin states from decoherence (e.g., via atomic clock transitions) have been experimentally tested by fine engineering of molecular states and levels[113]. The development of theoretical schemes to implement quantum error correction codes in molecules with multiple spin degrees of freedom has also been started[114, 115, 116, 117, 118].

Another important requirement is the possibility to initialize and read-out the qubit state. As seen in previous sections, the read-out of a single molecular spin located at a tunnel junction or on a CNT/graphene quantum dot has been demonstrated[119, 84, 120].

All this achievements are important milestones in molecular magnetism. They bring this research field closer to being able to provide the future basic components of quantum devices[121].

2 Experimental Details

During my PhD I worked on the automation of the μ SQUID technique. I've built on the work of Raoul Piquerel, a former PhD student [122], who together with Edgar Bonet and Christophe Thirion developed the general software framework.

Overview setup

Figure 2.1 shows the main components of the experimental setup used to perform sub-kelvin magnetometry on crystals of single molecule magnets. At the heart of the technique is a superconducting quantum interference device (SQUID) that is used to detect the variation of the magnetic field generated by the sample. A number of factors determine the coupling between the sample and the μ SQUID (e.g. the size of the crystal, the dilution state, position of the crystal with respect to the μ SQUIDs, etc.), thus, to optimize the magnetic signal and reduce the number of bad samples, the crystals are placed on an array of μ SQUIDs. The μ SQUIDs and the sample are mounted on the epoxy sample holder, thermalized at the coldest stage of the cryostat in a magnetically shielded environment.

The control over the SMM's magnetic moment is achieved through a DC magnetic field created by a 3d axis coil system and/or a RF field applied to the sample through a wire antenna. The 3d axis coil system gives us the ability to access all three field dimensions, especially important when aligning the external field in the plane of the μ SQUIDs and in finding the easy axis of the molecules. The small size of the coils (i.e., small inductance) allows for fast field sweeping rates. We generally go up to 1 T/s but dB_z/dt up to 10 T/s are accessible. The coils are thermalized to the 4 K stage of the dilution fridge.

The drive of the current through the μ SQUID and the detection of the superconductive-resistive transition is done by specialized low noise electronics, called " μ SQUID electronics". The automation of the measurement process is done with the use of Adwin - a real-time data acquisition device. It is responsible for both the fast, time critical processes like keeping time in the measurement of the switching current, triggering of the RF source but also for some slower processes like the control over the current sources that drive the superconducting coils.

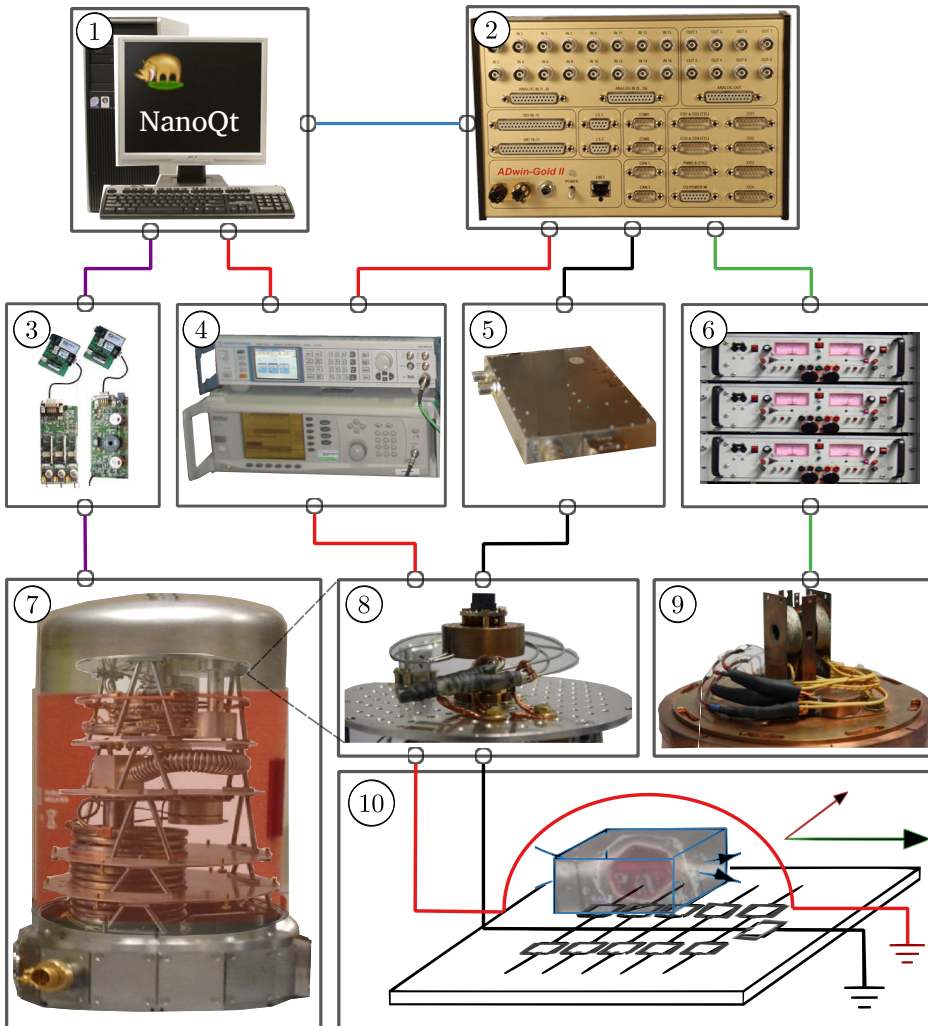


Figure 2.1: Overview of the μ SQUID setup: (1) NanoQt – asynchronous acquisition program running on a Linux machine, (2) Adwin automat, (3) PID temperature controller, (4) RF generators, (5) μ SQUID electronics, (6) the current sources that drive the 3d coil system, (7) He^3/He^4 dilution refrigerator, (8) 25 mK cold stage of the cryostat with the sample holder, (9) 3d-axis coil system mounted on top of the 4 K stage, and (10) schematic representation of a SMM crystal on top of an array of μ SQUIDS. The line connectors show the communication between different modules: (*blue*) the communication between the PC user (Nanoqt client) and the Adwin automat. (*purple*) temperature control, (*red*) RF module that terminates with a grounded wire antenna, (*black*) critical current measurement and (*green*) applied DC magnetic field.

The high level control over the experimental protocol is provided by NanoQt – an asynchronous acquisition program that was developed inside our group. It interfaces with the Adwin automaton, RF generator, temperature controller, etc., through TCP/IP connections.

Most of the experiments are performed at subkelvin temperatures that are reached through the use of a home built He³/He⁴ dilution refrigerator. The μ SQUID technique is enhanced by adding a microwave module. With the microwave radiation generated by the AnritsuMG369x frequency synthesizer transported to the sample through a coaxial cable thermalized from room temperature to 25 mK and then applied to the sample through a golden wire antenna.

μ SQUID

The μ SQUID is designed as a flat loop made of a superconducting Nb-AlO_x-Nb trilayer with two constrictions (micro bridges) and connected to superconducting DC lines that are used to polarize the device. Besides geometrical parameters, the properties of the μ SQUID depend on the external conditions like temperature, magnetic field and current density. Below, we denote by (T_c, I_c, B_c) the set of parameters below which the μ SQUID is found in a superconducting state. The parameters are not independent, in fact, the relation between the critical current and the magnetic flux passing through the SQUIDs loop is used in the μ SQUID detection scheme:

$$I_c = I_0 \left| \sin \left(\frac{\Phi}{\Phi_0} \right) \right| \quad (2.1)$$

where $\Phi_0 = h/2e$ is the flux quanta and $\Phi = \mathbf{B} \cdot \mathbf{S}$ is the magnetic flux passing through the SQUID loop.

Figure 2.2 shows the experimental measurement of the critical current as a function of a magnetic field perpendicular to the μ SQUID loop. Significant deviations from the theoretical prediction (black line) are observed: both branches display a significant more linear dependence than the predicted sinusoidal one, also the branches cross at the inflection points. This does not mean that, two values of the critical current are observed during a single I_c measurement but rather the low or the high value is determined in subsequent measurements. The differences between the theoretical model and the measured characteristics are most likely the result of the asymmetry of the μ SQUIDs. The bistability region will be avoided when choosing the working point in the feedback mode.

The $I_c(B)$ characteristic shows that a small variation of the magnetic field leads to a large change in the critical current. This observation explains the high sensitivity

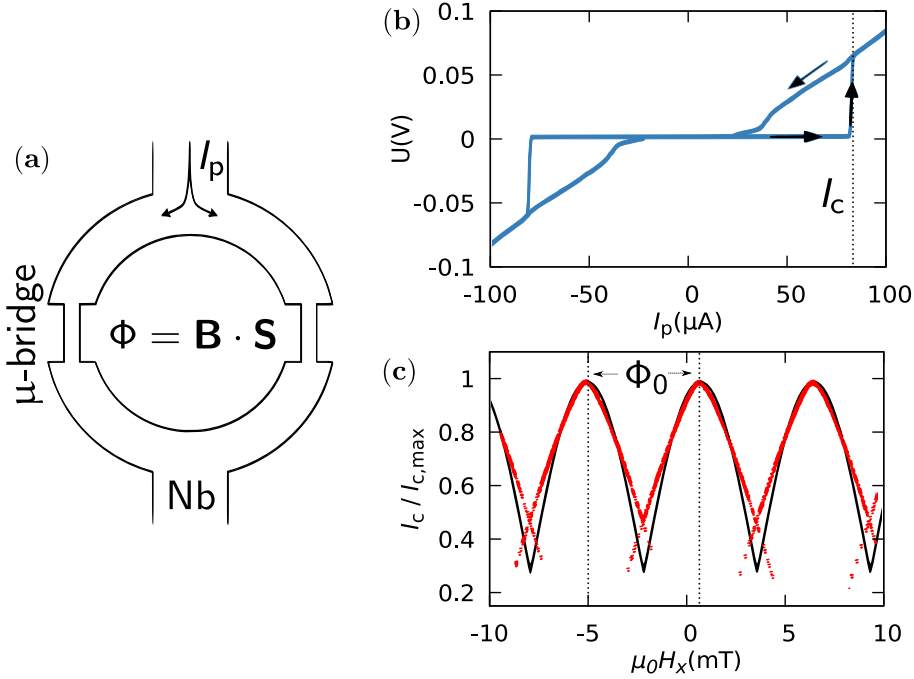


Figure 2.2: a) Schematic representation of the Nb μ SQUID. I_p is the polarization current and Φ is the magnetic flux passing through the SQUID's loop. b) $I(V)$ characteristic of the μ SQUID. The broken line indicates the current value at which the superconducting-resistive transition occurs. c) Critical current as a function of a magnetic field perpendicular to the μ SQUID loop. Significant deviations from the theoretical prediction Eq. 2.1 (black line) are observed: positive and negative branches display a significant more linear dependence than the predicted sinusoidal dependence and a crossing of the critical current branches is observed. The differences between the theoretical model and the measured characteristics are most likely the result of the asymmetry of the μ SQUIDs. The period of the $I_c(H_x)$ characteristic gives the flux quanta, $\Phi_0 = h/2e$.

of the μ SQUID technique. The limit of detection can be estimated by using the uncertainty principle, $\Delta E \Delta t \approx \hbar$, with $\Delta E = \Phi^2/2L$, and thus $\Delta\Phi_Q = \sqrt{2L\hbar}/\sqrt{\Delta t}$.

Measurement protocol

The measurement protocol is based on the periodic determination of the critical current. Figure 2.3 shows the current polarization of the μ SQUID with three distinct stages. First, the current is increased rapidly to a value close to the critical current (plateau). The time reserved for this stage (10 μs) is chosen to assure the stability of the polarization current. Then, the current is ramped linearly towards the critical value. The transition of the μ SQUID from superconducting to resistive regime leads

to a voltage drop across it. When the voltage is detected the polarization current is set to zero to avoid the overheating of the sample through the Joule effect. Before starting a new measurement cycle, sufficient time must be reserved for the SQUID to cool down and become again superconducting. If no detection is observed in the measurement period the current is set to zero and a new cycle is started. In the current measurement scheme the period is limited to around 100 μs .

The plateau and the slope is adjusted so that the critical current is reached during the linear increase of the polarization current. The duration of the ramp measures the critical current and thus the objective is to determine it as precisely as possible. Note that, we are interested in the variation of the critical current and not in its absolute value.

Most of the measurements of the hysteresis loop of crystals of SMMs are done using the so called "feedback mode" [123]. The μSQUID s are sensible to the transverse dipolar field generated by the SMMs. In the feedback mode we keep the flux constant, independent of the magnetization of the sample (see Fig. 2.3). Thus, the variation in the dipolar field (which is proportional to the variation in the magnetization) is compensated by an opposite applied field, the stability of the working point is achieved through the implementation of a feedback loop:

$$\delta B_x^{\text{feed}} = \alpha \delta I_c \quad (2.2)$$

where α is the feedback constant.

If the external magnetic field is not applied exactly in the plane of the μSQUID (due to misalignment issues) then the μSQUID also measures the transverse component of the applied field. This is accounted for by adding a correction to the feedback field:

$$\delta B_x^{\text{plan}} = a_y B_y + a_z B_z \quad (2.3)$$

where $a_{y,z}$ are the misalignment slopes.

Low Noise Electronics

The μSQUID electronics is responsible for driving the current through the SQUIDs and for detecting the superconducting-resistive transition. It contains three distinct stages. The digital part is responsible for the interface with the device that keeps the time (the Adwin in our case). An analog circuit responsible for generating low noise current necessary to polarize the μSQUID s. And a circuit to detect the voltage drop across the μSQUID and thus register the transition.

The analog circuit is a modular voltage generator in series with an externally adjustable resistor that gives access to polarization currents in the $20\ \mu\text{A} - 4\ \text{mA}$ range. The slope can be adjusted in the range $\pm 800\ \text{mV/s}$ with a resolution of $\pm 0.2\ \text{mV/s}$ while the plateau can be increased up to $4\ \text{V}$ in steps of $0.6\ \mu\text{V}$.

The μSQUID is part of an electric circuit of several hundreds ohms while the change in the resistance, due to SQUID's transition from superconducting to resistive state, is very small. Thus, the transition is detected by monitoring the voltage across the μSQUID and applying a high pass filter that allows to determine sudden variations that occurs due to SQUID transitions. If the detected voltage drop exceeds the threshold value the polarization current is set to zero.

The digital part is responsible for the communication with the Adwin automaton. It uses two distinct serial communication protocols. A three wire protocol for setting the values for the plateau, slope and detection threshold. And a two wire protocol for timing the critical current through the μSQUID s. The communication was optimized to use the smallest number of channels.

The two wire protocol (Fig. 2.3) is composed of a "rearme" and a "stop" line. The "rearme" command line is used to start the μSQUID measurement. The first rising edge instructs the electronics to increase the current to the plateau value. This level is maintained as long as the "rearme" signal is high. The falling edge begins the current ramp. When the transition is detected the signal is transmitted to Adwin through the "stop" channel. The time difference between the falling edge of the "rearme" command and the rising edge of the "stop" command is proportional to the critical current with the proportionality constant being the slope.

Adwin

The Adwin automaton is a "real-time" data acquisition device that is used to exert time critical control over different modules of μSQUID setup. Adwin's main component is the processor T11 which is the master on the main bus and thus responsible to coordinate and synchronize all the other modules. It has a clock cycle of $3.3\ \text{ns}$ and is not optimized for speed but for reproducibility of the execution time. The main process running on T11 is responsible for reading the inputs, evaluating the response and setting the outputs. The period of this process is set to $10\ \mu\text{s}$ chosen so that the workload never exceeds 90%.

The Adwin comes with a number of developed libraries that facilitates the interface between the automaton and high level technologies like C++, Python, etc. The connection to the computer client is done through an Ethernet cable with the support

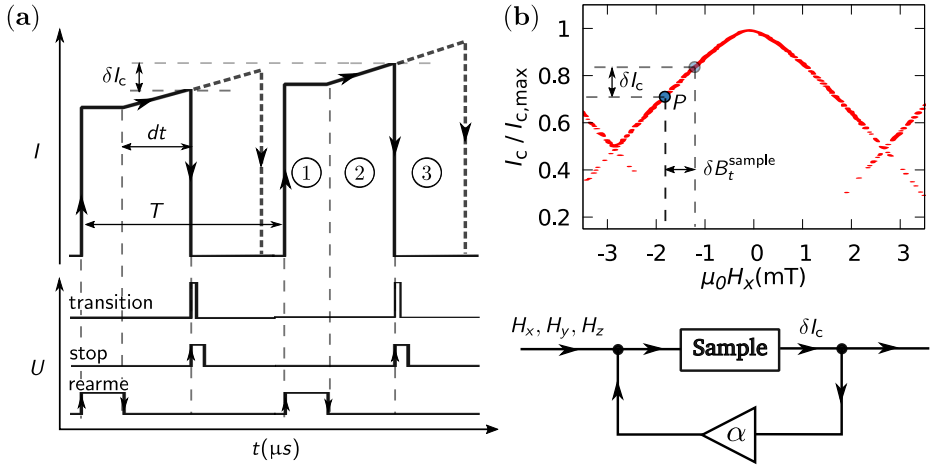


Figure 2.3: **a)** The measurement protocol used to determine the critical current. The current polarization of the μ SQUID is done in three distinct stages. (1) The current is increased rapidly to a value close to the critical current (plateau). The time reserved for this stage ($10 \mu\text{s}$) is chosen to assure the stability of the polarization current. (2) The current is ramped linearly towards the critical value. The transition of the μ SQUID from superconducting to resistive regime leads to a voltage drop across it. When the voltage is detected the polarization current is set to zero (3) to avoid the overheating of the sample through the Joule effect. In the current measurement scheme the period (T) is limited to around $100 \mu\text{s}$. The plateau and the slope is adjusted so that the critical current is reached during the linear increase of the polarization current. The duration of the ramp (dt) measures the critical current. On the bottom panel is shown the two wire communication protocol between the Adwin and μ SQUID electronics. The protocol is composed of a "rearme" and a "stop" line. The "rearme" channel is used to start the μ SQUID measurement. The first rising edge instructs the electronics to increase the current to the plateau value. This level is maintained as long as the "rearme" signal is high. The falling edge begins the current ramp. When the transition is detected the signal is transmitted to Adwin through the "stop" channel. The time difference (dt) between the falling edge of the "rearme" command and the rising edge of the top command is proportional to the critical current with the proportionality constant being the slope. **b)** The feedback mode used in the μ SQUID magnetometry in which the flux passing through the μ SQUID loop is kept constant, independent of the magnetization of the sample. The variation in the dipolar field ($\delta B_t^{\text{sample}}$), which is proportional to the variation of the magnetization, is compensated by an opposite applied field through a feedback loop **c)** and thus ensuring the stability of the working point (P).

for the TCP protocol. It is also equipped with input/output modules as 14 bits AD/DA converters with a sampling frequency of 100 MHz.

Important for μ SQUID measurements, the Adwin automaton can be equipped with a subordinate processor with a clock cycle of 50 MHz and with access to digital I/O ports, called TiCo. The main processor is used for computational heavy tasks like the calculation of the feedback field and communication with the computer client while the TiCo processor is reserved mainly for the purpose of interfacing with the μ SQUID electronics. It is used to set the value of the plateau, slope and detection threshold and also to keep time in the μ SQUID protocol, and to trigger the RF generator. One can program the TiCo processor in a similar way to the T11 processor but the communication with the process running on TiCo, for 'run-time' control and data exchange can be done only indirectly through the main Adwin processor.

NanoQt

The high level control over the experimental setup is done with the help of an asynchronous acquisition program, called NanoQt. NanoQt was developed in the C++ framework inside our group to take advantage of the Adwin automaton and centralize the control over different experimental devices. The user interface is built with the use of the QT library with a JavaScript wrapper for scripting support. The communication with the Adwin is done through the use of a specialized library provided by the development team of the automaton. NanoQt is also used to communicate with peripherals (e.g., RF source, PID temperature controller) through Ethernet connections and to design the protocols for the experiments. The central concept behind the design of a measurement protocol is the definition of a path in the field parametric space. The user has to define the nodes on the path and the duration (or the sweeping rate) it takes to go from one step to another. NanoQt also allows to view the collected data in real time and save it for later analysis.

Microwave device

During my PhD I also worked on developing an extra module for the μ SQUID setup that allows us to excite the sample with electromagnetic radiation and use the μ SQUID as a magnetic probe. To generate electromagnetic radiation, the commercial AnritsuMG369x arbitrary wave function generator was used. It provides pulses with frequency in [0.1:40] GHz range, power up to 20 dBm and with a width as small as 1 ns. The RF source is controlled through NanoQt using an Ethernet connection. This allows to set the parameters of the RF pulses (frequency, power, width, etc.,) that are

applied in between μ SQUID measurements. We operate the source in a triggered mode, that is, the pulse is generated as a response to an input trigger emitted by the Adwin automat. For the initial development of the technique, we pursued only the resonant excitation of the system and thus the amplitude of the RF field and frequency together with the width of the pulse are the only parameters that we controlled with no particular interest in the phase of the RF pulses. The EM radiation is then guided to the sample through a coaxial waveguide with the core made of stainless steel and the dielectric made of teflon which is thermalized between room temperature and 40 mK through the thermal contact established at different stages of the fridge. The microwave coaxial guide is connected to ground through a gold wire suspended on top of the sample. The wire serves as an antenna that generates electromagnetic field to excite the sample. The coupling between the sample and the EM radiation is weak and occurs mainly through the magnetic field component.

3 Tb³⁺ molecular magnets

3.1 The role of quadrupolar interaction in tunneling dynamics of TbPc₂ SIMM

Single ion molecular magnets (SIMMs) are the first members in the ever growing family of magnets that employ molecules as their basic unit [22]. Their simple magnetic core motivated a considerable scientific effort to correlate different chemical designs to exhibited magnetic properties [124, 125], and to induce and control coherent quantum dynamics on a large timescale [72, 73, 77]. The objective is to reach a level of understanding that will allow to synthesize molecular units suited to be incorporated in functional devices [126]. In the search for the optimal molecular design (to enhance bistability and dynamical properties of SIMMs) the chemical control over the symmetry of the complex and the nature of the ligand substituents proved to be essential [127, 128]. The progress made in the last decades being relevant both to the fundamental research in the field of mesoscopic quantum physics [27], and to the trend and outlook of the current technology [129, 90, 130].

A central property of molecular magnets is their magnetic bistability, that is, the existence of an energy barrier that separates states of different spin orientation. Thus, they are envisioned as memory units in high density storage devices [131]. The obvious strategy to reach this highly sought goal is to enhance the uniaxial anisotropy to obtain molecular complexes that exhibit hysteresis at high enough temperatures. Advancement in this direction has been recently reported as a mononuclear Dy compound was shown to exhibit magnetic hysteresis at temperatures up to 60 K [132, 11]. However many challenges still need to be surmounted, one of which lies in the intrinsic quantum nature of molecular magnets itself. Notably, underbarrier relaxation pathways (*e.g.* pure and phonon assisted quantum tunneling), opened by transverse interactions that break the axial symmetry of the molecule, results in a much lower effective energy barrier.

Quantum tunneling of magnetization was also instrumental in reading out and manipulating both the electronic and the nuclear spin of a mononuclear molecular

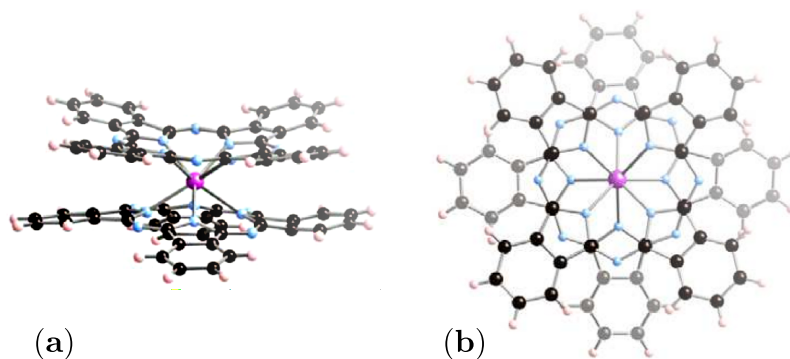


Figure 3.1: **a)** Side view and **b)** top view of the $TbPc_2$ molecule which features a Tb^{3+} ion sandwiched between two phthalocyanine planes in a square antiprismatic symmetry (D_{4d}) – the Tb^{3+} ion is coordinated by 4 nitrogen atoms from each ligand plane and the upper Pc ligand is a mirror reflection of the lower one (with respect to the x - y plane) rotated by 45° around the z -axis. (Colour code: Tb, pink; N, cyan; C, black; O, red; H atoms have been removed for clarity).

complex [133], to the point of the successful implementation of quantum algorithms [12]. Thus, understanding the mechanisms that operate behind the observed tunneling dynamics is an important prerequisite to design application oriented molecular magnets.

Amongst already numerous example of SIMMs, the $TbPc_2$ molecule can be linked to breakthrough discoveries that greatly helped to advance the agenda of this research field. First, through ac-measurements it was noticed that a molecule with a single magnetic center can exhibit a large energy barrier [134]. Then, micro-SQUID measurements on a diluted $TbPc_2$ molecular crystal experimentally showed resonant relaxation through quantum tunneling between mixed states of both electronic and nuclear origin [135]. Thus, it became the system of choice for the first molecular spintronics devices [136, 84, 137] and it helped to construct the case for using molecules as potential qubits.

In this section we revisit the analysis of the low temperature hysteresis loop (Fig. 3.2b) characterizing a diluted crystal of $[TbPc_2]^{-1}$ SIMMs in an isostructural diamagnetic YPc_2 matrix (Tb to Y ratio of 1% [138]), measured with the micro-SQUID setup at subkelvin temperatures [123]. We show that despite the great progress made in the last decade and numerous studies that looked at the $TbPc_2$ complex [139], the tunneling dynamics of this system was still poorly understood. We investigate numerically different interactions that have the potential to promote tunneling transitions and show that the coupling of the electronic shell to the ^{159}Tb nuclear spin dominates the environmental and ligand field interactions.

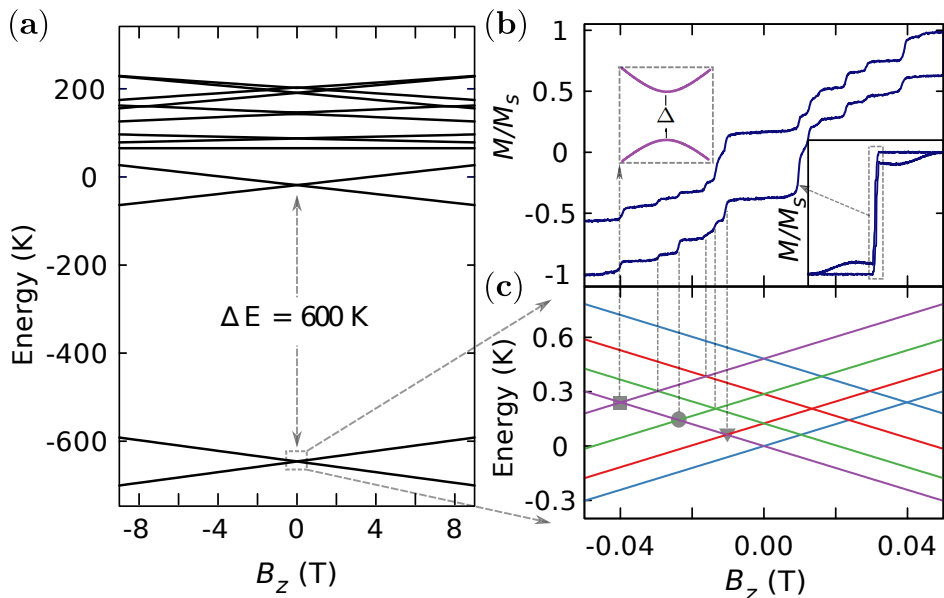


Figure 3.2: **a)** Zeeman diagram obtained by numerical diagonalization of the spin Hamiltonian given by Eq. (3.3). **b)** The magnetic hysteresis loop characterizing a crystal containing TbPc₂ SIMMs diluted in a diamagnetic, isostructural matrix formed by YPc₂ molecules, with [TbPc₂]/[YPc₂] ratio of 1 %. Upon sweeping the magnetic field from -1 T up to positive fields as small as 0.05 T, approximately 75 % of the TbPc₂ SIMMs undergo quantum tunneling transitions, resulting in sharp steps in the magnetization curve. The remaining SMM reverse their magnetic moment at larger magnetic fields by a direct relaxation process (*right inset*). The quantum tunnel transitions take place between mixed states of nuclear and electronic origin and are labeled by the change in the nuclear magnetic moment ($|\Delta m_I| = 0, 1$ and 2 shown as a square, circle, and triangle, respectively in the Zeeman diagram). The tunnel splitting (Δ) shown in the (*left inset*) quantifies the state mixing at resonance and is directly connected to the magnitude of the tunneling transition rates. **c)** Hyperfine structure of the lowest doublet, $m_J = \pm 6$ in the field region where tunneling transitions take place. The position of the relaxation steps are fitted to the corresponding level crossings in the Zeeman diagram by using $A_{\text{hyp}} = 26.7$ mK and $D_{\text{quad}} = 17$ mK.

Spin Hamiltonian

The TbPc₂ molecule (Fig. 3.1) features a Tb³⁺ ion sandwiched between two phthalocyanine planes in a square antiprismatic symmetry (D_{4d}), that is, the Tb³⁺ ion is coordinated by 4 nitrogen atoms from each ligand plane and the upper Pc ligand is a mirror reflection of the lower one (with respect to the x - y plane) rotated by 45° around the z -axis. The crystal field interaction generates a quantization axis oriented

perpendicular to the Pc planes and was modeled, with a certain degree of success, by the following Hamiltonian [135] (see Sect. 1.1):

$$\mathcal{H}_{\text{lf}} = \sum_{n=1}^3 B_{2n}^0 O_{2n}^0 + B_4^4 O_4^4 \quad (3.1)$$

The terms in the sum describe the uniaxial anisotropy while the O_4^4 term models a transverse ligand field interaction that arises from a broken D_{4d} symmetry. The diagonalization of \mathcal{H}_{lf} in the $|J, m_J\rangle$ eigenbasis reveals that the ligand field partially lifts the degeneracy of the $2J + 1$ substates in the ground state multiplet $J = 6$. The ground state doublet, $m_J = \pm 6$, is separated from the first excited doublet, $m_J = \pm 5$, by approximately 600 K (Fig. 1.3). Then, each m_J -doublet splits in an external magnetic field, the resulting Zeeman diagram being depicted in Fig. 3.2a. Therefore, at cryogenic temperatures, the $TbPc_2$ single molecule magnet behaves with a good approximation as an Ising spin system.

The Tb^{3+} ion also has a non-zero nuclear spin, $I = 3/2$, which couples to the surrounding electronic shell and further splits the ground doublet, $m_J = \pm 6$ in a manifold of four levels. The interaction is modelled by adding a hyperfine and a nuclear quadrupolar contribution to the spin Hamiltonian:

$$\mathcal{H}_n = A_{\text{hyp}}(\mathbf{J} \cdot \mathbf{I}) + \mathbf{I} \hat{D}_{\text{quad}} \mathbf{I} \quad (3.2)$$

Where $A_{\text{hyp}}(\mathbf{J} \cdot \mathbf{I})$ is the isotropic hyperfine interaction (Sect. 3.2), while the non-spherical charge distribution around the ^{159}Tb nucleus with a spin angular momentum $I = 3/2$ gives a non-negligible quadrupolar contribution, $\mathbf{I} \hat{D}_{\text{quad}} \mathbf{I}$. In the ideal case of a D_{4d} symmetry of the electronic shell, only the axial components ($\sim I_z$) need to be preserved. Thus, the total Hamiltonian that also includes the coupling to a magnetic field (\mathbf{H}), is given by the following expression:

$$\begin{aligned} \mathcal{H}_{\text{TbPc}_2} = & \mathcal{H}_{\text{lf}} + \mu_B \mu_0 \mathbf{H} \cdot (g_e \mathbf{J} + g_n \mathbf{I}) \\ & + A_{\text{hyp}} \mathbf{I} \cdot \mathbf{J} + \mathbf{I} \hat{D}_{\text{quad}} \mathbf{I} \end{aligned} \quad (3.3)$$

where the second term is the Zeeman interaction parametrized through the electronic ($g_e = 1.5$) and the nuclear ($g_n = 1.33$) gyromagnetic ratios. The A_{hyp} and the axial (dominant) term of \hat{D}_{quad} (D_{quad}) are uniquely determined by the positions of the relaxation steps (Fig. 3.2b) that are fitted to the corresponding level crossings in the Zeeman diagram (Fig. 3.2c), leading to $A_{\text{hyp}} = 26.7$ mK and $D_{\text{quad}} = 17$ mK.

Hysteresis loop

Figure 3.2a shows the magnetic hysteresis loop measured by using the μSQUID measurements (Chap. 2) on a crystal containing $TbPc_2$ SIMMs diluted in a diamagnetic,

isostructural matrix formed by YPc₂ molecules, with [TbPc₂]/[YPc₂] ratio of 1 %. Upon sweeping the magnetic field from -1 T up to positive fields as small as 0.05 T, approximately 75 % of the TbPc₂ SIMMs undergo quantum tunneling transitions, resulting in sharp steps in the magnetization curve. The remaining SMM reverse their magnetic moment at larger magnetic fields by a direct relaxation process [126]. Note the absence of a relaxation step at the level crossings found at zero external field. This is explained through Kramer's theory for half integer spin system that predicts degenerate ground states if only the ligand field is taken into account [55].

The quantum tunnel transitions take place between mixed states of nuclear and electronic origin and thus can be labeled by the change in the nuclear magnetic moment ($|\Delta m_I| = 0, 1$ and 2 shown in Fig. 3.2c as a square, circle, and triangle, respectively). The tunnel splitting (Δ in the inset of Fig. 3.2b) quantifies the state mixing at resonance and is directly connected to the magnitude of the tunneling transition rates [23]. Thus, the main objective of this paper is to evaluate Δ using numerical methods and this way to single out the interactions that promote tunneling relaxation between different hyperfine states.

Transverse interactions

In order to evidence the effect of the nuclear spin on the QTM dynamics of the TbPc₂, we first study the mixing of the electronic states due to non-axial interactions and then include the hyperfine splitting.

The effectiveness in mixing the electronic spin states by different order transverse interactions ($B_n J_{\pm}^n$) is shown in Fig. 3.3a. The qualitative character of $\Delta(B_n)$ characteristics can be understood using the tools of the perturbation theory which predicts that the tunnel splitting between the two lowest substates ($J_z = \pm 6$) follow the dependence:

$$\Delta \sim D J^2 \left(\frac{B_n J^n}{2D J^2} \right)^{12/n} \quad (3.4)$$

where D is the effective zero field splitting given by the diagonal terms in the ligand field (B_2^0, B_4^0 and B_6^0). The power law explains the difference in the amplitude needed for different order interactions to produce the same effect on the level mixing. Figure 3.3b shows the interplay between different transverse ligand field interactions as the transverse Zeeman interaction is increased linearly. The oscillations of the tunnel splitting with the applied transverse field are a consequence of the topological phase interference.

At this point, we can consider the complete spin Hamiltonian of the TbPc₂ complex (Eq. 3.3) that includes the interaction with the nuclear spin. The O_4^4 operator in

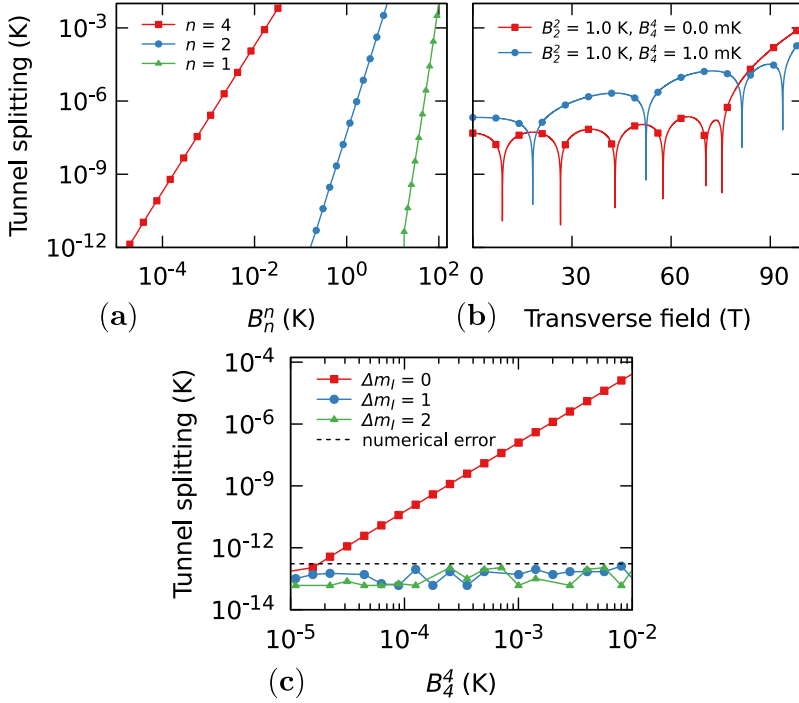


Figure 3.3: **a)** The effect of the transverse interactions of order n , ($B_n^n O_n^n = 1/2 B_n^n (J_+^n + J_-^n)$), on the tunnel splitting between the two lowest electronic levels ($J_z = \pm 6$). The first order interaction corresponds to the transverse Zeeman term ($1/2(J_+^n + J_-^n) = J_x$). **b)** The dependence of the tunnel splitting on the simultaneous action of the different interactions present in the system. The observed pattern of alternating maxima and minima corresponds to the topological phase interference resulting from the biaxial nature of the magnetic anisotropy. The fourth order transverse interaction tunes the amplitude and the period of the observed oscillations. **c)** The dependence of the tunnel splitting of the three types of anticrossings (denoted by the change of the nuclear spin, $|\Delta m_l| = 0, 1$ and 2) on the amplitude of the O_4^4 term in the ligand field interaction.

the ligand field Hamiltonian mixes ± 6 electronic states and transitions between them become allowed. By varying the B_4^4 parameter between 10^{-5} K and 10^{-2} K, the tunnel splitting corresponding to the crossings that conserves the nuclear spin vary between 10^{-12} K and 10^{-4} K, while all the other splittings remain negligible (Fig. 3.3c). This is not a surprising result as a fourth order perturbation can induce transitions only between states with a total spin that differ by a multiple of four. If this would be the sole non-axial interaction, only the transitions that conserve the nuclear spin will be observed – which is not our case.

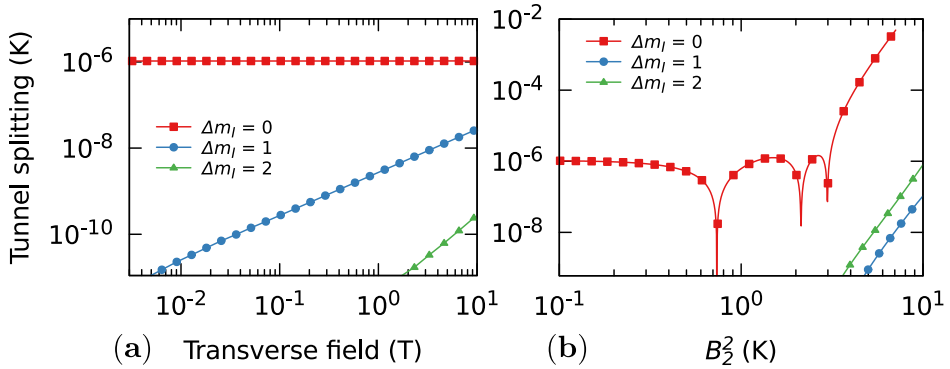


Figure 3.4: **a)** The effect of an applied transverse field on the tunnel splitting of the different hyperfine transitions. The transverse Hamiltonian includes also the fourth order perturbation with $B_4^4 = 6$ mK. **b)** An additional rhombic term ($B_2^2 O_2^2$) is added to the situation shown in the left panel, where we consider a constant transverse field, $H_x = 1$ mT. The observed oscillations are the result of the Berry phase interference [6].

One factor that is often invoked when explaining why the selection rules are not obeyed is the transverse component of the magnetic field that can be of both internal (*e.g.* dipolar field) or external (*e.g.* misaligned applied field) origin. When computing the tunnel splitting as a function of the applied transverse field (Fig. 3.4a), one observes that a field of at least 1 T is needed in order to have significant splittings pertaining to the crossings that do not conserve the nuclear spin (taking the ones that conserve the nuclear spin as a reference). This value is of course much larger than the environmental fields of dipolar origin. The dipolar field variance for our sample of 1 % concentration being around $\sqrt{\langle \Delta H_{\text{dip}}^2 \rangle} \approx 1$ mT. The necessity for such large values is easy to understand as the coupling between the magnetic field and the nuclear spin is weak due to the smallness of the nuclear magnetic moment.

The deviation from the tetragonal symmetry by the inclusion of a second order perturbation ($B_2^2 O_2^2$) was already done when the low temperature tunneling dynamics of Mn₁₂-ac was analyzed [140]. If one were to add also the biaxial term to the ligand field Hamiltonian (Eq. 3.3), the predicted dynamics of the $|\Delta m| = 1$ or 2 transitions would still remain orders of magnitude slower than the relaxation at the crossings that conserve the nuclear spin (Fig. 3.4b).

The reason why the above factors fail to explain the observed transitions lies in the magnitude of the different interactions described by Eq. 3.3. The effective total half integer spin comes from two heterogeneous spins that have a strong uniaxial

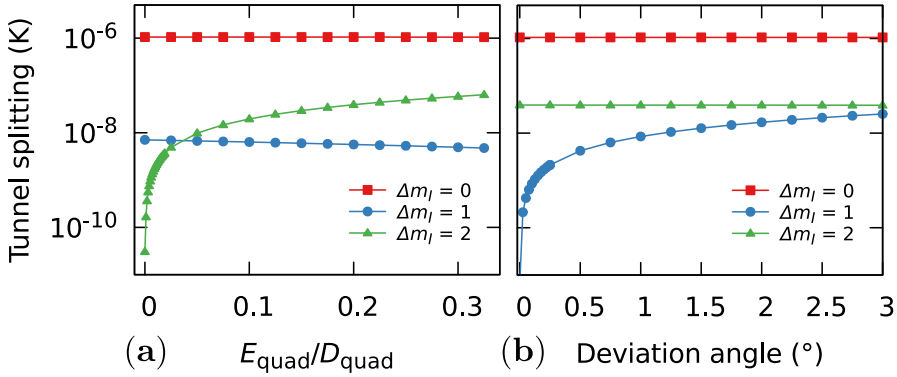


Figure 3.5: (a) Variation of the tunnel splitting with the rhombic term ($E_{\text{quad}}(I_x^2 - I_y^2)$) in the quadrupolar interaction, computed for a fixed angle misalignment between the ligand field and quadrupolar easy axis of 1° . From other transverse interactions only the O_4^4 term was kept, with $B_4^4 = 0.5$ K. (b) Variation of the tunnel splitting as a function of the misalignment between the ligand field and quadrupolar easy axis for $E_{\text{quad}}/D_{\text{quad}} = 0.2$ and the same O_4^4 term.

anisotropy and are tightly coupled through the hyperfine interaction. The hyperfine interaction does not promote transitions of both the electronic and nuclear spin (through terms like $A_{\text{hyp}}J_+I_-$) because the selection rules cannot be satisfied by both a nuclear and an electronic spin transition. While the electronic states are easily mixed by the ligand field, the nuclear states, to the first order, remain degenerate. Thus, in order to explain the observed steps in the magnetization curve, one needs to look at interactions that strongly couple to the nuclear spin.

Non-axial quadrupolar interaction

We suggest that a solution can be found in the quadrupolar interaction between the nucleus and the electronic shell. We already mentioned that if we consider a broken square antiprismatic symmetry we can add a biaxial term to the ligand field Hamiltonian. This entails us to include the biaxial term to the quadrupolar Hamiltonian as well, thus:

$$\mathbf{I}\hat{D}_{\text{quad}}\mathbf{I} = D_{\text{quad}}I_z^2 + E_{\text{quad}}(I_x^2 - I_y^2) \quad (3.5)$$

With this term, the states of the nuclear spin that differ by $|\Delta m_I| = 2$ become mixed and the entire ensemble's dynamics at the corresponding crossings is significantly enhanced (Fig. 3.5a). The odd transitions should still not be allowed. One has to

consider that there is a small misalignment between the uniaxial symmetry of the ligand field and the quadrupolar interaction which leads to terms of the form: $I_z I_{\pm}$.

Figure 3.5b shows the effect of the above described non-axial contributions. It can be seen that they act mostly independently of each other, as the biaxial term mixes the hyperfine states with $|\Delta m_I| = 2$ and the angle deviation mixes the states with $|\Delta m_I| = 1$. Thus, the non-axial quadrupolar interaction is a mechanism that can mix the hyperfine states and promote QTM transitions between the states that do not conserve the nuclear spin. This result is important both from an academic point of view as similar dynamics can be observed in other lanthanide single molecule magnets (see also Sect. 3.4), and from a technological one as tunneling between hyperfine states can be used to initialize and read-out the nuclear spins when implementing quantum protocols.

3.2 Decoherence Measurements in $TbPc_2$ SIMM

The coherent dynamics of an ensemble of weakly coupled spin systems is central to both the development of mesoscopic quantum physics [141, 70] and to the fast advancing field of quantum engineering [129, 90, 130]. Amongst solid state electron spin systems that are researched as potential quantum bits, (*e.g.* semiconductor quantum dots [142], nitrogen vacancies centers in diamond [143], molecular magnets, phosphorus or bismuth in silicon [144]), molecular magnets proved to be especially useful model systems. We saw in previous sections that many purely quantum phenomena like ground state tunneling [3], phonon and photon assisted tunneling transitions [4, 64], spin parity and quantum phase interference [6], phase coherence and Rabi oscillations [61] were analyzed in great detail in these systems.

When it comes to the study of decoherence, the common ground between different qubit systems is found in the description of the environment by standardized models like oscillatory or spin baths [141]. The main advantages of molecular magnets arise from their diversity and chemical tenability of the spin ground state and the intra- and intermolecular interactions (*e.g.* through the appropriate choice of the organic ligands) [127, 128]. Thus, one of the best characterized molecular system, the Fe_8 complex [8], was used to validate the theory of environmental decoherence against experiment [70]. In the above experiment, as well as, the breakthrough achievements like the first measurements of the spin relaxation times [72] and the observation of millisecond coherence time and Rabi oscillations at room temperature [73, 145, 111], electron paramagnetic resonance (EPR) was the technique of *choice*. However, the stringent requirement for a system to be susceptible to EPR investigation is a large coherence time [75]. In this section we show that using incoherent Landau-Zener tunneling dynamics [146] we are able to determine the intrinsic tunneling time and the decoherence rate, thus complementing the resonance techniques and providing a new tool to probe the quantum properties of molecules that could be candidates for implementing quantum bits.

We continue to analyze the magnetic response characterizing a diluted crystal of $TbPc_2$ lanthanide single ion molecular magnets. After writing an effective spin Hamiltonian for the $TbPc_2$ complex, we review the incoherent Landau-Zener formalism in which its dynamics is studied. Then, we describe the novel method by which we obtain the dependence of the tunneling transitions on the sweeping rate, alongside presenting the first experimental evidence of the thermalization of the ^{159}Tb nuclear spins. Finally, the phenomenological model proposed in Ref [146] is used to motivate the dynamics of the molecular spin and to study it quantitatively leading to experimental estimates of both the intrinsic tunneling time and the dephasing time.

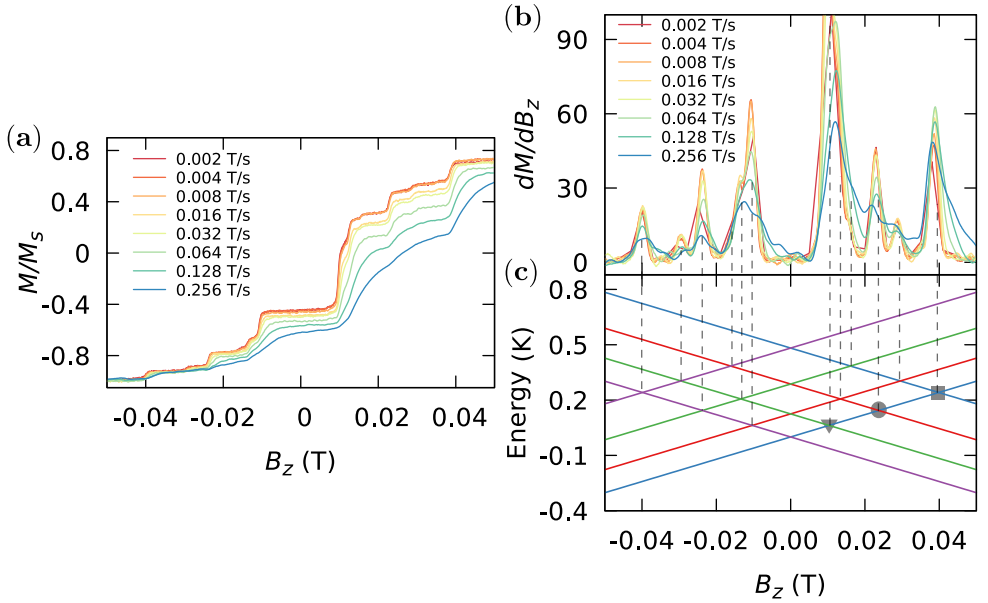


Figure 3.6: Sweeping rate dependence of **a)** the magnetization curves and **b)** their derivatives obtained after the sample was placed in $B_z = -1.3$ T for 2000 s at the cryostat temperature of 200 mK. The correspondence between the hyperfine anticrossings in the Zeeman diagram **c)** and the QTM steps seen as peaks in the derivative of the magnetization curves are marked with broken lines. The different anticrossings that correspond to $|\Delta m_l| = 0, 1$ and 2 nuclear selection rule are indicated by a square, circle and triangle, respectively. The adiabatic limit, $P_{LZ} \rightarrow 1$, predicted by the Landau-Zener model is not reached for slow sweeping rates, instead below 16 mT/s, all the $M(B_z; dB_z/dt)$ characteristics fall on the same curve.

Effective spin Hamiltonian

In section 3.1 it was shown that the strong uniaxial character of the ligand field interaction leads to a ground doublet, $m_j = \pm 6$, separated by about 600 K from the first excited doublet, $m_j = \pm 5$. As we work at subkelvin temperatures, the system is confined to the two lowest states, $m_j = \pm 6$, and thus the electronic spin can be treated as an effective Ising spin 1/2 with an effective g -value, $g_{\text{eff}} = 18$. Under an external field parallel to the anisotropy z -axis, the effective two level Hamiltonian describing the electronic states can be written as:

$$\mathcal{H}_e = \frac{g_{\text{eff}}}{2} \mu_B B_z \sigma_z + \frac{\Delta}{2} \sigma_x \quad (3.6)$$

Where the first term represents the longitudinal Zeeman interaction and the second one models the non-axial ligand field interactions. By including the nuclear spin interaction we have:

$$\mathcal{H}_{TbPC_2} = \mathcal{H}_e + A_{\text{hyp}}|m_J|(\boldsymbol{\sigma} \cdot \mathbf{I}) + \mathbf{I}\hat{P}_{\text{quad}}\mathbf{I} \quad (3.7)$$

Thus, the states are labelled by using the electronic and nuclear spin components, $|m_J, m_I\rangle$, with $m_J = \pm 6$ and $m_I = -3/2 \dots 3/2$.

At this point, two important observations need to be made. First, tunneling transitions within the doublet $m_J = \pm 6$ happen between mixed hyperfine states $|+6, m_I\rangle$ and $|-6, m_I'\rangle$. In a first approximation, we consider that tunneling transition events at different crossings are independent of each other, that is tunneling dynamics at a specific anticrossing affects only the populations of the two levels that form it. Second, the interaction between the electronic spin and nuclear spin results in the non-equidistant splitting of the energy levels, with the energy spacings between consecutive hyperfine states being around 120, 160 and 190 mK. These spacings are larger than the lowest temperature of about 25 mK reached with our dilution cryostat. This suggests that any initial distribution of the nuclear spin population thermalizes towards the equilibrium Boltzmann distribution.

Figure 3.11 shows equilibrium magnetization curves at different cryostat temperatures measured after the sample was kept for 4000s in $B_z = -1.3$ T applied magnetic field. The increase of the occupation number of the excited states is seen in the strong dependence of the QTM steps on temperature as the variation of the relaxation steps with temperature depends only on the initial population of the hyperfine levels (in a first approximation, P , is assumed to be independent of temperature). The detailed analysis of the thermalization process will be pursued in the next section.

Landau-Zener dynamics

The time evolution of the magnetic moment under a changing magnetic field is given by the following master equation for the density matrix (ρ):

$$\frac{d\rho}{dt} = \frac{i}{\hbar}[\rho, \mathcal{H}] \quad (3.8)$$

Thus, the spin reversal probability, for the case when the magnetic field is swept at a constant rate, is given by the Landau-Zener expression (Eq. 1.30):

$$P_{LZ} = 1 - \exp\left(-\frac{\pi\Delta^2}{\hbar\alpha}\right)$$

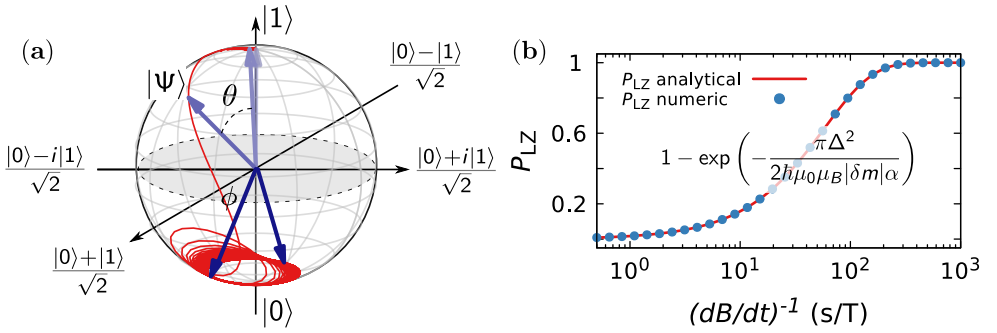


Figure 3.7: **a)** The trajectory of the molecular spin (*red curve*) on the Bloch sphere during the Landau-Zener dynamics. The initial state $|1\rangle$ and the intermediate states $|\Psi\rangle$ are indicated by blue arrows with the color gradient indicating the time dimension. The non-adiabatic evolution of the spin through the level anticrossing is a unitary coherent dynamics, reflected by the motion of the spin on the surface of the sphere. Far from the level anticrossing, a steady state precession ($\theta = \text{const}$) is reached. The LZ tunneling probability is given by: $P_{\text{LZ}} = \cos^2(\theta/2)$. **b)** Landau-Zener tunneling probability as a function of the sweeping rate. The continuous line represents the analytical solution to the LZ problem while the blue points are the numerical solution of Eq. 3.8.

where $\alpha = g_{\text{eff}}\mu_B dB_z/dt$ is the rate of change of the Zeeman interaction.

The usual approach to investigate experimentally the tunneling dynamics in molecular magnets is to measure the sweeping rate dependence of the relaxation steps. Figure 3.6a shows the TbPc₂'s magnetization curves obtained after a waiting time of 2000 s at the cryostat temperature of 200 mK for field sweeping rates in the range $dB_z/dt \in [1 : 256]$ mT/s. The correspondence between the hyperfine anticrossings in the Zeeman diagram and QTM steps seen as peaks in the derivative of the magnetization curves (Fig. 3.6b,c) are marked with dotted lines. Note that, $P_{\text{LZ}} \rightarrow 1$ limit predicted by the Landau-Zener model is not reached for slow sweeping rates, instead below 16 mT/s all the $M(B_z; dB_z/dt)$ characteristics fall on the same curve. This is not a surprising result as, Eqs. 3.8 and 1.30 have a limited domain of applicability, adequately describing the experimental reality only when the characteristic time of the experiment (the time the system is driven through resonance) is considerably smaller than the characteristic time of the environmental perturbation (*e.g.* dephasing time). The deviations from the Landau-Zener formalism are thus due to both elastic (dephasing) and inelastic (relaxation and excitation) processes.

The problem was recently analyzed using measurements performed on a single TbPc₂ molecule in a spin transistor geometry [146] and it was concluded that, in the limit of small probing currents, the dephasing processes dominates the system's

dynamics. The observed behaviour was successfully modeled by a phenomenological Lindblad operator formalism in which the dephasing process acts through the term $(2L\rho L^\dagger - L^\dagger L\rho - \rho L^\dagger L)$ added to the right hand side of Eq. 3.8:

$$\frac{d\rho}{dt} = \frac{i}{\hbar}[\rho, \mathcal{H}] + (2L\rho L^\dagger - L^\dagger L\rho - \rho L^\dagger L) \quad (3.9)$$

Thus, I shortly present the use of the Lindblad operator formalism in describing the decoherence dynamics.

Lindblad operators

I will first analyze the two limit cases that corresponds to dephasing processes between the diabatic or adiabatic states and then discuss the phenomenological model used to describe the LZ dynamics of $TbPc_2$ in a single molecule transistor environment.

The decoherence processes will be discussed in terms of a few parameters, namely, tunneling time, $\tau_\Delta = \frac{\hbar}{\Delta}$, the time systems is driven through anticrossings, $\tau_{ac} = \frac{\Delta}{\alpha}$, and the dephasing time, $\tau_d = \frac{1}{\gamma}$, where γ is the dephasing rate. Note that, a pure dephasing process changes the population of the electronic states by affecting the phase of the spins in their LZ dynamics and does not induce direct transitions between the eigenstates of the molecular spin.

In the first case, the Lindblad operator is given by:

$$L_a(t) = \frac{1}{2\sqrt{\tau_d}}[|\uparrow\rangle\langle\uparrow| - |\downarrow\rangle\langle\downarrow|] \quad (3.10)$$

where $|\downarrow\rangle, |\uparrow\rangle$ are the diabatic states.

The operator L_a describes a dephasing process that affects the linear superposition of the diabatic states and characterizes a strong coupling regime between the spin and environmental degrees of freedom. Figure 3.8a,b shows the time evolution of the spin initialized in the ground state and driven through the anticrossing, as a function of the dephasing time for slow $\tau_{ac} \gg \tau_\Delta$ and fast $\tau_{ac} \ll \tau_\Delta$ sweeping rates. The dynamics on the Bloch sphere computed by the numerical integration of Eq. 3.9 is shown in Fig. 3.8c. One can see that, the dephasing transforms the linear superposition of the diabatic states in a mixture of states. Thus, the decoherence process is especially effective in the slow sweeping rate limit, that is, $\tau_{ac} \gg \tau_\Delta$ while for fast sweeping rates the dynamics is close to the coherent Landau-Zener evolution.

The tunneling probability as a function of the sweeping rate for different dephasing times obtained by solving the master equation 3.9 is shown in Fig. 3.8d. Note that,

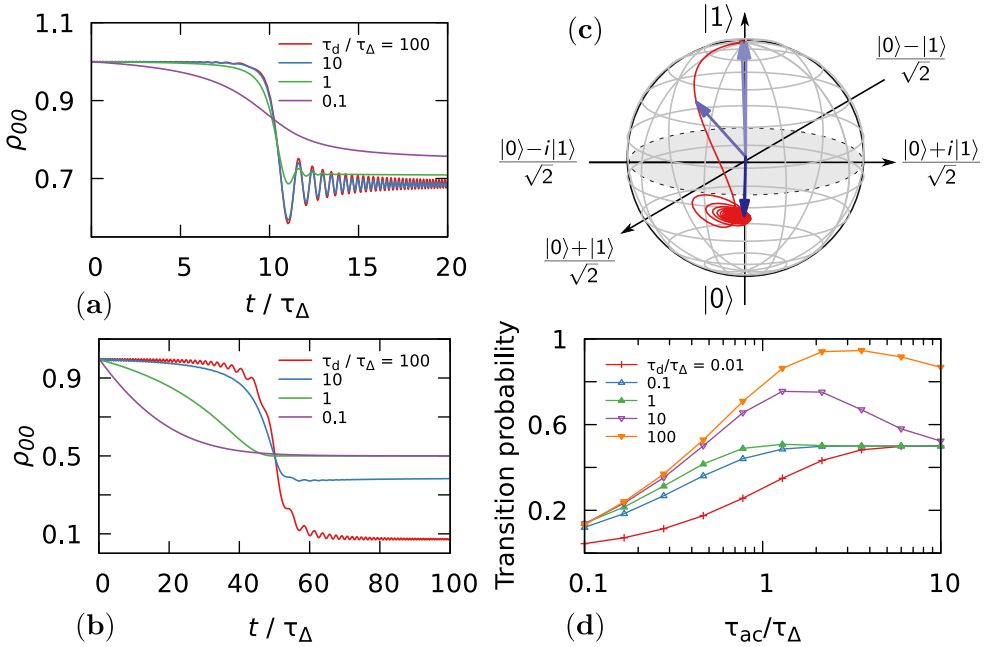


Figure 3.8: Time evolution of the population of the ground state when the system was initialized in the ground state and then driven through the anticrossing, as a function of the dephasing time, τ_d , for **a)** slow $\tau_{ac}/\tau_\Delta = 5$ and **b)** fast $\tau_{ac}/\tau_\Delta = 0.25$ sweeping rates, computed by the numerical integration of Eq. 3.9. The decoherence process is especially effective in the slow sweeping rate limit, $\tau_{ac} \gg \tau_\Delta$, while for fast sweeping rates and for $\tau_d > \tau_\Delta$, the dynamics is close to the coherent Landau-Zener evolution. **c)** LZ dynamics for $L = L_a$ shown on the Bloch sphere for $\tau_{ac}/\tau_\Delta = 10$ and $\tau_d/\tau_\Delta = 1$. The dephasing transforms the linear superposition of the diabatic states in a mixture of states. **d)** LZ tunneling probability as a function of the sweeping rate for different dephasing times. When $\tau_{ac} \approx \tau_d$, the interference between diabatic states is strongly affected and the system tends to a randomized state characterized by $P = 0.5$.

when the time the system is driven through the anticrossing becomes comparable to the dephasing time, the interference between diabatic states is strongly affected and the system tends to a randomized state characterized by $P = 0.5$.

The second case to consider is:

$$L_b(t) = \frac{\eta}{2\sqrt{\tau_d}} [|\epsilon_1(t)\rangle \langle \epsilon_1(t)| - |\epsilon_2(t)\rangle \langle \epsilon_2(t)|] \quad (3.11)$$

where $|\epsilon_{1,2}(t)\rangle$ are the time-dependent eigenstates of \mathcal{H} and $\eta = \langle \epsilon_1(t)| \sigma_z |\epsilon_1(t)\rangle$. This time, the Lindblad operator L_b describes a dephasing process between the adiabatic states and characterizes a weak coupling regime between the molecular spin and

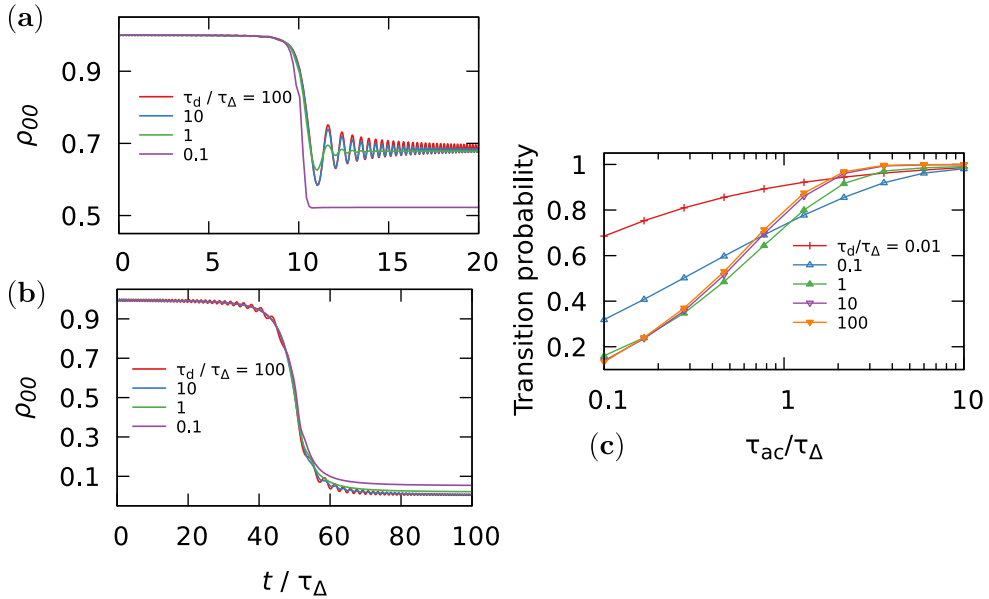


Figure 3.9: Time evolution of the population of the ground state when the system was initialized in the ground state and then driven through the anticrossing, as a function of the dephasing time, τ_d , for **a)** slow $\tau_{ac}/\tau_{\Delta} = 5$ and **b)** fast $\tau_{ac}/\tau_{\Delta} = 0.25$ sweeping rates, computed by the numerical integration of Eq. 3.9, with $L = L_b$. At low sweeping rates, where the evolution is close to an adiabatic one, the LZ dynamics is hardly affected by the decrease in the dephasing time. This is also seen in **c)** which displays the tunneling probability, P , as a function of sweeping rate for different dephasing times. In the adiabatic limit, P saturates to 1 and not to 0.5 as was the case for $L = L_a$.

environmental degrees of freedom. If not at resonance, the adiabatic and diabatic states tend to coincide and thus the Lindblad operators are very similar. This is not the case when the system is found at the anticrossing. For example, exactly at resonance L_b vanishes while L_a has its strongest impact on the dynamics.

This leads to different effects that the two classes of dephasing processes have on the LZ dynamics. For example, at low sweeping rates, where the evolution is close to an adiabatic one, the LZ probability of the spin when $L = L_b$ is only weakly affected by the decoherence processes (see Fig. 3.9). Thus, the tunneling probability in the adiabatic limit saturates to 1 and not to 0.5 as was the case for a decoherence process in the diabatic basis.

We are now in position to consider the phenomenological model introduced in Ref. [146], characterized by the Lindblad operator:

$$L_c(t) = \frac{1}{\tau_{av}} \int_{t-\tau_{av}}^{t+\tau_{av}} L_b(\tau) d\tau \quad (3.12)$$

The time constant, τ_{av} , was introduced as an interpolation parameter between the two limiting cases in which the environment affects the superposition of the diabatic or the adiabatic states [147, 146]. For example, for the limit cases $\tau_{av} \gg \tau_{ac}$ or $\tau_{av} \ll \tau_{ac}$, L_c tends to L_a and L_b , respectively, such that, one gets the above considered cases. Therefore, at different sweeping rates, different dephasing mechanism will affect the system's dynamics.

Figure 3.10b shows the sweeping rate dependence of the tunneling probability for different τ_{av} and a fixed $\tau_d = \tau_\Delta$. The characteristics can be understood by looking at the relative magnitude of τ_{av} with respect to τ_Δ and τ_{ac} . As long as τ_{av} is much smaller than τ_Δ the dephasing is dominated by processes that destroy the superposition of the adiabatic states.

For larger values of the averaging time, that is, for $\tau_{av} \approx \tau_\Delta$, the $P(dB/dt)$ characteristics change qualitatively and besides the plateau at zero and 1 a plateau at $P = 0.5$ appears. This indicates that, the dephasing affects the linear superposition of the diabatic states. Decreasing the sweeping rate even further, so that, $\tau_{av} < \tau_{ac}$ the tunneling probability starts to increase again and saturates to $P = 1$. This corresponds to the transition from a dephasing process between the diabatic states to one between the adiabatic states.

Figure 3.10a displays the dependence of the spin reversal probability on the dephasing time τ_d for fixed $\tau_{av} = 10\tau_\Delta$. As the dephasing time is decreased, the evolution of the molecular spin departs from the coherent LZ dynamics with the extra parameter τ_{av} marking the time scale on which a weaker coupling regime is reached.

Magnetization fit

We start the theoretical analysis by describing the numerical procedure by which we fit the magnetization curves and obtain the dependence of the tunneling probability at different level crossings, as a function of the field sweeping rate. We use the knowledge of the equilibrium Boltzmann distribution reached when the sample is thermalized in an external applied magnetic field, $B_z = -1.3$ T, and fit the magnetization curve to infer the tunneling probability.

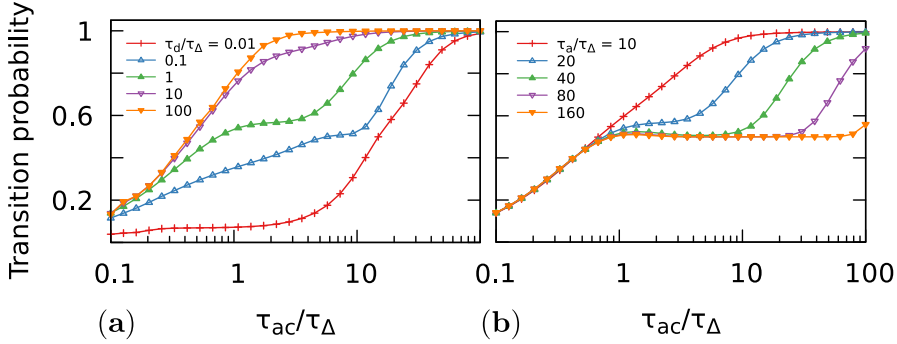


Figure 3.10: **a)** Sweeping rate dependence of the Landau Zener tunneling probability for the case $L = L_c$, for different dephasing times τ_d and a fixed $\tau_{av} = 10\tau_{\Delta}$. As the dephasing time is decreased, the evolution of the molecular spin departs from the coherent LZ dynamics with the extra parameter τ_{av} marking the time scale on which a weaker coupling regime is reached. **b)** The dependence of the spin reversal probability on different τ_{av} for a fixed $\tau_d = \tau_{\Delta}$. If $\tau_{av} \ll \tau_{\Delta}$ the dephasing is dominated by processes that destroy the superposition of the adiabatic states, and the dynamics hardly difference from the coherent one. For larger values of the averaging time, that is, $\tau_{av} \approx \tau_{\Delta}$, the $P(dB/dt)$ characteristics changes qualitatively and besides the plateau at zero and 1 a plateau at $P = 0.5$ appears. When $\tau_{av} < \tau_{ac}$ the tunneling probability starts to increase again and saturates to $P = 1$.

The model for $M(B_z)$ requires to keep track of the fractional populations of the hyperfine levels, $|m_J, m_I\rangle$, at an applied longitudinal field B_z , which we denote by $n(m_J, m_I; B_z)$. The initial state corresponds to the polarized sample in an applied field $B_z = -1.3$ T, thus, the only non-zero populations are the ones with $m_J = +6$. Note that, by definition, the fractional populations satisfy the relation:

$$\sum_{m_J, m_I} n(m_J, m_I; B_z) = 1 \quad (3.13)$$

The initial, equilibrium distribution is given by the Boltzmann distribution:

$$n_i^0 = \frac{\exp(-E_i/k_B T)}{Z} \quad (3.14)$$

With this notation, the normalized magnetization at an applied field B_z is given by:

$$M(B_z)/M_s = \sum_{m_J, m_I} -\frac{m_J}{|m_J|} n(m_J, m_I; B_z) \quad (3.15)$$

With $m_J = \pm 6$ and $m_I = -3/2 \dots 3/2$. As we sweep the magnetic field, the change in the population of the hyperfine states is assumed to happen only at level anticrossings in the Zeeman diagram (Fig. 3.6c) with the relation between the tunneling probability and magnetization step given by:

$$P_{LZ} = |\Delta M / (2M_{in})| \quad (3.16)$$

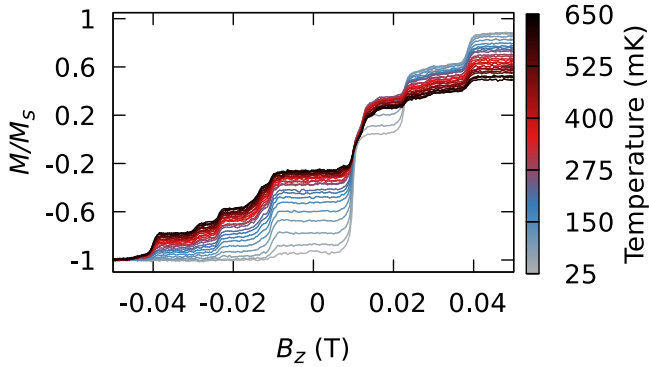


Figure 3.11: Equilibrium magnetization curves at different cryostat temperatures measured after the sample was kept for 4000 s in $B_z = -1.3$ T applied magnetic field. The increase of the occupation number of the excited states is seen in the strong dependence of the QTM steps on temperature as, in a first approximation, the variation of the relaxation steps with temperature depends only on the initial population of the hyperfine levels.

Where M_{in} is the initial magnetization of the states involved in the anticrossing and ΔM is the height of the relaxation step.

Before continuing with our analysis let's discuss the assumptions taken when constructing the above presented model for $M(B_z)$. First, it is considered that the tunneling probability does not depend on the sample's magnetization, that is, all collective processes can be neglected. Due to dilution, TbPc₂ molecules are coupled only by weak dipolar interactions which are assumed to have the sole effect of giving a finite width (taken from experiment to be around 1 mT) to the relaxation steps. Note that, if the dipolar field is quasistatic during the relaxation process of the individual molecular spins (as it is the case for diluted samples and small relaxation steps), the effect of the dipolar coupling is just to shift the time origin of the Landau-Zener process, with no effect on the dephasing process. Also, besides the dipolar broadening, the steps are artificially broadened due to the time constant of the feedback loop of the measurement process [123].

Another important limit is the characteristic time of the read-out technique (the time needed to sweep the $[-40 : 40]$ mT field range) which is around 40 s for the lowest sweeping rate of 2 mT/s, is much smaller than the characteristic relaxation times of the ¹⁵⁹Tb nuclear spin. This assumption is valid at low temperatures where the time needed to reach the thermal equilibrium is of the order of thousands of seconds (see Sect. 3.3) but starts to break down for temperatures larger than 300 mK. One has to remark that the rate of the electronic inter-well direct spin-phonon transitions also

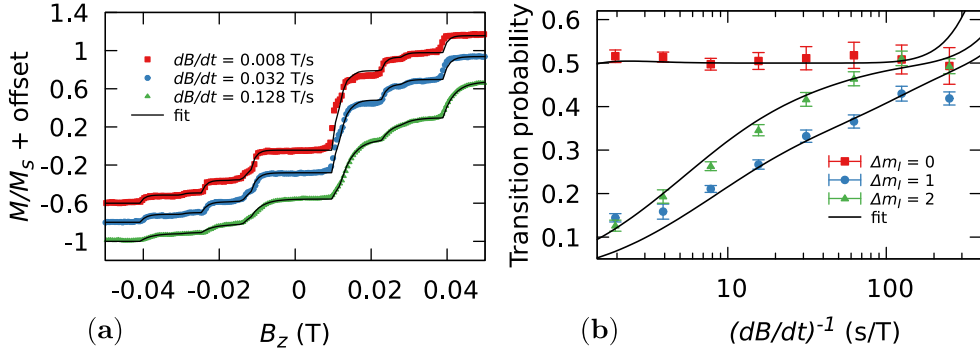


Figure 3.12: **a)** Magnetization curves for different sweeping rates, at 200 mK, fitted by theoretical curves (black lines). The fitting procedure leads to the spin flip probability corresponding to the 3 types of anticrossings ($\Delta m_l = 0, 1$ and 2). The curves were shifted vertically for a better visualization. **b)** Spin flip probabilities fitted to the dephasing model outlined in the text, leading to tunneling times of 4.78 and 3.47 μs for $\Delta m_l = 1, 2$, respectively and a dephasing time of 0.33 μs .

increases with temperature and constitutes another factor that limits the validity range of the presented technique.

Taking into account the above presented factors results in an almost perfect fit of the experimental curves, as seen in Fig. 3.12a. The determined transition probabilities are shown in Fig. 3.12b. It is important to notice that at very slow sweeping rates ($dB/dt \lesssim 5$ mT), the model for the magnetization curves starts to fail because the characteristic time of the experiment approaches the electronic and nuclear spin lattice relaxation times. Thus, we work in the sweeping rate range in which the tunneling dynamics dominates over the direct relaxation process.

In order to characterize the dephasing process, we solve numerically the above presented phenomenological master equation and fit the spin flip transition probabilities using a nonlinear least-square algorithm with three time constants: τ_Δ , τ_d and τ_{av} . As seen in Ref. [146], if we are far from the coherent Landau-Zener dynamics, then τ_d/τ_Δ and τ_{av}/τ_Δ parameters are uniquely defined by the shape of the $P(dB/dt)$ characteristic, while a variation of the tunneling time, τ_Δ , results in a horizontal shift along the sweeping rate axis. Additionally, to reduce the number of fit parameters, we make the requirement for τ_d and τ_{av} to be the same for $\Delta m_l = \pm 1$ and ± 2 transitions.

The transitions that conserve the nuclear spin ($\Delta m_l = 0$) are independent on the sweeping rate (in the range tested experimentally). The plateau at $P_0 = 0.5$ is characteristic of a dephasing process that comes from a strong interaction between

the system and its environment, so that the Lindblad operator is mostly constructed from the diabatic states [146]. The $\Delta m_I = 1$ and 2 transitions are well fitted by using tunneling times, ($\tau_\Delta \equiv \hbar/\Delta$), $\tau_\Delta = 4.78$ and $3.47 \mu\text{s}$, respectively, and with the same dephasing ($\tau_d = 0.33 \mu\text{s}$ or alternatively a decoherence rate $\gamma_d = 1/\tau_d \approx 3 \text{ MHz}$) and averaging time ($\tau_{av} = 93.7 \mu\text{s}$). The sweeping rate range for which the plateau of $P_0 = 0.5$ is observed for $\Delta m_I = 0$ means that the tunnel splitting for this anticrossing is at least one order of magnitude larger than the other two transitions (the fit curve is not uniquely defined for $\Delta m_I = 0$ transition).

The study in Ref. [146] and the present work share the same molecular complex but which is placed in very different environments. Thus, it is worthwhile to compare the measured low temperature dynamics. For the TbPc₂ molecule in a spin transistor geometry, tunneling events are observed only at the crossings that conserve the nuclear spin while for TbPc₂ in a single crystal environments, all the transitions except the ones at zero field are evidenced experimentally [135, 148]. This clearly shows that the molecules in the two samples are acted upon by different transverse terms. Also, the measured $P(dB/dt)$ characteristics differ significantly between the two experiments proving that the dynamics of a molecular spin driven through an avoided level crossing is strongly dependent on the coupling to its environment. In the former study, the conduction electrons that tunnel through the ligand quantum dot are expected to play the dominant role in the decoherence process, while for a molecular crystal at very low temperatures, the incoherent dynamics is caused mainly by the surrounding spin bath comprised of nuclear and other molecular spins. Establishing the connection between the phenomenological model that uses Lindblad operators and a microscopic description that includes explicitly the environmental degrees of freedom is an important outlook of the present study.

3.3 Nuclear spin lattice relaxation

In this section we investigate the thermalization of the ^{159}Tb nuclear spin. We use the acquired understanding on the LZ dynamics of its magnetization to develop a read-out technique for the population of the hyperfine states. Then, the time evolution of the population of the hyperfine states, obtained by fitting the magnetization curves, is evaluated in the framework of a Markovian master equation that allows us to discuss the dynamics in terms of spin-phonon relaxation rates. Finally, by evaluating the temperature dependence of the relaxation process we identify the main mechanism responsible for the thermalization of the nuclear spins. We find that a direct process that involves phonon modulation of the hyperfine interaction is sufficient to explain the magnitude of the determined relaxation rates.

Thermalization of ^{159}Tb nuclear spins

The experimental protocol used to evidence and investigate the thermalization of ^{159}Tb nuclear spins is shown in the inset of Fig. 3.13a. In order to start with a reproducible initial state we sweep back and forth through the zero field resonances until a demagnetized state, $M = 0$, is reached. Through this procedure, the nuclear spin population is heated-up to an effective temperature much higher than the cryostat temperature. The sample is then saturated in a high longitudinal magnetic field ($B_z = -1.3$ T). During this stage, the molecular spins population is completely polarized, that is, all the molecules will be characterized by $m_I = +6$ while the nuclear spin population remains out of equilibrium. The sample is kept polarized in $B_z = -1.3$ T for a definite time, called the *cooling time* (t_c). During this time the population of the ^{159}Tb nuclear spins is allowed to evolve towards thermal equilibrium. The last step is to read-out the nuclear spin states by inverting the applied field while measuring the $M(B_z)$ characteristic.

Figure 3.13a shows a zoom of the measured magnetization curves for increasingly larger cooling times. We can see that the steps corresponding to excited hyperfine states, ($m_I = +6, m_I > -3/2$) for $B_z < 0$ T, gradually diminish and then disappear as the system evolves towards thermal equilibrium. Describing the above highlighted dynamics is the main focus of the current section.

In the previous section we used the knowledge about the equilibrium Boltzmann distribution to fit the magnetization curve and infer the tunneling probability while in the present study we take advantage of the acquired understanding to obtain the time evolution of the population of the nuclear spin states. When studying the field sweeping rate dependence of the tunneling probability (P_{LZ}), we found a

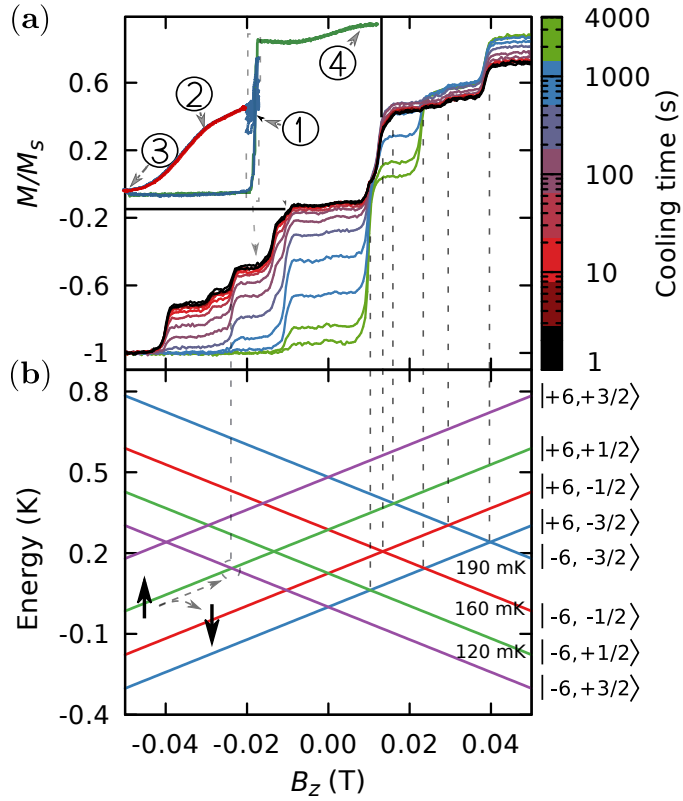


Figure 3.13: **a)** Magnetization curves of a diluted TbPc₂ crystal measured with the μ SQUID technique at 50 mK as a function of the time the sample is kept in $B_z = -1.3$ T (cooling time). The full procedure to measure these magnetization curves is shown in the inset: (1) initialize the sample by sweeping through the zero field resonances multiple times until the $M = 0$ state is reached, (2) saturate the sample, (3) wait a certain time for nuclear spins to thermalize and (4) read-out the hyperfine populations by inverting the magnetization while measuring $M(B_z)$. **b)** Hyperfine structure of the ground doublet, $m_j = \pm 6$, as a function of the applied longitudinal field obtained after numerical diagonalization of the Hamiltonian given by Eq. (3.7). The large black arrows are meant to illustrate how the ^{159}Tb transitions from the state $|+6, +1/2\rangle$ to the state $|+6, -1/2\rangle$ during the thermalization process are seen in the magnetization curve as a decrease in the magnitude of the relaxation step.

behaviour qualitatively different from the predicted Landau-Zener dynamics of an isolated spin. The observed tunneling relaxation was shown to be dominated by the environmentally induced decoherence with the central feature for the present study being the $P_{LZ} \rightarrow 0.5$ limit observed at small sweeping rates (compared to $P_{LZ} \rightarrow 1$ expected for the adiabatic limit of the Landau-Zener dynamics).

The analysis of the hysteresis curves is done following the same procedure as described in the previous section. The fit of the magnetization curve through Eq. 3.15 for different t_c at fixed T and fixed t_c with varying T is shown in Fig. 3.14 with the population of the hyperfine states (n_i), as fit parameters. A good agreement between the model and the experimental data is observed for $T < 300$ mK for all values of t_c .

Figure 3.15 shows the time evolution of the population of the hyperfine states as a function of t_c at different temperatures obtained from the fit of the $M(B_z)$ characteristics. We can see that the initial state corresponds indeed to a strongly non-equilibrium configuration, the populations of the hyperfine states being close to equal. Also, at 50 mK, the relaxation is rather slow as the equilibrium Boltzmann distribution is reached on the time scale of thousands of seconds. Another observation regards the population of $|+6, -1/2\rangle$ state (and to some degree of $|+6, +1/2\rangle$) which remains practically unchanged during the initial phase of the thermalization process. This suggests that the relaxation process that brings the system to the equilibrium Boltzmann distribution follows the selection rule: $\Delta m_I = \pm 1$.

To get further insight into the relaxation process(es) that dominates the observed dynamics, we model the thermalization of the nuclear spins in $B_z = -1.3$ T where the sample is polarized. For this, we make use of a standard master equation for a memoryless, Markovian evolution:

$$\frac{d}{dt}n(m;t) = \sum_{q=m\pm 1} [\gamma_q^m n(q;t) - \gamma_m^q n(m;t)] \quad (3.17)$$

Where m and q denote the hyperfine states and take values between $-3/2 \dots 3/2$ while $m_J = +6$ for all the states involved in the relaxation. γ_q^m coefficients denote the transition rate from the state $|+6, q\rangle$ to the state $|+6, m\rangle$. The relaxation rates γ_q^m obey the detailed balance condition:

$$\gamma_m^{m'}/\gamma_{m'}^m = \exp(\beta(E(m) - E(m'))) \quad (3.18)$$

with $\beta = 1/(k_B T)$. The sum in (3.18) is taken only over the nearest neighbour levels to reflect the above selection rule and reduce the number of fit parameters. The fit of the master equation (3.18) to the thermalization process at different temperatures is shown as black lines in Fig. 3.15 with the three de-excitation rates, γ_m^{m-1} (from now on denoted simply γ_m) as the only fitting parameters.

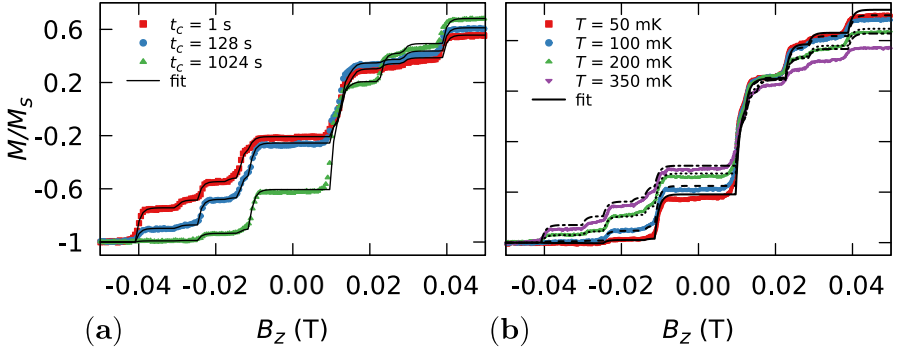


Figure 3.14: Fit of the magnetization curves measured with $dB_z/dt = 8$ mT/s and (a) fixed $T = 50$ mK for different cooling times, b) fixed $t_c = 1024$ s for different T . The fitting parameters are the initial populations of the hyperfine states and the relaxation is assumed to be dominated by incoherent quantum tunneling events occurring with the probability, $P_{LZ} = 0.5$. A good agreement between the model and the experimental data is observed for $T < 300$ mK for all values of t_c .

In order to identify the relaxation process we repeat the above presented analysis for temperatures up to 300 mK where the model for the magnetization curve starts to break down and the estimation of the population of the hyperfine states is no longer accurate (see Fig. 3.14).

Figure 3.16a shows the obtained temperature dependence of the relaxation rates. The transition rates increase with the spacing between the hyperfine levels. Also, for temperatures roughly smaller than 100 mK, the relaxation process becomes temperature independent. This suggests that the transition rates are determined by the sum of a spontaneous and an induced process. Thus, considering a pair of adjacent hyperfine levels, $|+6, m\rangle$ and $|+6, m-1\rangle$, separated in energy by ΔE_m , the transition rate γ_m can be expressed as:

$$\gamma_m = \mathcal{F}(\Delta E_m) \frac{\exp(\beta \Delta E_m)}{\exp(\beta \Delta E_m) - 1} \quad (3.19)$$

The fit curves are shown in Fig. 3.16a as black lines with $\mathcal{F}(\Delta E_m) = 1.09, 3.81$ and 8.86 ($\times 10^{-3} \text{s}^{-1}$) for the three de-excitation transitions, γ_m , with $m = -1/2, 1/2$ and $3/2$. The expression (3.19) works especially well at low temperatures ($T \lesssim 200$ mK) while the deviations that we start to see at higher temperatures suggest that the inclusion of higher order processes (*e.g.* Raman or Orbach mechanisms [14]) may play a role in the relaxation dynamics.

We can also compute the lifetime, τ_m , of each hyperfine level through the expression: $1/\tau_m = (\gamma_m^{m-1} + \gamma_m^{m+1})$. Figure 3.16b shows the evaluation of the lifetime of the

hyperfine levels using the determined relaxation rates from the master equation and also by using the above expression (black lines in Fig. 3.16b). As one can expect, in the $T \rightarrow 0$ limit, the lifetime of the ground state, $|+6, -3/2\rangle$ becomes infinite, as there are no phonons with sufficient energy to excite the nuclear spin, while the finite lifetime of the excited states are determined by the spontaneous emission process.

In order to interpret $\mathcal{F}(\Delta E_m)$, the coupling mechanism between the nuclear spins and phonon bath should be considered. The electronic shell of the Tb^{3+} ion couples to the lattice vibrations through the ligand field interaction, while the link between the electronic configuration and the ^{159}Tb nuclear spins is made through the hyperfine (mainly the spin orbit term) and quadrupolar interactions.

Thus, we follow Ref. [23, 42] and compute the transition rates induced by the phonon modulation of the nuclear spin Hamiltonian:

Nuclear spin phonon relaxation rate

Phonons transform any position vector \mathbf{r} into $\mathbf{r} + \mathbf{u}$ where \mathbf{u} is called the displacement field. If one considers a rotation of the crystal characterized by the vector $\mathbf{\Omega}$ then:

$$\mathbf{\Omega} = -\frac{1}{2}\nabla \times \mathbf{u} \quad (3.20)$$

The dominant energy at the nuclear site is the isotropic hyperfine interaction, $\mathcal{H} = A_{\text{hyp}}I_zJ_z$. If \hat{k} is the unit vector of the easy axis then after the rotation $\mathbf{\Omega}$ transforms into $\hat{k}' = \hat{k} + \mathbf{\Omega} \times \hat{k}$. The hyperfine term $A_{\text{hyp}}(\mathbf{J} \cdot \hat{k})(\mathbf{I} \cdot \hat{k})$, transforms into:

$$\mathcal{H}' = A_{\text{hyp}}(\mathbf{J} \cdot \hat{k}')(\mathbf{I} \cdot \hat{k}') = A_{\text{hyp}}(J_z + J_x\Omega_y - J_y\Omega_x)(I_z + I_x\Omega_y - I_y\Omega_x) \quad (3.21)$$

We neglect terms proportional to $J_{x,y}$ because we keep the sample polarized in high fields and, at sub-kelvin temperatures, phonons do not have enough energy to induce transitions of the electronic spin. We are also interested in evaluating first order effects, thus we also ignore terms $\propto I_\alpha I_\beta$ with $\alpha, \beta = x, y, z$.

The Hamiltonian becomes:

$$\mathcal{H}' = A_{\text{hyp}}J_zI_z + A_{\text{hyp}}J_z(I_x\Omega_y - I_y\Omega_x) \quad (3.22)$$

Thus, the perturbation induced by a uniform rotation $\mathbf{\Omega}$ is:

$$\delta\mathcal{H} = \mathcal{H}' - \mathcal{H} = A_{\text{hyp}}J_z[(\partial_x u_z - \partial_z u_x)I_x + (\partial_y u_z - \partial_z u_y)I_y] \quad (3.23)$$

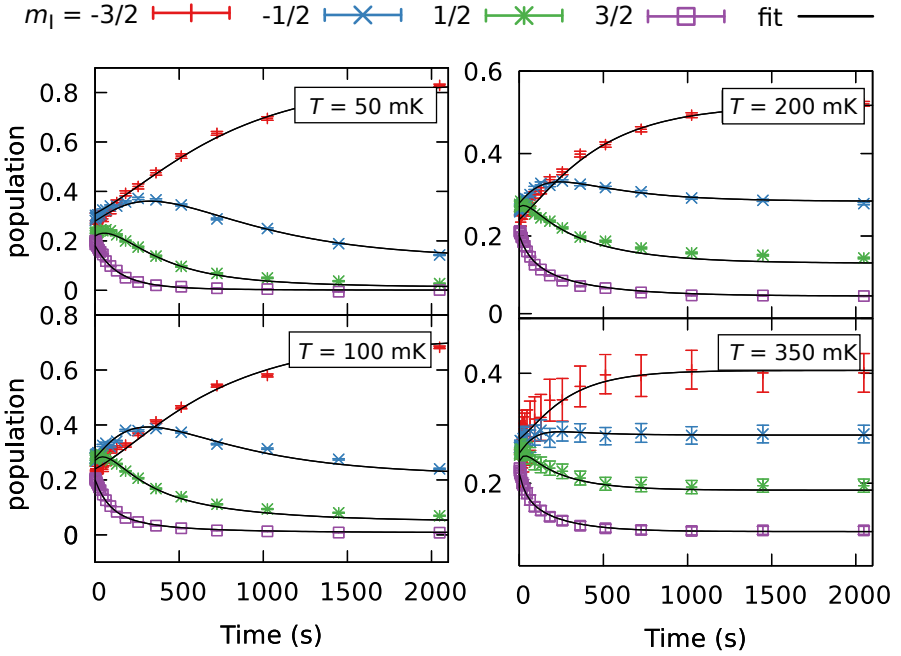


Figure 3.15: Evolution towards thermal equilibrium of the populations of the hyperfine levels at 50 mK, 100 mK, 150 mK and 200 mK obtained from the fit of the $M(B_z)$ characteristics. The initial state corresponds to a strongly non-equilibrium configuration with the populations of the hyperfine states being close to equal. At 50 mK, the relaxation is rather slow as the equilibrium Boltzmann distribution is reached on the time scale of thousands of seconds. The relaxation dynamics is evaluated in the context of the master equation (3.17), with the black lines showing the resulting fit. The only fitting parameters are the de-excitation transition rates, γ_m .

The Fourier transform of the displacement field is:

$$\mathbf{u}(\mathbf{r}) = \frac{1}{\sqrt{N}} \sum_{\mathbf{q}} \mathbf{u}(\mathbf{q}) e^{i\mathbf{q}\cdot\mathbf{r}} \quad (3.24)$$

where N is the number unit cells and \mathbf{q} are reciprocal vectors and obtain:

$$\delta\mathcal{H} = -\frac{iA_{\text{hyp}}J_z}{2\sqrt{N}} \left\{ [(q_x u_z - q_z u_x) - i(q_y u_z - q_z u_y)] I_+ + [(q_x u_z - q_z u_x) + i(q_y u_z - q_z u_y)] I_- \right\} \quad (3.25)$$

The transitions rates (γ_m) from the state $|m\rangle$ to the state $|m-1\rangle$, a process in which the spin relaxes and a phonon is emitted, is computed by using Fermi's golden rule:

$$\gamma_m = \frac{2\pi}{\hbar} \sum_{\mathbf{q}} |\langle \mathbf{n}_{\mathbf{q}} + 1, m-1 | \delta\mathcal{H} | \mathbf{n}_{\mathbf{q}}, m \rangle|^2 \delta_- \quad (3.26)$$

where $\delta_- = \delta(\hbar\omega_{\mathbf{q}} - (E_m - E_{m-1}))$ and $\mathbf{n}_{\mathbf{q}}$ denotes the number of phonons characterized by the wave vector \mathbf{q} and energy $\hbar\omega_{\mathbf{q}}$.

To evaluate Eq. 3.26 one uses the canonical transformation: $\mathbf{u} = \sqrt{\frac{\hbar}{2M\omega}} (\mathbf{c}^\dagger + \mathbf{c})$ together with the properties of the ladder operators:

$$\begin{aligned} c |n\rangle &= \sqrt{n} |n-1\rangle \\ c^\dagger |n\rangle &= \sqrt{n+1} |n+1\rangle \\ S_\pm |s, m\rangle &= \sqrt{(s \mp m)(s \pm m + 1)} |s, m \pm 1\rangle \end{aligned} \quad (3.27)$$

Thus, one obtains:

$$\gamma_m = \frac{\pi}{4} \frac{A_{\text{hyp}}^2 m_J^2 s_-}{NM} \sum_{\mathbf{q}} \frac{1}{\omega_{\mathbf{q}}} [(q_x - q_z) - i(q_y - q_z)]^2 (n_{\mathbf{q}} + 1) \delta_- \quad (3.28)$$

where $s_- = (s+m)(s-m+1)$.

By using the thermal average for the phonon modes: $\langle n_{\mathbf{q}} \rangle = 1/(e^{\beta\hbar\omega_{\mathbf{q}}} - 1)$ with $\beta = 1/(k_B T)$, and the continuous approximation: $(1/N) \sum_{\mathbf{q}} \rightarrow (a^3/(2\pi)^3) \int d^3q$ one gets:

$$\gamma_m = \frac{A_{\text{hyp}}^2 m_J^2 s_-}{32\pi^2 \rho} \int d^3q \frac{1}{\omega_{\mathbf{q}}} \frac{e^{\beta\hbar\omega_{\mathbf{q}}}}{e^{\beta\hbar\omega_{\mathbf{q}}} - 1} [(q_x - q_z)^2 + (q_y - q_z)^2] \delta_- \quad (3.29)$$

where $\rho = M/a^3$ is the crystal density.

The change to spherical coordinates gives:

$$\gamma_m = \frac{A_{\text{hyp}}^2 m_J^2 s_-}{6\pi\rho} \int dq \frac{q^4}{\omega_{\mathbf{q}}} \frac{e^{\beta\hbar\omega_{\mathbf{q}}}}{e^{\beta\hbar\omega_{\mathbf{q}}} - 1} \delta_- \quad (3.30)$$

Finally, by using the Debye model, $\omega_{\mathbf{q}} = cq$ where c is the sound velocity, one gets:

$$\gamma_m = \frac{A_{\text{hyp}}^2 m_J^2 s_- \Delta E_m^3}{6\pi\rho c^5 \hbar^4} \frac{e^{\beta\Delta E_m}}{e^{\beta\Delta E_m} - 1} \quad (3.31)$$

where $\Delta E_m = E_m - E_{m-1}$.

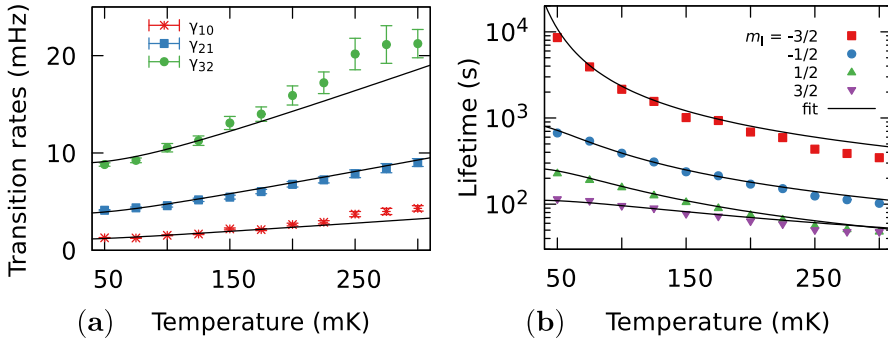


Figure 3.16: **a)** Temperature dependence of the relaxation rates fitted to a direct relaxation process characterized by a spontaneous and a induced component and given by Eq. (3.19). **b)** Temperature dependence of the lifetime of the hyperfine levels computed by using: $1/\tau_m = (\gamma_m^{m-1} + \gamma_m^{m+1})$. The continuous lines denote the evaluation of the level lifetimes. In the $T \rightarrow 0$ limit, the lifetime of the ground state, $|+6, -3/2\rangle$, becomes infinite, while τ_m of the excited states are mainly determined by the spontaneous emission process.

$$\mathcal{F}(\Delta E_m) = \frac{m_l^2 \delta A_{\text{hyp}}^2 \Delta E_m^3}{6\pi \hbar^4 \rho c^5} (I(I+1) - m(m-1)) \quad (3.32)$$

Where ρ is the crystal density and c is the sound velocity.

To our knowledge, measurements of both ρ and c in TbPc₂ crystals were not reported so far, thus one has to take them as free parameters. Especially, variations in the sound velocity will have a big impact on the relaxation rate as it enters in Eq. 3.31 to the fifth power. Also, the Debye model (a linear dispersion for the acoustic phonon modes) used in the derivation is an over-simplification. However, as we miss the value of ρ and the details on the lattice modes, we will be content with a rough estimation of the order of magnitude of the relaxation rates. Thus, by using Eq. (3.31) for the evaluation of $\gamma_{-1/2}$ at 50 mK we get: $\rho c^5 \approx 3.5 \times 10^{19} \text{ kg} \cdot \text{m}^2/\text{s}^5$. And by setting a sensible value for $\rho = 1500 \text{ kg}/\text{m}^3$, we obtain $c = 1877 \text{ m}/\text{s}$, which is a reasonable enough value (for example, $c = 1450 \text{ m}/\text{s}$ was used to explain phonon-assisted tunneling in Mn₁₂-ac [42]) to confirm the proposed mechanism for the thermalization process.

Nuclear pin phonon transitions in SMM

The identified direct relaxation channel between the ¹⁵⁹Tb nuclear spins and the phonon bath is a rather unexpected find for the relaxation of a nuclear spin embedded in a molecular complex. For example, measurements on ⁵⁵Mn nuclear spins at the core

of Mn_{12} -ac SMM were used to check the predictions of the spins bath theory for the dynamics of *molecular spin–nuclear bath* coupled system[149]. Most of the observed phenomenologies, with the exception of ^{55}Mn thermalization, were successfully explained. It was suggested that ^{55}Mn nuclear spins thermalize through the quantum dynamics of the molecular spins because the spin lattice interactions were found inefficient to explain the measured relaxation rates. However, so far no theoretical solution to this problem was found. The relaxation mechanism that we evidence for ^{159}Tb is not efficient in the case of ^{55}Mn nuclear spins because the hyperfine interaction in transition metal ion compounds is around one order of magnitude smaller.

Another interesting example to consider is the spin lattice relaxation of ^{159}Tb in $TbPc_2$ molecular spin transistor geometry[83]. The relaxation process, with a characteristic time of tens of seconds, was found to be dominated by the interaction with the electrons that tunnel through the molecular quantum dot. The comparison between the two experiments, that share the same molecular complex placed in very different environments, suggests that the direct relaxation mechanism that we highlight in this work sets the lower limit for the nuclear relaxation rate in potential lanthanide SMMs based spintronics devices.

3.4 Electronic and nuclear spin dynamics in Tb_2Pc_3 dinuclear SMM

In the previous sections we explored quantum phenomenologies seen in lanthanide molecular magnets by using the $TbPc_2$ molecule as a model system. We made the case that the displayed phenomenologies are prototypical for other lanthanide SMMs. In this section we show that the ferromagnetic interaction between the electronic spins in a dinuclear complex, $Tb_2Pc^{Hx8}Pc_2$ (from here on referred as Tb_2Pc_3) increases the multiplicity of nuclear spin states and that their state can be read-out through cooperative tunneling of the electronic spins (co-tunneling). The measurements on Tb_2Pc_3 will also be used to show that the compound exhibits relaxation QTM steps induced by the nuclear quadrupolar interaction. Also, nuclear spin-lattice relaxation processes, given by the modulation of the hyperfine interaction, are observed,

Tb_2Pc_3 SMM

Details on the synthesis and structural characterization of the molecule are found in Ref. [2]. The Tb_2Pc_3 is an asymmetric, dinuclear compound with one Tb^1 ion sandwiched between Pc^{Hx8} and a Pc plane while the second Tb^2 ion is found between two Pc planes (see Fig. 3.17). The point symmetry at the metal sites can be approximated to a square antiprism symmetry with CShM of 2.553 for Tb^1 and CShM of 1.593 for Tb^2 . Thus, a significant deviation from the ideal D_{4d} symmetry (even more so than in the case of $TbPc_2$) is observed (see Fig. 3.18).

The molecules crystallize in the monoclinic $P2_1/c$ space group with four molecules in the unit cell. Two molecules are related by an inversion symmetry and the other two are generated by glide and skew plane symmetry operations. There is a small angle of about 6° between the easy axis of the molecules in the two groups. The intramolecular Tb-Tb distance is 3.52 \AA while the shortest intermolecular Tb-Tb distance is 10.85 \AA , leading to a small couplings between the individual SMMs and to a significant magnetic interaction between the Tb ions of the same molecule. To further reduce the spin-spin interactions between different molecular units, we performed measurements on diluted samples with the host matrix made of $Y_2Pc^{Hx8}Pc_2$.

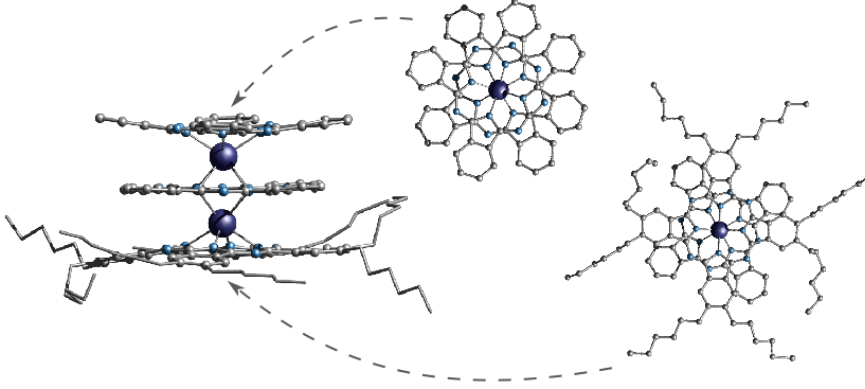


Figure 3.17: Side and top views of the $Tb_2Pc^{Hx8}Pc_2$ complex that encapsulates one Tb^1 ion sandwiched between Pc^{Hx8} and a Pc plane and a second Tb^2 ion found between two Pc planes. The point symmetry at the metal sites can be approximated to a square antiprism symmetry with CShM of 2.553 for Tb^1 and CShM of 1.593 for Tb^2 . Color code: Tb, dark blue; N, cyan; C, gray. H atoms are omitted for clarity.

Spin Hamiltonian

The spin Hamiltonian of the compound is written as:

$$\mathcal{H} = \mathcal{H}_{Tb^1} + \mathcal{H}_{Tb^2} + \mathcal{H}_{exc} \quad (3.33)$$

Where

$$\mathcal{H}_{Tb} = \mathcal{H}_{lf} + g_J \mu_B \mu_0 \mathbf{H} \cdot \mathbf{J} + A_{hyp} (\mathbf{J} \cdot \mathbf{I}) + \mathbf{I} \hat{P}_{quad} \mathbf{I} \quad (3.34)$$

is the Hamiltonian characterizing each individual Tb ion with

$$\mathcal{H}_{lf} = B_2^0 O_2^0 + B_4^0 O_4^0 + B_4^4 O_4^4 + B_6^0 O_6^0 \quad (3.35)$$

describing the ligand field interaction (the indexes indicating the individual ions were dropped to simplify the notation).

$$\mathcal{H}_{exc} = \mathbf{J}_1 \hat{A}_d \mathbf{J}_2 \quad (3.36)$$

describes the ferromagnetic interaction between the ions with \hat{A}_d containing both dipolar and exchange contributions. The Steven's coefficients were obtained by simultaneous fit of ac-susceptibility and NMR measurements on a similar Tb dinuclear compound [151]. The B_k^q parameters are slightly different for each Tb site reflecting the asymmetry of the molecule.

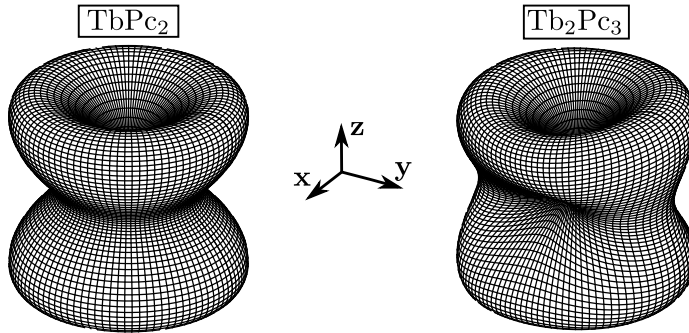


Figure 3.18: The comparison between the ligand field anisotropy of the Tb ion in $TbPc_2$ SMM and Tb^2 in $Tb_2Pc^{Hx8}Pc_2$ computed in the classical approximation of the spin Hamiltonian. The distorted electronic environment of the Tb ions is taken into account through the $B_4^4O_4^4$ term. $B_4^4 = 11.78 \times 10^{-2}$ K for Tb^2 in $Tb_2Pc^{Hx8}Pc_2$ and $B_4^4 = 17.6 \times 10^{-4}$ K for the Tb ion in $TbPc_2$ SMM. Despite the large difference between the off-diagonal terms, the uniaxial symmetry of the Tb ions in the Tb_2Pc_3 compound is preserved and their ground state is well defined as $m_J = \pm 6$.

The distorted electronic environment of the two Tb ions is taken into account through the $B_4^4O_4^4$ term with $B_4^4 = 11.78 \times 10^{-2}$ K which is two orders of magnitude larger than the value found for the $TbPc_2$ sibling molecule, $B_4^4 = 17.6 \times 10^{-4}$ K. Despite the large difference, the uniaxial symmetry of the compound is preserved (see Fig. 3.18) and the ground state for each Tb ion is well defined as $m_J = \pm 6$.

Due to the slight difference of the electronic environments of Tb^1 and Tb^2 , the A_{hyp} and \hat{P}_{quad} terms are expected to be different for each ion. However, in a first approximation, we can assume that they are equal. This allows to compute the dominant axial components of the hyperfine and quadrupolar interaction by fitting the steps in the magnetization curves and we obtained $A_{hyp} = 0.03$ K and $P_{quad} = 0.014$ K. Note that, A_{hyp} and P_{quad} are slightly different when compared to the values obtained for the $TbPc_2$ complex ($A_{hyp} = 0.0267$ K and $P_{quad} = 0.017$ K), showing that the ligand field gives the important contribution to the effective coupling between the Tb molecular and nuclear spin.

We work in the diabatic basis $|J_z^1, I_z^1\rangle |J_z^2, I_z^2\rangle$ and diagonalize the spin Hamiltonian as a function of the longitudinal applied magnetic field. The Zeeman diagram displayed in Fig. 3.20c results in 100 level crossings close to zero field characterized by simultaneous flip of the electronic and nuclear spins:

$$|+6, m^1\rangle | +6, m^2\rangle \rightarrow | -6, n^1\rangle | -6, n^2\rangle \quad (3.37)$$

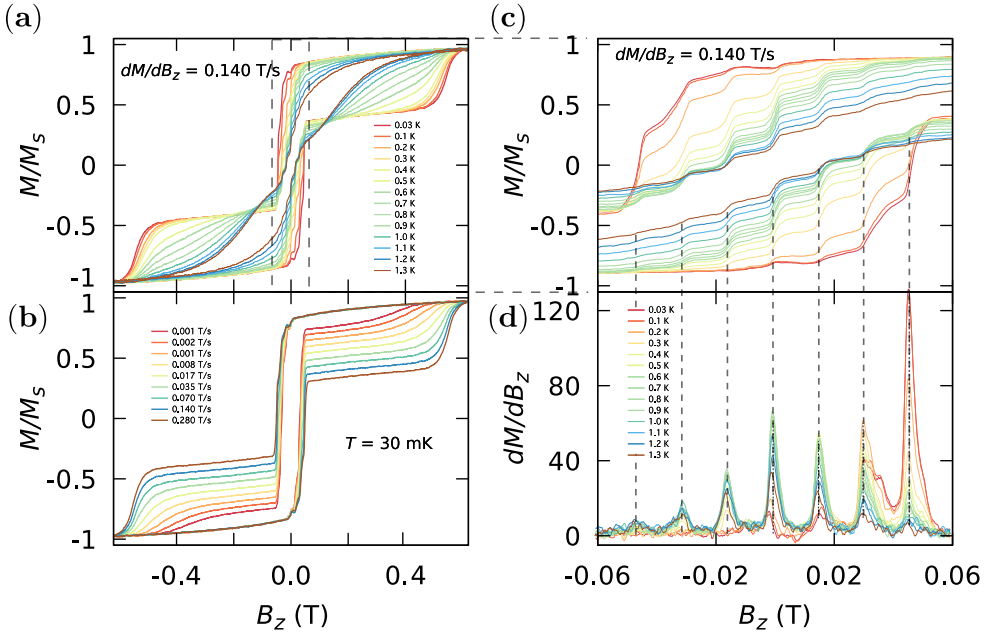


Figure 3.19: **a)** and **c)** Temperature dependence of the hysteresis loops and **d)** its derivative for Tb_2Pc_3 measured with a fixed sweeping rate of 140 mT/s. QTM events are observed in the $B_z \in [-0.05 : 0.05]$ T region as step occurring at ± 14 , ± 34 and ± 47 mT. These transitions correspond to the avoided level crossings that conserve the nuclear spin. The co-tunneling transition rates depend not only on the tunnel splittings of the mixed states but also on the thermal population of the hyperfine levels, thus the steps are strongly temperature dependent. At $B_z = 0.55$ T, an additional broad transitions is observed that corresponds to the transition from the ferromagnetic to the antiferromagnetic alignment of the electronic spins. The hyperfine structure of this step is not experimentally resolved due to the small distributions of the ligand field parameters and the 6° degree misalignment of the two Tb ions. **b)** The sweeping rate dependence of the hysteresis loops at the cryostat temperature of 30 mK. As the dB_z/dt is decreased the adiabatic regime is approached and most of the molecules relax through co-flipping of the electronic spins.

where m^i and n^i take values between $-3/2$ and $3/2$, and describe the nuclear spin components. However, out of these, only the crossings that conserve the nuclear spin are split by $B_4^4 O_4^4$ term while the crossings characterized by $|\Delta m_1| \neq 0$ require a non-axial quadrupolar interaction to be mixed.

μ SQUID measurements

We performed μ SQUID measurements on micrometer sized crystals containing $Tb_2Pc^{Hx8}Pc_2$ molecules that are diluted in an isostructural, diamagnetic matrix

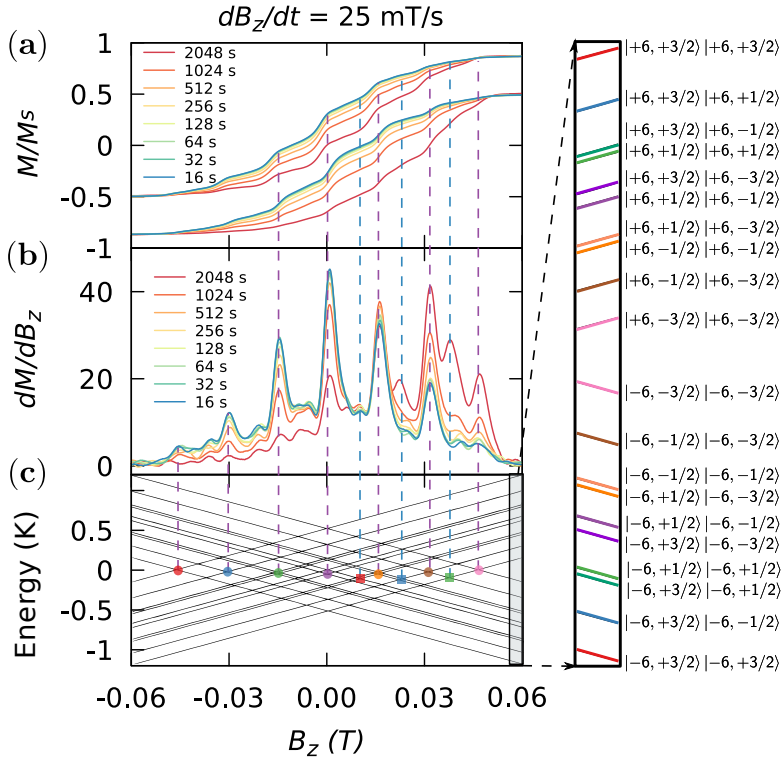


Figure 3.20: a) Magnetization curves ($M(B_z)$) and b) dM/dB_z characterizing a diluted Tb_2Pc_3 crystal at 50 mK as a function of the time the sample is kept in $B_z = -1.3$ T. The nuclear spins were thermalized with the same procedure used to observe the nuclear spin lattice relaxation in $TbPc_2$. That is, we first sweep the field back and fourth in the region where tunneling transitions are observed ($\sim [-0.06, 0.06]$ T), thus the nuclear spins are heated up. We then saturate the sample in a field of -1.3 T and wait for the nuclear spins to relax. The nuclear spins in Tb_2Pc_3 thermalize on a similar scale as in the $TbPc_2$ sibling molecule with a waiting time of the order of thousands of seconds needed to thermally equilibrate the nuclear spin system at 50 mK. Besides the main transitions that conserve the nuclear spins (circles), the transitions that do not conserve the nuclear spins are also observed (squares in Fig. 3.20). Similar to the case of $TbPc_2$ studied in Sect. 3.1 these steps are the result of the non-axial quadrupolar interaction that mixes the states with different nuclear spin states. c) Hyperfine structure of the ground states as a function of the applied longitudinal field obtained after numerical diagonalization of the Hamiltonian given by Eq. (3.34).

formed by $Y_2Pc^{Hx8}Pc_2$ molecules with a concentration of 1%. The sample's dilution controls the dipolar interaction between the molecular spins and consequently is used to reduce the probability of the collective effects. Thus, on one hand, a diluted sample shows a well resolved hyperfine structure and on the other, its dynamics can be understood in terms of the properties of an ensemble of non-interacting molecular spins.

Before each field sweep the nuclear spins were thermalized with the same procedure used to observe the nuclear spin lattice relaxation in $TbPc_2$. That is, we first sweep the field back and fourth in the region where tunneling transitions are observed ($\sim [-0.06, 0.06]$ T), thus the nuclear spins are heated up. We then saturate the sample in a field of -1.3 T and wait for the nuclear spins to reach the equilibrium Boltzmann distribution. The thermalization process at 50 mK is shown in Fig. 3.20a,b. One can see that the nuclear spins in Tb_2Pc_3 thermalize on a similar scale as in the $TbPc_2$ sibling molecule with a waiting time of more than 2000 s at 50 mK needed to thermally equilibrate the nuclear spin system with the phonon bath. This is an expected result as both compounds are characterized by similar hyperfine constants.

Let's look closer to the temperature dependence of the hysteresis loops and its derivative measured with a fast, fixed sweeping rate of 140 mT/s (Fig. 3.19). A fast sweeping rate was chosen in order to highlight the main QTM transitions and simplify the initial interpretation of the measurements.

Starting with a saturated sample, the QTM events are observed first in the $B_z \in [-0.05 : 0.05]$ T field region where a staircase like structure with seven main transitions occurring at ± 14 , ± 34 and ± 47 mT, emerges. These transitions correspond to the avoided level crossings that conserve the nuclear spin. The co-tunneling transition rate depends not only on the tunnel splittings of the mixed states but also on the thermal population of the hyperfine levels. The strong temperature dependence of the QTM state is dictated by the temperature dependence of the equilibrium Boltzmann distribution.

Increasing the magnetic field further, an additional broad transitions is observed at $B_z = 0.55$ T, that corresponds to the transition from the ferromagnetic to the antiferromagnetic alignment of the electronic spins [2]. The hyperfine structure of this step is not experimentally resolved due to the small distributions of the ligand field parameters and 6° degree misalignment of the two Tb ions. It was shown that these transitions cannot be reproduced by employing a purely dipolar coupling between the molecular spins and thus, an exchange coupling between them was introduced.

The sweeping rate dependence of the hysteresis loops at the cryostat temperature of 30 mK is shown in Fig. 3.19b. As the dB_z/dt is decreased the adiabatic regime

is approached. This suggests that the incoherent LZ dynamics in Tb₂Pc₃ is affected by the ferromagnetic interaction of the Tb³⁺ spins. The quantitative analysis of the dynamics through the use of the Lindblad operator formalism is an important outlook of the present section.

Besides the main transitions seen at fast sweeping rates (circles in Fig. 3.20), the transitions that do not conserve the nuclear spins are also observed at small sweeping rates (squares in Fig. 3.20). Similar to the case of TbPc₂ studied in Sect. 3.1 these steps are the result of the non-axial quadrupolar interaction that mixes the states with different nuclear spin states.

4 Hyperfine enhanced phonon assisted tunneling

The advancement towards industrially viable quantum technologies like quantum computing and nanoscale magnetometry depends largely on our ability to control the immediate environment of a system of interacting quantum objects (qubits). The main objective is to preserve coherence during external manipulations and thus exploit intrinsic quantum properties like interference and entanglement. Depending on their nature and coupling strength, most environmental degrees of freedom in interaction with the qubit can be mapped either into a bosonic bath, for non-local, weak interaction, or to a spin bath, in the case of localized, strong interactions [152]. The later case is especially important as it can induce decoherence even in the $T \rightarrow 0$ limit, that is, the dephasing is not accompanied by dissipative processes. Thus, the complex problem of a central quantum system coupled to localized environmental excitations, for example, nuclear spins or paramagnetic centers, is pivotal in mesoscopic quantum physics [153].

Amongst experimental implementations of the above model (*e.g.* NV centers in diamond [143], nanomagnets [154], SQUIDs [155] and impurities in silicon [143]), molecular magnets illustrate especially well the intimate relationship that exists between the manifested quantum phenomenologies (*e.g.* quantum tunneling of magnetization (QTM) [3], spin parity effect [48], Rabi oscillations [61]) and the spin bath. After the experimental evidence of the magnetic bistability in $\text{Mn}_{12}\text{-ac}$ [2], event that marks the birth of the field of molecular magnetism, the breakthrough discoveries of both phonon-assisted and ground state quantum tunneling [3, 5] greatly boosted the interest in these systems. Theoretical inquires to explain the observed dynamics were resolved by carefully considering the effect of the environmental interactions (both spin-phonon and spin-spin couplings) and thus contributed significantly to the development of the theory of the spin bath [156].

Molecular magnets also proved to be ideal systems for testing the predictions made by the constructed theory. Thus, both the influence of the isotopic composition through variation of the hyperfine interaction on the relaxation rate [33] and the

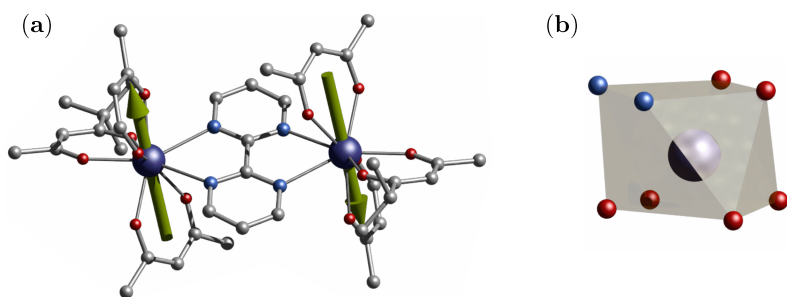


Figure 4.1: **a)** Chemical structure of the $(^{163,164}\text{Dy}(\text{tmhd})_3)_2\text{bpm}$ compounds. **b)** Polyhedral representation of N_2O_6 coordination environment of the Dy ion formed by six oxygen atoms from the tmhd and two nitrogen atoms of the bpm. The coordination geometry around the dysprosium ions can be best described as a square antiprism with a continuous shape measure (CShM) of 0.607 for $^{163}\text{Dy}_2\text{bpm}$ and 0.615 for $^{164}\text{Dy}_2\text{bpm}$. Green arrows represent the anisotropy axis for each Dy(III) obtained from ab initio CASSCF calculations. Colour code: C, grey; N, cyan; O, red; Dy, dark blue.

peculiar square root law for the relaxation at low temperatures and short times were promptly verified [157].

The strong correlations between the dynamics of the spin bath and the relaxation of the molecular spin were also evidenced by measuring directly the nuclear spins through resonant techniques [158]. Both the longitudinal and transverse relaxation times were linked directly to the electronic spin dynamics [159] proving that nuclear spins can serve as microscopic probes for the molecular spin [160]. The theory of the spin bath was also successfully applied in the study of the decoherence in crystals of molecular magnets [75, 70], paving the way for molecular optimization for quantum information processing nanodevices.

Most of the experimental and theoretical investigations into the subject of spin-bath were done using transition metal ion compounds as model systems. However, the last decade saw the rise of molecular complexes that employ lanthanide ions as magnetic centers and at the moment one can make an argument that this class of SMMs are amongst the most promising ones. Unquenched orbital angular momentum, large single ion anisotropy and a strong hyperfine interaction are just some characteristics that distinguish lanthanide complexes in the field of molecular magnetism [13]. For example, in the Chap. 3 was shown that the nature of the strong interaction between the electronic shell of the lanthanide ion and its own nuclear spin has strong repercussions on the tunneling dynamics [135, 148]. Also, the non-zero orbital momentum brings upfront the spin-phonon interaction. Thus, even in the range where the dynamics is temperature independent, the phonon bath can no longer be

ignored. Despite these observations, the quantum dynamics of lanthanide SMMs in the framework of the spin bath theory is a subject largely unexplored.

In Sect. 3.3 we investigated the thermalization of ¹⁵⁹Tb nuclear spin belonging to the archetypical TbPc₂ complex and proven that the relaxation is due to the phonon modulation of the hyperfine interaction. In the current chapter we show that the uncharacteristic, phonon induced hyperfine fluctuations is important in the phonon-assisted tunneling dynamics of lanthanide molecular magnets.

The effect of the nuclear isotopes on the molecular spin relaxation will be studied using two model systems: Dy(tmhd)₃₂bpm and Ho^{III}F₂[15-MC_{Ni}-5]. We show experimentally that the presence of the nuclear spin leads to a significant increase of the relaxation rate at crossover temperatures, that is, when molecular spin tunneling and phonon assisted transitions occur with comparable rates. Then, the characteristics of their relaxation process will be explained by including nuclear spin fluctuations in the theoretical framework of phonon assisted tunneling. We show that thermal fluctuations of the nuclear spin in lanthanide SMMs open additional relaxation channels for the molecular spin and thus leads to an exponential increase of the relaxation time.

4.1 Dy₂dpm isotopologue SMMs

The X-ray single crystal analysis showed that the Dy isotopologue complexes feature two neutral dinuclear systems with formula (^{163,164}Dy(tmhd)₃)₂bpm (denoted by ^{163,164}Dy₂bpm) where tmd = tris(tetramethylheptanedionato) and bpm = bipyrimidine (see Fig. 4.1 and Ref. [4] for the detailed structural and chemical characterization of the compounds). Note that, the two compounds are characterized by different nuclear spin moments with $I(^{163}\text{Dy}) = 7/2$ and $I(^{164}\text{Dy}) = 0$.

Both isostructural complexes, crystallise in the triclinic *P*1 space group, with half-molecule in the asymmetric unit, thus, both dysprosium ions are related by an inversion centre. A single molecule resides in the unit cell. At the metal side, each Dy ion possesses a N₂O₆ coordination geometry formed by six oxygen atoms from the tmhd and two nitrogen atoms of the bpm (Fig. 4.1). The coordination geometry around the dysprosium ions can be best described as a square antiprism with a continuous shape measure (CShM) of 0.607 for ¹⁶³Dy₂bpm and 0.615 for ¹⁶⁴Dy₂bpm.

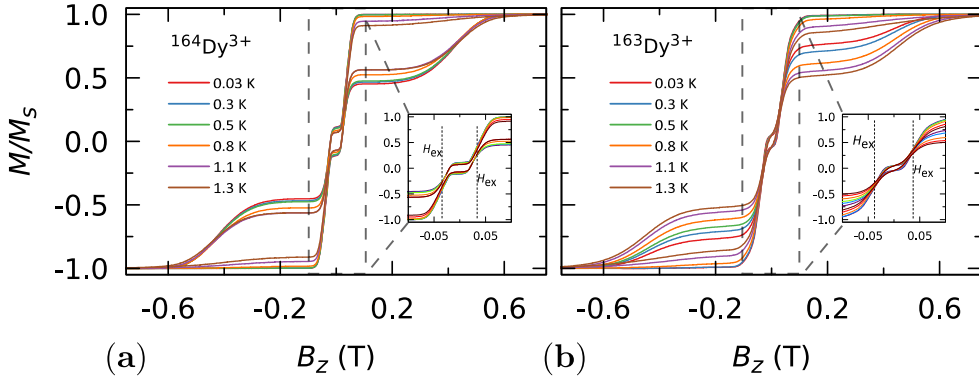


Figure 4.2: Temperature dependence of the magnetic hysteresis loops at a field sweeping rate of 70 mT/s for **a)** $^{164}\text{Dy}_2\text{bpm}$ and **b)** $^{163}\text{Dy}_2\text{bpm}$. The two sharp QTM steps at positive and negative field correspond to ferromagnetic \leftrightarrow antiferromagnetic transitions. At $B_z > 0.3$ T the loops have a broad step due to direct electronic transitions. Also, $M(B_z)$ characteristics of $^{163}\text{Dy}_2\text{bpm}$ a more temperature dependent for $^{164}\text{Dy}_2\text{bpm}$, suggesting a weaker spin-phonon coupling in the isotopically purified compound.

Hysteresis loops

The μSQUID measurements were performed on undiluted single crystals of $^{163,164}\text{Dy}_2\text{bpm}$. Figure 4.2 shows the hysteresis loops of the $^{163,164}\text{Dy}_2\text{bpm}$ measured at different temperatures and a fixed sweeping rate of 70 mT/s. Well-resolved two-steps hysteresis loops were obtained for both compounds with the width of the loops increasing as the temperatures is decreased. The loops are typical of two antiferromagnetically coupled Ising-like spins, that is, around zero field, the loops have a S-shape with two sharp QTM steps at positive and negative fields. For fields larger than 0.3 T the loops display a broad step, which is strongly field-sweep-rate dependent and is a consequence of the direct relaxation process between the antiferromagnetic and ferromagnetic spin states. Additionally, the loops exhibit a small hysteresis at 0 T which comes from the fact that some of the molecules do not tunnel to the antiferromagnetic ground state but remain pinned to the ferromagnetic state. Upon simple comparison of the hysteresis curves of the two compounds it can be observed that the loops for $^{163}\text{Dy}_2\text{bpm}$ show a more temperature dependent behaviour than for $^{164}\text{Dy}_2\text{bpm}$, indicating that the relaxation mechanism is more effective for this system.

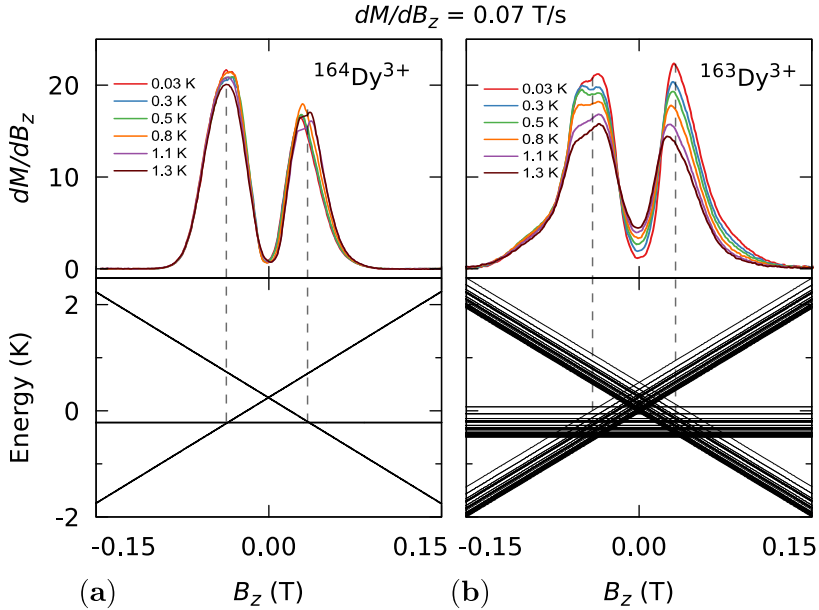


Figure 4.3: Temperature dependence of the derivatives of the magnetic hysteresis loops at a field sweeping rate of 70 mT/s for **a)** $^{164}\text{Dy}_2\text{bpm}$ and **b)** $^{163}\text{Dy}_2\text{bpm}$. The steps are fitted to the ferromagnetic \leftrightarrow antiferromagnetic transitions in the Zeeman diagram.

The mean exchange field (H_{ex}) can be directly extracted from the inflexion points in the hysteresis loops, leading to an effective exchange constant between the Ising spins of the Dy(III) ions:

$$J_e = \frac{g_J \mu_B H_{\text{ex}}}{m_J} \quad (4.1)$$

here $m_J = 15/2$ and $g_J = 4/3$. The determined $J_e = 4.18$ mK is slightly larger than the one obtained from a purely point dipolar approximation ($J_{\text{dip}} = 3.53$ mK for distance of $6.7964(4)$ Å between the two Dy ions). Thus, the interaction between the Dy(III) pairs is mainly of dipolar origin, with a small exchange contribution.

Low-Temperature QTM dynamics

To begin with our analysis, we focus on the low-temperature magnetic properties of the individual $^{164}\text{Dy}_2\text{bpm}$ SMMs as the lack of the nuclear spins simplifies the analysis.

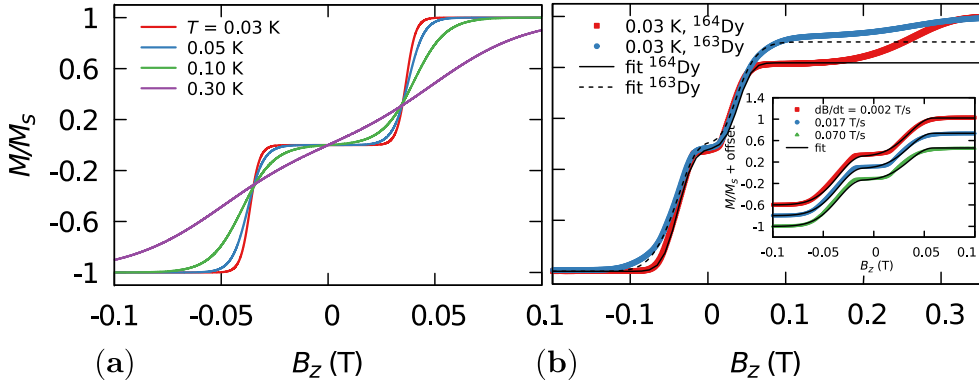


Figure 4.4: **a)** Equilibrium magnetization curves of both Dy_2bpm compounds for different temperatures. At $T = 0.3$ K, $M(B_z)$ are paramagnetic in nature which is not the case experimentally for either of the two compounds. Thus, the relaxation time of the experiment is significantly smaller than the relaxation time of the molecular spins. **b)** Fit of the magnetization curves of $^{164}\text{Dy}_2\text{bpm}$ and $^{163}\text{Dy}_2\text{bpm}$ through the models described in the text with the sole fit parameter being the tunneling probability, $p = 0.74$ for $^{164}\text{Dy}_2\text{bpm}$ and $p = 0.76$ for $^{163}\text{Dy}_2\text{bpm}$ at the anticrossings that conserve the nuclear spin. (inset) Fit of the magnetization curves of $^{164}\text{Dy}_2\text{bpm}$ at different sweeping rates. The curves are shifted upwards for better visibility.

The single ion magnetic properties of the Dy(III) dimers are dominated by the spin-orbit coupling and the interaction with the surrounding ligands, leading to a separation of 188 K between the ground, $m_J = \pm 15/2$ and first excited, $m_J = \pm 13/2$ multiplet. This allows us to describe the complex as two Ising spins $1/2$ coupled through dipolar interaction by a term of the form: $J_{\text{eff}}\sigma_z^1\sigma_z^2$, where $J_{\text{eff}} = J_e m_J^2$ and where $\sigma_z^{1,2}$ are the z-Pauli matrices.

Thus, under the action of an external magnetic field applied along the easy axis, the spin Hamiltonian is written as:

$$^{164}\mathcal{H} = g_{\text{eff}}\mu_B\mu_0 H_z(\sigma_z^1 + \sigma_z^2) + \Delta/2(\sigma_x^1 + \sigma_x^2) + J_{\text{eff}}\sigma_z^1\sigma_z^2$$

where $g_{\text{eff}} = 20$ is an effective g-factor and Δ is the tunnel splitting that arises from the transverse interactions in the system. Figure 4.3 represents the corresponding Zeeman diagram.

With this we can start to understand the hysteresis loop of the $^{164}\text{Dy}_2\text{bpm}$ complex (Fig. 4.2). At $H_z = -1$ T (with Oz chosen along the easy axis of the complex) the sample is polarized and all the spins are in the ground state $|15/2, 15/2\rangle$. As we sweep the magnetic field, the molecules remain in the ground state until the external field compensates the bias field, $B_r \sim -35$ mT, and the SMMs make a transition

from the ferromagnetic to the antiferromagnetic order by quantum tunneling. The position of the relaxation step gives the value of the effective coupling constant, $J_{\text{eff}} = 4.18$ K, as described above. The height of the relaxations step (ΔM) is related to the tunneling probability (p) through the relation: $p = \Delta M / (2M_{\text{in}})$, where M_{in} is the initial magnetization. The next transition happens at $B \sim 35$ mT where the molecules relax non-adiabatically from the state $|15/2, -15/2\rangle$ to $|-15/2, -15/2\rangle$, with the same probability, p . The above discussion is valid only for the idealized situation describing a system of isolated molecules. In a real crystal the molecules are coupled by weak dipolar (and sometimes exchange) interactions and collective effects like the reshuffling of the internal fields have an important influence on the relaxation process. Thus, in order to properly describe the dynamics of the ensemble of SMMs, a multi-body model should be employed. However, in a first approximation, we can assume that the resonance fields of the molecules that tunnel follow a Gaussian distribution around the bias field (B_r):

$$\Delta N \sim \exp\left(\frac{-(B - B_r)^2}{2\sigma^2}\right) \quad (4.2)$$

with the variance of this distribution depending linearly on the sample's magnetization:

$$\sigma(H) = \sigma_0 |M(H)| + \sigma_{\text{min}} \quad (4.3)$$

Using the above assumptions we are able to fit the magnetization curves (Fig. 4.4), with the sole fit parameter being the tunneling probability, p , which for the sweeping rate of 2 mT/s is found to be $p = 0.74$. The parameters σ_0 and σ_{off} that describe the distribution of the resonance fields are chosen so that a simultaneous fit of the magnetization curves under different sweeping rates is obtained.

Now we are ready to consider ¹⁶³Dy₂bpm complex. The ¹⁶³Dy isotope has a nuclear magnetic moment $I = 5/2$ coupled to the electronic shell by the hyperfine ($A_{\text{hyp}}\mathbf{I} \cdot \mathbf{J}$) and quadrupolar interaction ($P_{\text{quad}}I_z^2$). Thus, the total Hamiltonian of the ¹⁶³Dy₂bpm complex can be written as:

$${}^{163}\mathcal{H} = {}^{164}\mathcal{H} + \sum_{i=1}^2 A_{\text{hyp}}\mathbf{I}^i \cdot \mathbf{J}^i + P_{\text{quad}}I_z^i I_z^i \quad (4.4)$$

with $A_{\text{hyp}} = 7.14$ mK and $P_{\text{quad}} = 19.6$ mK. The corresponding Zeeman diagram is shown in Fig. 4.3.

The analysis of the magnetization curve of the ¹⁶³Dy₂bpm complex (Fig. 4.2) is done in a similar fashion to the analysis of the ¹⁶⁴Dy₂bpm complex, with two new assumptions related to the presence of the nuclear spin. We consider that the hyperfine levels corresponding to the ground multiplet $|15/2, 15/2\rangle$ are initially

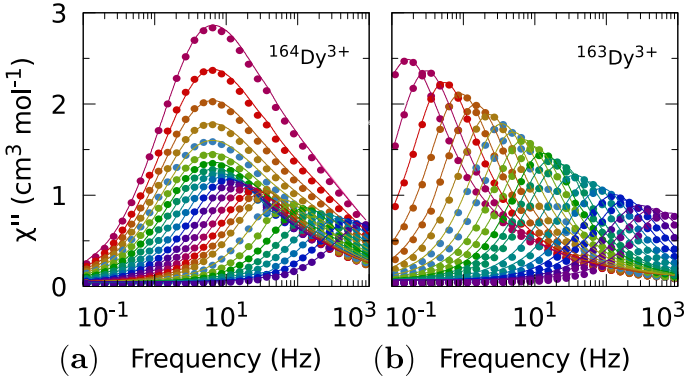


Figure 4.5: The out of phase component of $\chi(\omega; T)$ under a zero DC applied magnetic field ($H_{DC} = 0$ T) for (a) $^{163}\text{Dy}_2\text{bpm}$ and (b) $^{164}\text{Dy}_2\text{bpm}$. For $^{163}\text{Dy}_2\text{bpm}$, at the lowest temperature of 2 K, the maximum is centered around 7 Hz, and stays practically constant until reaching 5 K. Above 5 K the maximum is clearly temperature dependent, shifting swiftly up to 18 K. In contrast, for the $^{164}\text{Dy}_2\text{bpm}$ analogue, at the lowest temperature of 2 K, the maximum lies below our minimum working frequency of 0.1 Hz, while for temperatures between 4 K and 18 K the relaxation shows a strong temperature dependence. The continuous lines are fits of the susceptibility measurements using the generalized Debye model, Eq. 4.5 with the parameter, α , taking values between $0.02 < \alpha < 0.37$ for $^{163}\text{Dy}_2\text{bpm}$, and $0.02 < \alpha < 0.21$ for $^{164}\text{Dy}_2\text{bpm}$.

uniformly populated and tunneling transitions are allowed only between the levels that conserve the nuclear spin, with a fixed probability, p . The resulting fit is shown in Fig. 4.4b, which yields the tunneling probability, $p = 0.76$, for the sweeping rate of 2 mT/s.

We see that the magnitude of the tunneling probability for the two compounds does not change (the small difference may originate in the difference in size and shape of the sample – shape anisotropy). The nuclear spins have the sole role of broadening the relaxation steps. Thus, the magnetic behavior observed at higher temperatures is entirely due to the interaction with the phonon bath.

AC-measurements

In order to get further insight into the role played by the nuclear spins in the relaxation process of the two isotopologues, we turn to alternating current (AC) susceptibility measurements. The reported measurements are performed on polycrystalline samples under an oscillating field of 35 Oe. We investigate both the temperature dependence of the susceptibility under a constant frequency, $\chi(T; \omega)$, and the frequency dependence under a fixed temperature, $\chi(\omega; T)$. The $\chi(T; \omega)$ characteristics

reveals that both compounds exhibit a SMM behaviour. For example, a maximum around 18 K in the out of phase component of the $\chi(T; \omega)$ is observed for both SMMs at the highest frequency available of 1512 Hz. Noticeable differences between the two isotopologues are better seen in the frequency dependence of the susceptibility, thus we will first focus on these measurements.

Fig. 4.5 shows the out of phase component of $\chi(\omega; T)$ under a zero DC applied magnetic field ($B_{DC} = 0$ T) for ¹⁶³Dy₂bpm and ¹⁶⁴Dy₂bpm, respectively. For ¹⁶³Dy₂bpm, at the lowest temperature of 2 K, the maximum is centered around 7 Hz, and stays practically constant until reaching 5 K. Above 5 K the maximum is clearly temperature dependent, shifting swiftly up to 18 K. In contrast, for the ¹⁶⁴Dy₂bpm analogue, at the lowest temperature of 2 K, the maximum lies below our minimum working frequency of 0.1 Hz, while for temperatures between 4 K and 18 K the relaxation shows a strong temperature dependence. In order to compare the characteristic relaxation time of the two compounds at different temperatures we successfully fit the susceptibility measurements using the generalized Debye model:

$$\chi(\omega) = \chi_S + \frac{\chi_T - \chi_S}{1 + (i\omega\tau)^{1-\alpha}} \quad (4.5)$$

where χ_T and χ_S are the isothermal and adiabatic susceptibilities, and τ is the relaxation time. The obtained temperature dependence of the relaxation times is shown in Fig. 4.6 with the parameter α taking values between $0.02 < \alpha < 0.37$ for ¹⁶³Dy₂bpm, and $0.02 < \alpha < 0.21$ for ¹⁶⁴Dy₂bpm. The wide distribution of α and its increase with temperature indicates the presence of multiple relaxation channels that affects the relaxation time (more so for ¹⁶³Dy₂bpm than for the ¹⁶⁴Dy₂bpm complex). The big difference between the relaxation time of ¹⁶³Dy₂bpm and ¹⁶⁴Dy₂bpm at low temperatures ($T < 5$ K) can be understood qualitatively by considering the effect of the nuclear spin on the processes that dominates the relaxation of the electronic spins in this temperature range.

First, for a polycrystalline sample, the presence of nuclear spins increases the fraction of molecules that can relax through quantum tunneling. That is, the relaxation of ¹⁶⁴Dy₂bpm through QTM takes place only when the bias local field satisfies the resonance condition ($B \approx B_r$), while for ¹⁶³Dy₂bpm the hyperfine splitting leads to level anticrossings that are spread in the region $[-75 : 75]$ mT (Fig. 4.3) and thus a larger fraction of molecules are found at resonance at any given time. Second, the hyperfine interaction in ¹⁶³Dy₂bpm results in broader electronic levels and thus in a stronger coupling between the molecular spins and the vibrational acoustic modes. This leads to single phonon processes (direct relaxation) that, in the intermediate temperature range ($2 \text{ K} < T < 5 \text{ K}$), dominates the spin-lattice relaxation dynamics. The stronger spin-phonon coupling for ¹⁶³Dy₂bpm is also observed when comparing the temperature dependence of the hysteresis loops measured with the micro-SQUID

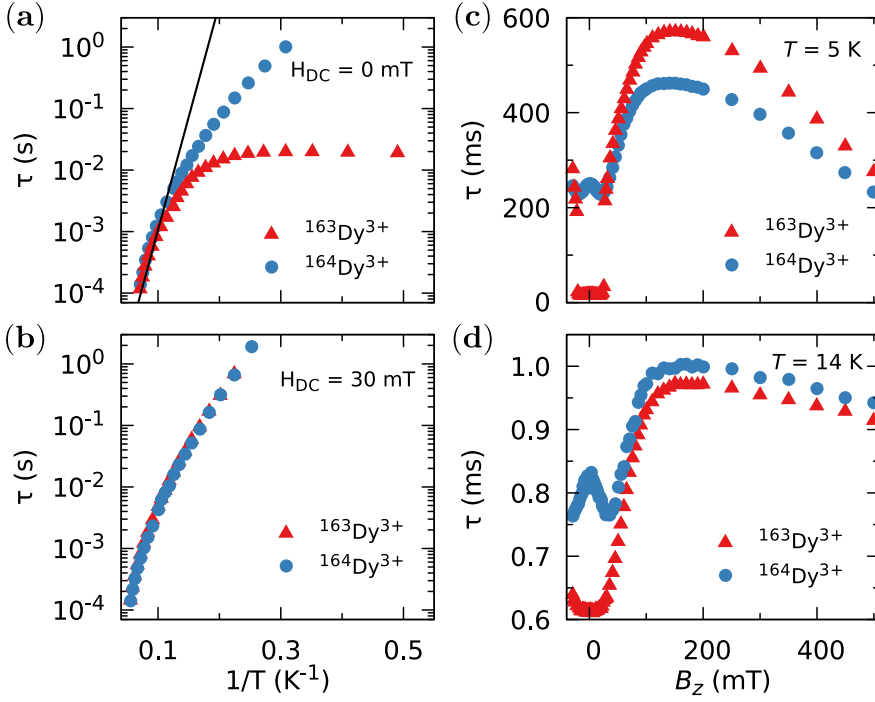


Figure 4.6: Temperature dependence of the relaxation time, τ , for Dy_2bpm isotopologues obtained from the fit of the ac-measurements for **a)** zero applied field $H_{\text{DC}} = 0$ T and **b)** $H_{\text{DC}} = 30$ T. Field dependence of the relaxation time, τ , at a fixed temperature of **c)** $T = 5$ K and **d)** $T = 14$ K. Significant difference in the magnitude of the relaxation times of the two compounds is observed for $T < 5$ K and $H_{\text{DC}} < 25$ T, while at higher temperatures and field the overbarrier Orbach process characterized by an effective energy barrier of $U_{\text{eff}} \approx 81$ (black line) K.

technique (Fig. 4.2). For temperatures larger than 5 K, the relaxation times of the two isotopologues are very similar to each other and are well fitted by the Arrhenius law:

$$\tau = \tau_0 \exp(-U_{\text{eff}}/k_{\text{B}}T) \quad (4.6)$$

The fits shown in Fig. 4.6 lead to similar effective energy barriers: $U_{\text{eff}} = 81.66$ K for $^{163}\text{Dy}_2\text{bpm}$ and $U_{\text{eff}} = 81.04$ K for $^{164}\text{Dy}_2\text{bpm}$.

To investigate further the differences between the dynamic magnetic properties of the two isotopologues, τ was examined in detail by field dependent studies, i.e. $\tau(B)$ at a fixed temperature of 5 K with fields ranging from -30 to 500 mT (Fig. 4.5). We first should notice that the difference in the magnitude of the relaxation times of the two compounds is preserved for fields with amplitude smaller than 25 mT. Also for $^{164}\text{Dy}_2\text{bpm}$, a modulation of $\tau(B)$ with a local maximum at zero and a minimum at

around 30 mT is observed because when applying a small external field we increase the fraction of molecules that are found at resonance and can relax through QTM. The polycrystalline nature of the sample is responsible for shifting the minimum to smaller field value ($B \approx 30$ mT) as compared to the resonance field of about 35 mT observed for a monocrystal. At the same time, no such modulation, is observed for $^{163}\text{Dy}_2\text{bpm}$ because the multiple hyperfine crossings and stronger spin-lattice coupling results in practically uniform relaxation rates. As we increase the field past 25 mT, a significant decrease in the relaxation rate is observed as the molecules are gradually shifted out of resonance and already at 30 mT the relaxation of the two compounds becomes very similar (Fig. 4.6c). At higher fields, $B > 200$ mT, the relaxation is again enhanced due to the direct relaxation process (see also the micro-SQUID measurements in Fig. 4.2).

Interestingly, for fields larger than 100 mT the relaxation of $^{164}\text{Dy}_2\text{bpm}$ is faster than that of $^{163}\text{Dy}_2\text{bpm}$. This is unexpected result and explaining it will require further investigations. However, in order to confirm that this is due to the presence/absence of nuclear spins we measure $\tau(B)$ at 14 K (Fig. 4.6d), where nuclear spin effects are expected to be less important. And indeed we can see that the difference in $\tau(B)$ characteristics of the two isotopologues is greatly reduced. Before we construct a quantitative interpretation of the above observations let's also briefly look at μSQUID and ac-measurements performed on a polynuclear Ho complex.

4.2 Phonon assisted tunneling in $\text{Ho}^{\text{III}}\text{F}_2[15\text{-MC}_{\text{Ni}}\text{-5}]$

Below we report single crystal and powder measurements on $\text{Ho}^{\text{III}}\text{F}_2[15\text{-MC}_{\text{Ni}}\text{-5}]$ (from here on denoted HoNi_5). For details on its chemistry see Ref. [7].

The high level structure of the molecule involves the Ho ion surrounded by the crown of five Ni ions and then coordinated axially by two F ions, resulting in a compressed pentagonal geometry (see Fig. 4.7a). The axial F-Ho-F moiety leads to a large uniaxial anisotropy while the crown-like structure of Ni_5 results in small transverse ligand field interactions and will be shown to play a central role in the dynamics of the compound. The isostructural HoNi_5 molecules form single crystals characterized by the triclinic space group.

Figure 4.7b shows the results of the ab-initio calculations on HoNi_5 using MOLCAS package [7]. The axial F ligation of the Ho ion was found to result in a record splitting of the $J = 8$ ground multiplet with a separation of 577 cm^{-1} between $m_J = \pm 8$ and $m_J = \pm 7$ doublet. The Ni ions are strongly coupled through exchange interactions leading to a singlet ground state, $S = 0$, and a triplet excited state, $S = 1$. The interaction between the Ho ion and Ni_5 crown results in a ground state splitting of about 20 cm^{-1} . The Holmium ion is also the nuclear spin carrier - the ^{165}Ho isotope (100% natural abundance) has a nuclear spin $I = 7/2$. The hyperfine interaction further splits the electronic states with the resulting states characterized by $|m_J, m_S, m_I\rangle$ with $m_J = \pm 8$, $m_S = 0, 1$, and $m_I = -7/2, \dots, 7/2$. Our main interest in this complex comes from the unusual ground state splitting of the Ho ion in interaction with Ni_5 ring that results in a significant temperature range in which the QTM transitions rates are comparable with the spin-phonon transition rates. This leads to rather unique $\tau(T, B)$ characteristics.

μSQUID measurements

We investigate the low temperature magnetic properties of the HoNi_5 complex by performing μSQUID measurements on a monocrystal containing HoNi_5 SMMs diluted in the $\text{Y}^{\text{III}}\text{F}_2[15\text{-MC}_{\text{Ni}}\text{-5}]$ matrix with a concentration of 5%. The effect of different field sweeping rates (dB_z/dt) on the magnetic response ($M(B_z)$) of the sample is measured at temperatures starting from 30 mK up to 4 K.

Figure 4.8 shows the temperature dependence of the hysteresis loops at a fixed sweeping rate of 1 mT/s and 128 mT/s. We first should notice that the molecules exhibit hysteresis up to 4 K bearing evidence of the large uniaxial anisotropy of the molecule. Then, the hyperfine interaction between the Ho electronic shell and its

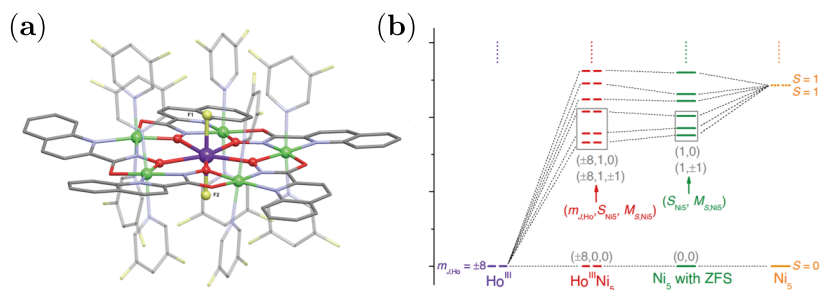


Figure 4.7: **a)** Chemical structure of $\text{Ho}^{\text{III}}\text{F}_2[15\text{-MC}_{\text{Ni}}\text{-5}]$ complex [7]. The molecule presents the Ho ion surrounded by the crown of five Ni ions and then coordinated axially by two F ions, resulting in a compressed pentagonal geometry. The axial F-Ho-F moiety leads to a large uniaxial anisotropy while the crown-like structure of Ni_5 results in small transverse ligand field interactions and will be shown play a central role in the dynamics of the compound. Color code: purple (Ho), green (Ni), grey (C), red (O), light blue (N) **b)** Energy diagram obtained from the ab-initio calculations on HoNi_5 using MOLCAS package [7]. The axial F ligation of the Ho ion was found to result in a record splitting of the $J = 8$ ground multiplet with a separation of 577 cm^{-1} between $m_J = \pm 8$ and $m_J = \pm 7$ doublet. The Ni ions are strongly coupled through exchange interactions leading to a single ground state, $S = 0$, and a triplet excited state, $S = 1$. The interaction between the Ho ion and Ni_5 crown results in a ground state splitting of about 20 cm^{-1} .

own nuclear spin results in a well resolved hyperfine structure that is observed as relaxation steps in the magnetization curve.

At very low temperatures, starting with a saturated sample in a large negative magnetic field and sweeping the zero field we observe that the molecules relax mainly through tunneling transitions between mixed states of hyperfine origin in the ground multiplet. The relaxation rates reflect to some degree both the magnitude of the tunnel splitting and the population of the hyperfine states. As we increase the temperature, phonon assisted processes start to play an important role in the measured dynamics and eventually dominate the relaxation process.

Important features of the relaxation process, central to the following discussion, can be observed in the derivatives of the hysteresis curves measured at different sweeping rate and at a fixed temperature of 3 K (Fig. 4.8c). Equally spaced transitions around zero field seen as sharp peaks in dM/dB_z correspond to the hyperfine crossings that conserve the nuclear spin. The position of the peaks ($\pm 151, \pm 108, \pm 65, \pm 22 \text{ mT}$) and the period of $\Delta B_z = 43 \text{ mT}$ leads to the axial value of the hyperfine constant of $A_{\text{hyp}} = 0.0251 \text{ cm}^{-1}$. Also, the magnitude of the transitions is constant for negative resonance fields and decreases for positive fields. This can be understood by taking into account the direct relaxation which shows larger rates at higher fields.

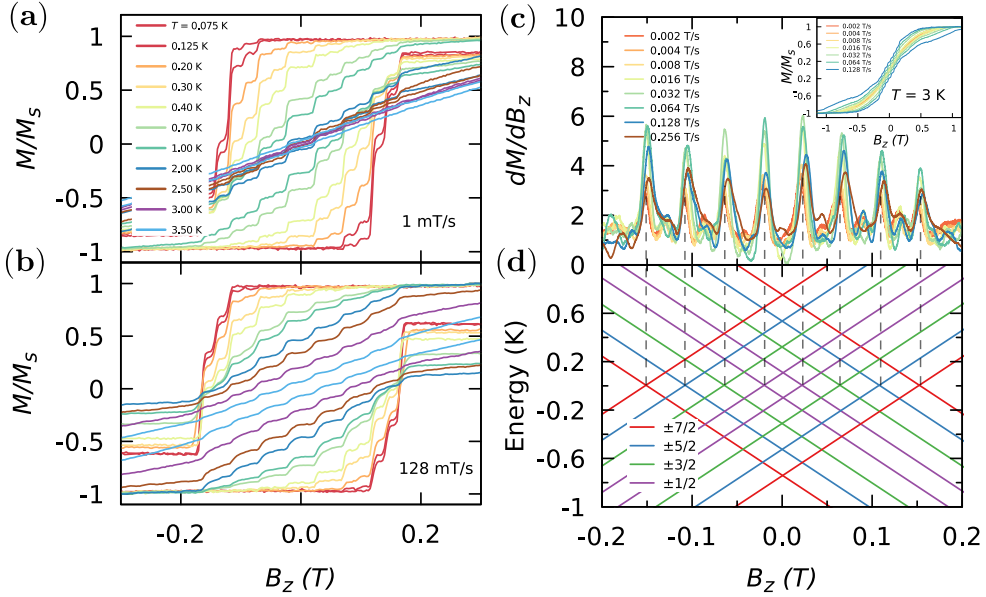


Figure 4.8: Temperature dependence of the hysteresis loops at a fixed sweeping rate of **a)** 1 mT/s and **b)** 128 mT/s. The molecules exhibit hysteresis up to 4 K bearing evidence of the large uniaxial anisotropy of the molecule. The hyperfine interaction between the Ho electronic shell and its own nuclear spin results in a well resolved hyperfine structure that is observed as relaxation steps in the magnetization curve. **c)** The derivatives of the hysteresis curves measured at different sweeping rate and at a fixed temperature of 3 K (the inset shows $M(B_z)$ characteristics). Equally spaced transitions around zero field seen as sharp peaks in dM/dB_z correspond to the hyperfine crossings that conserve the nuclear spin. The position of the peaks ($\pm 151, \pm 108, \pm 65, \pm 22$ mT) and the period of $\Delta B_z = 43$ mT leads to the axial value of the hyperfine constant of $A_{\text{hyp}} = 0.0251 \text{ cm}^{-1}$. The magnitude of the transitions is constant for negative resonance fields and decreases for positive fields due to the direct relaxation which shows larger rates at higher fields. **d)** Hyperfine splitting of the electronic ground state $m_j = \pm 8$.

Direct relaxation process

For illustrative purposes we may consider only two levels ($|\uparrow\rangle$ and $|\downarrow\rangle$) that are split by the Zeeman interaction and the spins are all initialized in $|\downarrow\rangle$ state. Under an negative applied field there is a non-zero chance for the spins to make a direct transition to the state $|\uparrow\rangle$ by absorbing a phonon, a process that can be characterized by the rate $\gamma_{\downarrow\uparrow}$.

Once excited the spins can relax back to the ground state by giving back the phonon ($\gamma_{\uparrow\downarrow}$). At equilibrium, the two transition rates are connected by the Boltzmann factor:

$$\frac{\gamma_{\downarrow\uparrow}}{\gamma_{\uparrow\downarrow}} = \exp\left(-\frac{\Delta E}{k_B T}\right) \quad (4.7)$$

Thus, the excitation process ($\gamma_{\downarrow\uparrow}$) is always less probable than the de-excitation one ($\gamma_{\uparrow\downarrow}$). Especially, when the level splitting is comparable to the cryostat temperature. At positive fields, the $|\downarrow\rangle$ state becomes the excited state and thus $\gamma_{\downarrow\uparrow} > \gamma_{\uparrow\downarrow}$. With the inequality becoming more strong as the field increases. An example of the dynamics described above is seen in many lanthanide SMMs at subkelvin temperatures where besides tunneling around zero field, a broad step at higher fields is observed. To apply the above mechanism to rigorously explain why the derivative of the magnetization curves of HoNi_5 are constant at negative fields and decrease at positive fields is a more complex problem. The levels are split by the hyperfine interaction, thus the dM/dB does not directly reflect the difference between the transition rates as it also depends on the number of spins that can relax.

AC-measurements

Alternating current susceptibility measurement were performed on powder samples of HoNi_5 for temperatures between 4 and 50 K and applied DC fields up to 0.2 T. The Cole-Cole plots at zero field were fitted to the phenomenological Debye model (Fig. 4.9a). The parameter α takes values between 0.18 and 0.36 indicating a narrow distribution of the relaxation time.

The relaxation time obtained from the fit of the ac-measurements at different applied magnetic field and two fixed temperatures, is displayed in Fig. 4.9b. The four minima located at 30, 80, 130 and 170 mT are slightly larger than those observed in μSQUID measurements on single crystals (Fig. 4.8c). The difference is due to the distribution of the axial Zeeman and dipolar interaction of the Ho ion in the powder sample.

Note that, when we analyzed, ac-measurements measurements of $\text{Dy}(\text{tmhd})_3\text{2bpm}$ we saw that the minima in relaxation time moved to lower fields (and not larger) compared to μSQUID on single crystals. The qualitative difference between the two SMMs lies in the antiferromagnetic nature of the ground state of the Dy_2bpm compounds, characterized by $\langle M \rangle = 0$ equilibrium state in zero magnetic field. Thus, at resonance the relaxation of the Dy_2bpm compound leads to a narrower distribution of the local dipolar fields.

The damping of the variation of the relaxation time can be explained by a quadratic rise of the direct relaxation rate with the applied magnetic field, a dynamics similar to what we saw in μSQUID measurements (Fig. 4.8c).

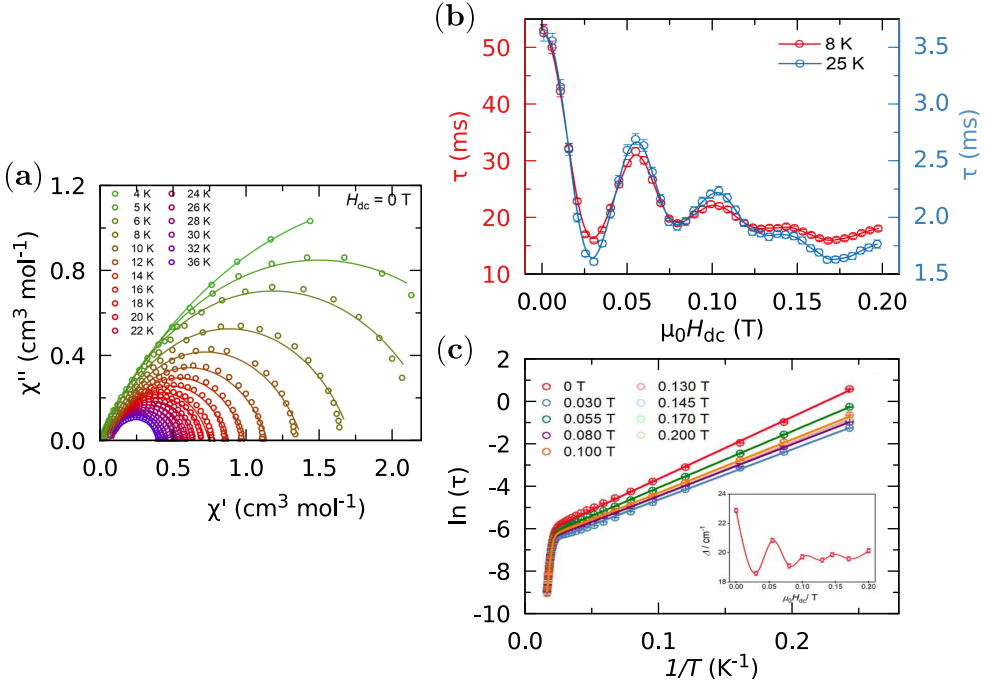


Figure 4.9: AC-susceptibility measurement performed on powder samples of HoNi_5 for temperatures between 4 and 50 K and applied DC fields up to 0.2 T. **a)** The Cole-Cole plots at zero field fitted to the phenomenological Debye model. The parameter α takes values between 0.18 and 0.36 indicating a narrow distribution of the relaxation time. **b)** The relaxation time obtained from the fit of the ac-measurements at different applied magnetic fields and two fixed temperatures. The four minima located at 30, 80, 130 and 170 mT are slightly larger than those observed in μSQUID measurements on single crystals. The difference is due to the distribution of the axial Zeeman and dipolar interaction of the Ho ion in the powder sample. **c)** The relaxation time as a function of temperature at different applied fields. The characteristics show two distinct regions with the crossover temperature being around 37 K. The two branches are fitted to the Arrhenius law with different effective energy barriers (Eq. 4.8). The high temperature regions, at different DC fields, gives a shared $U_{\text{eff}} = 577$ K. In the inset is shown the variation of Δ between 18.6 and 22.9 cm^{-1} as a function of the applied DC field. The effective energy barrier at high temperature is the result of an Overbach activation process while Δ in the low temperature region indicates that phonon-assisted tunneling dominates the relaxation process.

The relaxation time as a function of temperature at different applied fields (Fig. 4.9c) reveals two distinct regions with the crossover temperature being around 37 K. The two branches are fitted to the Arrhenius law with different effective energy barriers:

$$\tau = \tau_{01} \exp(-U_{\text{eff}}/k_{\text{B}}T) + \tau_{02} \exp(-\Delta/k_{\text{B}}T). \quad (4.8)$$

For the high temperature region, we obtain a shared $U_{\text{eff}} = 577$ K, independent of the applied DC field, while for $T < 35$ K, Δ , varies between 18.6 and 22.9 cm^{-1} for $H_{\text{DC}} < 0.2$ T (Inset of Fig. 4.9c).

The effective energy barrier at high temperature is the result of an Overbach activation process while Δ in the low temperature region indicates that phonon-assisted tunneling dominates the relaxation process.

To our knowledge, the U_{eff} of 577 cm^{-1} sets a new record for Ho-SMMs. Note that, ab-initio calculations predicts a reversal barrier of 421 cm^{-1} which is lower than the experimental value. This can be explained through the lack of dynamic correlation effects at the CASSCF level.

4.3 Phonon assisted tunneling in Mn₁₂-ac

We start the analysis of the relaxation processes observed in our study of Dy(tmhd)₃)₂bpm and Ho^{III}F₂[15-MC_{Ni}-5] by first replicating the results obtained by Leuenberger and Loss [163] regarding the phonon assisted tunneling in Mn₁₂-ac and then proceed to construct case studies used to highlight different aspects of the relaxation process. There are a few reasons to take this approach:

- It allows to acquire deep insight into the phonon-assisted tunneling dynamics.
- We can identify which of the observed characteristics of the relaxation process in the two model systems are general characteristics of the phonon-assisted tunneling dynamics and thus are also observed in Mn₁₂-ac and what characteristics are due to the strong hyperfine interaction in Ln SMMs. Note that, in the initial analysis of the Mn₁₂-ac complex, the hyperfine broadening was neglected because for $T > 1$ K the linewidth given by spin-phonon interaction is significantly larger.
- The results reported in Ref. [163] can be used as benchmark for the numerical analysis.

The objective of this section is to build upon the understanding of the phonon-assisted tunneling dynamics in Mn₁₂-ac complex and identify the changes induced by the strong hyperfine interaction in lanthanide compounds.

Spin Hamiltonian

In the ground state, Mn₁₂-ac is characterized by a giant spin $S = 10$ and the following spin Hamiltonian:

$$\mathcal{H}_s = -DS_z^2 - BS_z^4 + B_4(S_+^4 + S_-^4) + g\mu_0\mu_B(H_xS_x + H_zS_z) \quad (4.9)$$

where $D = 0.54$ K, $B = 1.1 \times 10^{-3}$ K, $B_4 = 8.5 \times 10^{-5}$ K. The energy spectrum as a function of an longitudinal applied magnetic field is represented in Fig. 4.10b. Classically, the first term leads to a potential barrier that hinders the relaxation of the electronic spin. Thus, the relaxation process for a system initialized on the right side of the barrier requires an external source of energy to help the spin to overcome the energy barrier. Such an external field is the interaction between the molecular spin and the lattice through spin-phonon interactions. Thus, to describe the spin in interaction with the phonon bath we have to include in the Hamiltonian the terms that describe the lattice degrees of freedom and also the coupling between the molecular spin and the phonon modes.

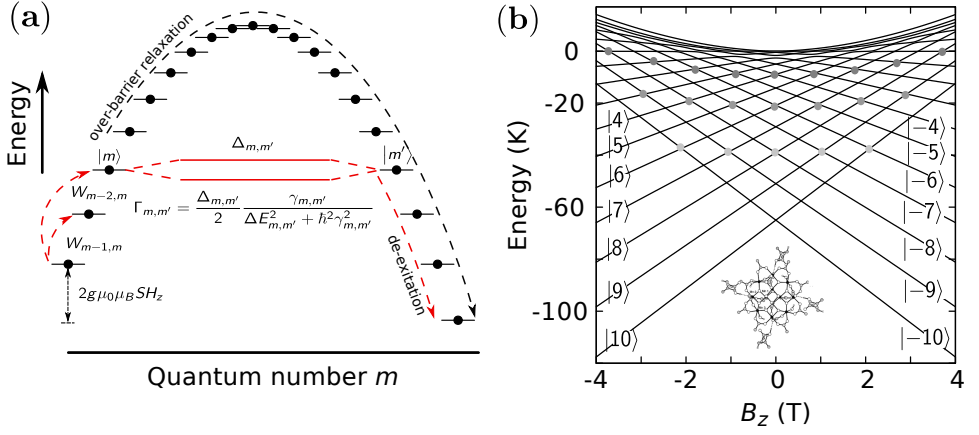


Figure 4.10: Schematic representation of the phonon-assisted tunneling mechanism in Mn_{12-ac} . The molecular spin is found in a potential barrier that hinders its relaxation. Thus, to thermalize, a system initialized on the right side of the barrier requires an external source of energy to help the spin to overcome the energy barrier. Such an external field is the interaction between the molecular spin and the lattice through spin-phonon interactions. The over-barrier relaxation path is indicated by the broken black line while the incoherent tunneling path is shown with the red. The process involves two steps; first the spin is excited to a mixed doublet with the rate $W_{m,n}$ and then tunnels through the barrier. The rate of the phonon-assisted tunneling dynamics is given by: $\Gamma_{m,m'}$. **b)** The energy spectrum as a function of an longitudinal applied magnetic field obtained through the numerical diagonalization of the spin Hamiltonian 4.9.

In the approximation of an harmonic phonon bath, the Hamiltonian describing the lattice modes is written as a function of phonon creation (\hat{b}_α) and annihilation operators (\hat{b}_α^\dagger):

$$\mathcal{H}_{\text{ph}} = \sum_{\alpha} \hbar\omega_{\alpha} (\hat{b}_{\alpha}^{\dagger}\hat{b}_{\alpha} + 1/2) \quad (4.10)$$

where $\hbar\omega_{\alpha}$ is the energy of the α phonon mode. The spin-phonon interaction in the linear approximation can be written as:

$$\mathcal{H}_{\text{s-ph}} = \sum_{\alpha} \left(\frac{\partial \mathcal{H}_{\text{s}}}{\partial \hat{q}_{\alpha}} \right) \hat{q}_{\alpha} \quad (4.11)$$

where $\hat{q}_{\alpha} = 1/\sqrt{2}(\hat{b}_{\alpha} + \hat{b}_{\alpha}^{\dagger})$ is the displacement operator. Thus, the total Hamiltonian is:

$$\mathcal{H} = \mathcal{H}_{\text{s}} + \mathcal{H}_{\text{ph}} + \mathcal{H}_{\text{s-ph}} \quad (4.12)$$

Master equation

The dynamics of the spin-phonon coupled system is described by the master equation for the density matrix operator:

$$\frac{d\rho}{dt} = \frac{i}{\hbar} [\rho, \mathcal{H}] \quad (4.13)$$

which is too complicated to solve exactly because of the large number of degrees of freedom. One common approximation that allows us to separate the spin degree of freedom from the phonon modes is the Markov approximation which works well when the characteristic time of phonon processes is significantly smaller than the spin relaxation time. Thus, the spin evolves under the average field created by the spin-lattice interactions with its dynamics described by the following master equation [163]:

$$\frac{d\rho_{mm'}}{dt} = \frac{i}{\hbar} [\rho, \mathcal{H}]_{mm'} + \delta_{mm'} \sum_n \rho_n W_{nn} - \gamma_{mm'} \rho_{mm'} \quad (4.14)$$

Where

$$W_{m'm} = C_{cf}^2 \frac{\Delta E_{m'm}^3}{\exp(\beta \Delta E_{m'm}) - 1} \quad (4.15)$$

are the spin phonon transition rates computed with the use of Fermi's golden rule, $\gamma_{mm'} = 1/2(W_m + W_{m'})$ and $W_m = \sum_n W_{nm}$. Finally, by projecting the spin Hamiltonian to the subspace generated by $|m\rangle$ and $|m'\rangle$ eigenstates we obtain:

$$\frac{d\rho_m}{dt} = -W_m \rho_m + \sum_n \rho_n W_{m,n} + \Gamma_{mm'} (\rho_{m'} - \rho_m) \quad (4.16)$$

Where

$$\Gamma_{mm'} = \frac{\Delta_{mm'}}{2} \frac{\gamma_{mm'}}{\Delta E_{mm'}^2 + \hbar^2 \gamma_{mm'}^2} \quad (4.17)$$

is the incoherent tunneling rate between the $|m\rangle$ and $|m'\rangle$ states and determined by the tunnel splitting $\Delta_{mm'}$ (Table 4.10a), energy differences $\Delta E_{mm'}$, in the Zeeman diagram (Fig. 4.10b), and the escape rate, $\gamma_{mm'}$.

When the Hamiltonian is diagonal in the S_z basis (the off-diagonal terms, $\sim S_{x,y}$, are set equal to zero) then we recover the master equation that describes an over-the-barrier relaxation process:

$$\frac{d\rho_m}{dt} = -W_m \rho_m + \sum_n \rho_n W_{mn} + \Gamma_{mm'} (\rho_{m'} - \rho_m) \quad (4.18)$$

In the case where the transverse terms in the spin Hamiltonian are considered, Eq. 4.18 holds its ground as long as we are far from level anticrossings.

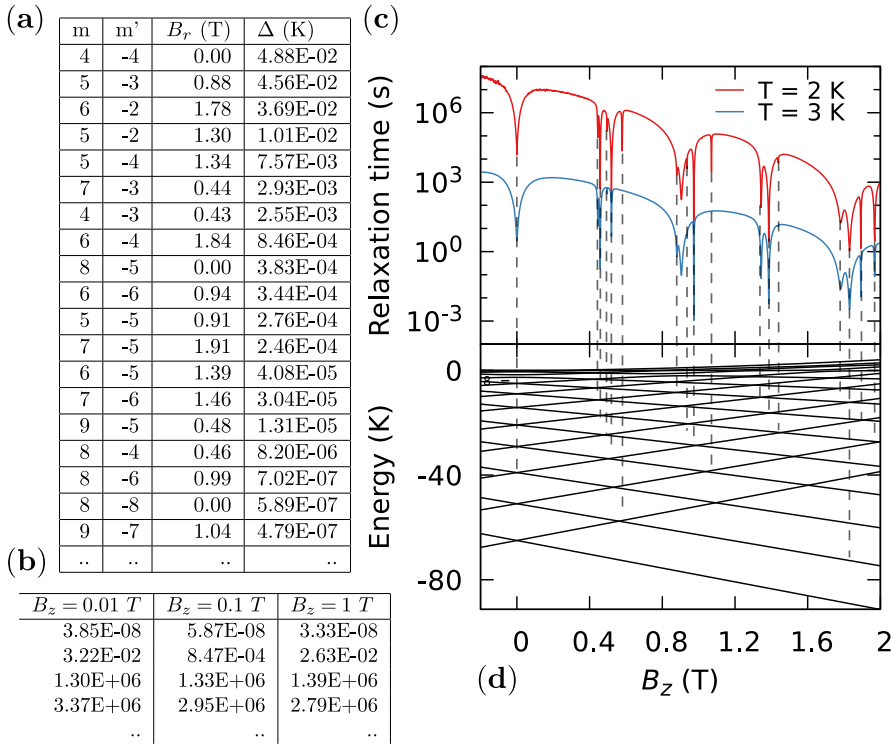


Figure 4.11: **a)** The tunnel splitting between states $|m\rangle$ and $|m'\rangle$ at the resonance field $B_r(T)$ for the low lying anticrossings, computed by using the spin Hamiltonian given by Eq. 4.9. **b)** Smallest relaxation rates at different applied longitudinal fields, obtained after the diagonalization of the transition matrix, \bar{W} . The first mode corresponds to the equilibrium Boltzmann distribution. The expected $w_0 \rightarrow 0$ is not reached because of numerical precision of the diagonalization process. Excluding this mode, the dominant interwell relaxation process is found through the use of the relation: $\tau = \max|1/w_i|$. **c)** Field dependence of the relaxation time for two fixed temperatures. The overall shape of the $\tau(B_z; T)$ characteristics correspond to a over-barrier, thermally activated process. As we increase the field, we lower the energy barrier the spin has to overcome to thermalize and thus a decrease of the relaxation time is observed. The distinct feature of the relaxation curve are the resonant transitions at field values corresponding to avoided level crossings (indicated in the Zeeman diagram **(d)** with the help of the dotted lines).

At resonance, the transverse interactions lead to eigenstates that are a linear superposition of the diabatic states. The overlap between the wavefunctions leads to a non-zero probability for the system to relax through quantum tunneling of magnetization, taken into account through the off-diagonal terms of the density matrix. In this case the relaxation is dominated by phonon assisted tunneling rates

described by the $\Gamma_{mm'}$ rates. The spin is excited to a mixed anticrossing and then tunnels through the energy barrier (see Fig. 4.10a).

In order to find the characteristic relaxation time, we rewrite the master equation in the form:

$$\dot{\rho} = \bar{W}\rho \quad (4.19)$$

where \bar{W} is called the transition matrix. Numerical diagonalization of \bar{W} allows to identify the modes of the relaxation process characterized by the set of real eigenvalues, $\{w_i\}$, and eigenvectors: $\{\{\phi_i^k\}\}$. Thus, the time dependence of the magnetization of the sample is [23]:

$$M(t) = \sum_m m \sum_k \lambda_k \phi_m^{(k)} \exp(-w_k t) \quad (4.20)$$

where m is an eigenvalue of the S_z spin operator and λ_k are constants determined by the initial conditions.

Table 4.11 shows the smallest relaxation rates at $B_z = 0.01, 0.1$ and 1 T, DC applied fields obtained after diagonalization of the transition matrix, \bar{W} . The mode with the smallest rate corresponds to the equilibrium Boltzmann distribution. Note that, the expected $w_0 \rightarrow 0$ is not reached because of the numerical precision of the diagonalization process. Excluding this mode, the dominant interwell relaxation process is found through the use of the relation:

$$\tau = \max\{-1/\text{Real}(w_i)\} \quad (4.21)$$

Relaxation paths

Figure 4.11b shows the field dependence of the relaxation time for two distinct temperatures. The overall shape of the $\tau(B_z; T)$ characteristics correspond to an over-barrier, thermally activated process. As we increase the field, we lower the energy barrier the spin has to overcome to thermalize and thus a decrease of the relaxation time is observed.

Distinct features of the relaxation curve are the resonant transitions at field values corresponding to avoided level crossings (indicated in the Zeeman diagram, Fig. 4.11d, with the help of dotted lines). The main peaks correspond to anticrossings generated purely by transverse ligand field interaction ($\Delta m = 4k$) but transitions originating in the transverse Zeeman interaction can also be observed. The width of the resonance peaks is given by the incoherent QTM rates (Eq. 4.17). At resonance, the relaxation process is dominated by the presence of the higher split excited states. Relaxation through these channels opened by the active spin phonon interactions leads to an increase in the observed relaxation rates.

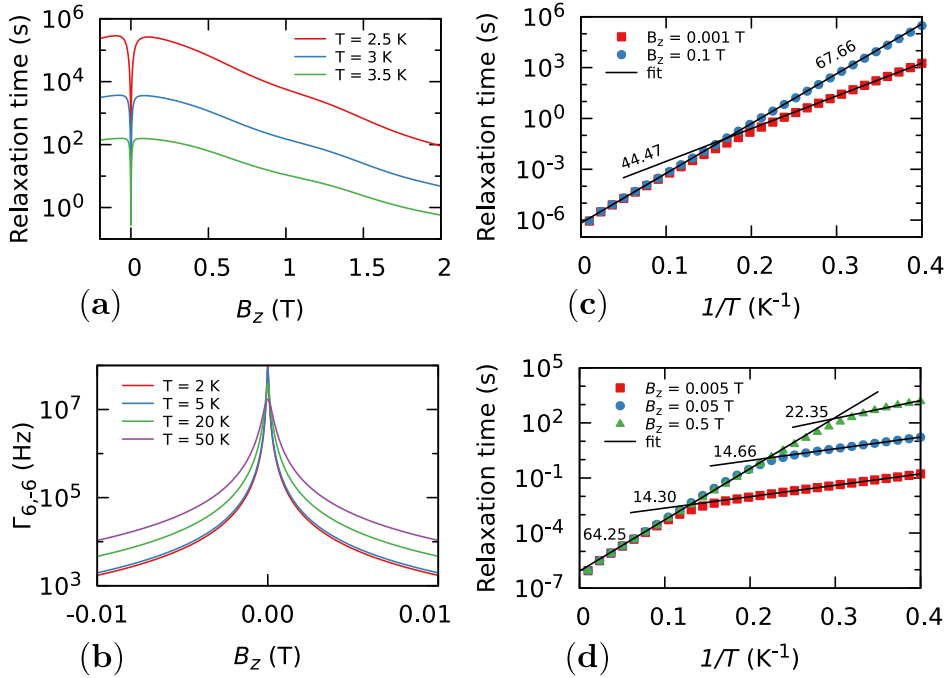


Figure 4.12: **a)** The relaxation time as a function of the applied magnetic field for different temperatures for $\mathcal{H}_T = B_z^6 O_6^6$. The peak in zero field corresponds to the phonon assisted tunneling process. The relaxation path consists of an excitation from ground doublet $|\pm 10\rangle$ to $|\pm 6\rangle$ levels and then tunneling to the other side of the barrier. As the temperature is increased, one can observe an exponential decrease in the relaxation time. **b)** Field dependence of Γ at different fixed temperatures. For temperatures smaller than 5 K, Γ is not changing greatly on the logarithmic scale while the truncation of the peaks by phonon transition rates at high temperatures leads to an effective energy barrier. **c)** The dependence of the relaxation rate on temperature at a fixed field. For $|B_z| < 0.001$ T the two distinct relaxation regions can be fitted by the Arrhenius law: $\tau = \tau_0 \exp(-U_{\text{eff}}/k_B T)$. For the low temperature region one obtains an effective barrier of $U_{\text{eff}} = 44.46$ K which is close to the separation between the ground, $|\pm 10\rangle$, and the split excited states, $|\pm 6\rangle$. For temperatures larger than ~ 5 K, one obtains $U_{\text{eff}} = 67.66$ K which is very close to the value predicted by the axial interactions (~ 65 K), which indicates that the dominant relaxation is an over-barrier mechanism. For $B_z = 0.1$ T the Orbach activation process determines the relaxation for all temperatures. **d)** Temperature dependence of the relaxation time at a fixed applied field for the case: $\Delta_{10,-10} = \Delta_{6,-6} = 10^{-3}$ K. Two distinct temperature regimes, for low temperatures ($T \ll \Delta E_{\pm 10, \pm 6}$) and for high temperatures ($T > \Delta E_{\pm 10, \pm 6}$), are observed. The energy barrier in the low-T region takes values significantly smaller than the separation between the ground and excited doublet resulting from ground state QTM transitions. The inflection point that denotes the transition between the two regions moves to lower temperatures as we move out of the tunnel window.

Study case: $B_6^6 O_6^6$

For most resonant field values there are multiple relaxation paths that contribute to the relaxation process of the magnetic moment. This hinders the further exploration of the phonon assisted tunneling dynamics. As the problem lies in the complexity of the spin Hamiltonian of the Mn_{12} system, we can imagine a simplified, 'fictitious' spin Hamiltonian and compute the relaxation dynamics. Even though, the studies presented below do not correspond to a specific systems there are definite advantages in taking this approach. For example, we can easily single out the effect of different parameters that determine the spin-phonon dynamics.

First, let's assume that the transverse ligand field interaction is determined only by the $B_6^6 O_6^6$ term, which in zero field mixes only the $|\pm 6\rangle$ states. The relaxation time as a function of the applied magnetic field for different temperatures is shown in Fig. 4.12a. The peak in zero field corresponds to the phonon assisted tunneling process. The relaxation path consists of an excitation from ground doublet $|\pm 10\rangle$ to $|\pm 6\rangle$ levels and then a QTM transition to the other side of the barrier. As the temperature is increased, one can observe an exponential decrease in the relaxation time, similar to the case when we consider the full spin Hamiltonian (see Fig. 4.11c). Note that, the incoherent QTM rates, Γ , depends on temperature through the escape rate which in turn depends on the phonon spectrum, and spin-phonon coupling constants.

Figure 4.12b displays the field dependence of Γ at different fixed temperatures. We see that for temperatures smaller than 5 K, Γ is not changing greatly on the logarithmic scale while the truncation of the peaks by phonon transition rates at high temperatures leads to an effective energy barrier. Thus, the temperature dependence of the relaxation time in Fig. 4.12a does not come from the $\Gamma(T)$ dependence but from the increase of the population of the excited $|\pm 6\rangle$ doublet.

The above argument is also supported by the dependence of the relaxation rate on temperature at a fixed field shown in Fig. 4.12c. When we are inside the tunneling window ($|B_z| < 0.1$ T) one can observe two distinct relaxation regions that can be fitted by the Arrhenius law:

$$\tau = \tau_0 \exp(-U_{\text{eff}}/k_B T) \quad (4.22)$$

For the low temperature region one obtains an effective barrier of $U_{\text{eff}} = 44.46$ K which is close to the separation between the ground, $|\pm 10\rangle$, and the split excited states, $|\pm 6\rangle$ (see Fig. 4.11c).

For temperature larger than 5 K, one obtains $U_{\text{eff}} = 67.66$ K which is very close to the value predicted by Eq. 4.9:

$$U = DS^2 + BS^4 = 65 \text{ K} \quad (4.23)$$

which indicates that the dominant relaxation is an over-barrier mechanism. When we choose an applied field that lies outside the tunnel window (e.g., $B_z > 0.1$ T) then the Orbach activation process determines the relaxation for all temperatures (blue circles in Fig. 4.12c).

Next we may ask how the dynamics changes when we add the possibility for the system to relax through the ground state (e.g., $\Delta_{10,-10} = \Delta_{6,-6} = 10^{-3}$ K). This case is of high interest here as it describes an energy spectrum qualitatively close to the HoNi_5 complex. The presence of the ground state relaxation channel increases the relaxation rate and leads to a slightly different dynamics, compared to the previous case. This is best seen in the temperature dependence of the relaxation time at a fixed applied field (Fig. 4.12d). Similar to the case when we had only an excited state splitting we see two distinct temperature regimes, for low temperatures ($T \ll \Delta E_{\pm 10, \pm 6}$) and for high temperatures ($T > \Delta E_{\pm 10, \pm 6}$). However this time, the obtained energy barrier in the low-T region takes values significantly smaller than the separation between the ground and excited doublet showing that tunneling dynamics leads to an effective anisotropy.

Also, the crossover temperature that denotes the transition between the two regions decreases as we move out of the tunnel window. This is dictated by the spread of the incoherent tunneling rates in the field space.

Nuclear spin 1/2

As we observed the general characteristics of the electronic phonon assisted tunneling, we are ready to investigate what would be the effect of a nuclear spin strongly coupled to the molecular spin. The ^{55}Mn ion has a nuclear spin 5/2 which is coupled to the electronic shell through the hyperfine interaction, with $A_{\text{hyp}} \approx 2.4$ mK.

This interaction, however, leads to a broadening of the resonance peak which is much smaller than the level broadening due to phonons. This observation and the fact that the shape of the peaks (Lorentzian and not Gaussian as expected for an inhomogeneous broadening) prompted the Authors in Ref. [163] to neglect the hyperfine splitting.

Our objective is to understand the role played by the nuclear spin in the thermalization process of lanthanide molecular complexes which is characterized by an hyperfine

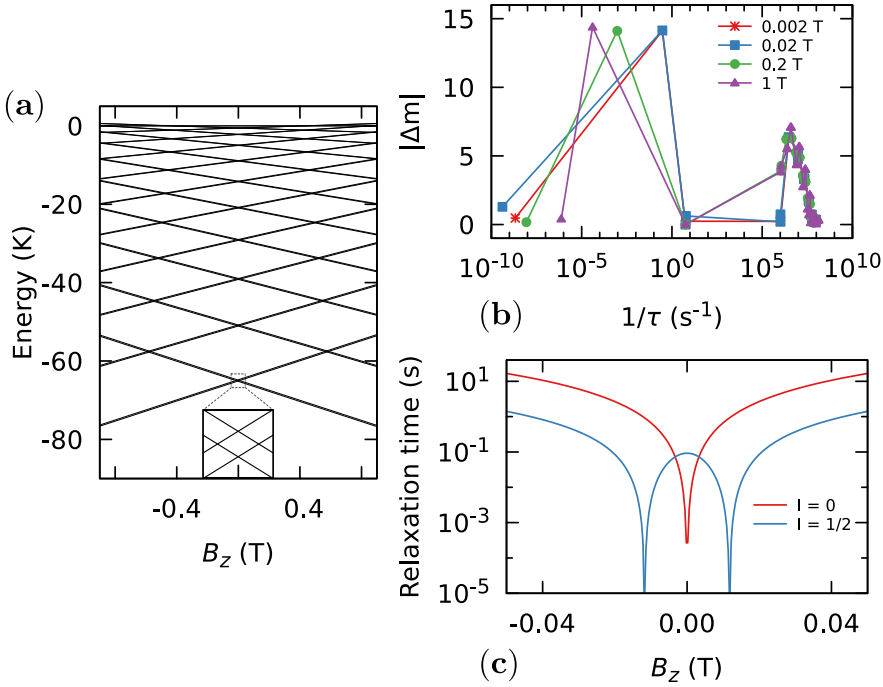


Figure 4.13: **a)** Hyperfine splitting of the energy levels of Mn_{12} by coupling the molecular spin with a nuclear spin, $I = 1/2$ with $A_{\text{hyp}} = 10$ mK. The inset shows a zoom on the hyperfine crossings close to zero field. **b)** The change in the magnetization induced by the modes of the transition matrix, \bar{W} in the $t \rightarrow \infty$ limit. The relaxation time is given by the mode that induces the biggest change on a long timescale. **c)** Relaxation time as a function of the applied field for $I = 0$ and $I = 1/2$ case studies. Nuclear spin fluctuations leads to a significant increase in the relaxation rate.

constant roughly one order of magnitude larger compared to 3d compounds. Thus, we consider a model in which the hyperfine interaction is large enough so that the transitions corresponding to different nuclear spin orientations are well resolved. We will also take $I = 1/2$ which gives a simple enough energy structure to investigate the hyperfine enhanced phonon-assisted tunneling. This, results in a term, $A_{\text{hyp}}(\mathbf{S} \cdot \mathbf{I})$, that is added to the spin Hamiltonian (Eq. 4.9) with $A_{\text{hyp}} = 10$ mK. Because of the smallness of the nuclear spin moment, we neglect, as it is customary, the nuclear Zeeman interaction.

The resulting energy spectrum of the electron-nucleus system is shown in Fig. 4.13a with the inset showing a zoom on the crossings close to zero field. If we neglect the off-diagonal terms then each state is characterized by the electronic and nuclear spin

component, $|m_S, m_I\rangle$. Thus, in general both phonon induced processes and tunneling events will involve the change of both nuclear and electronic spin projection. However, a reasonable approximation is to assume that the processes that dominates the dynamics are the ones that evolve the state of the electronic spin and conserve the nuclear spin or the ones that change the nuclear spin projection but conserves the electronic spin. For the former case, the relaxation rate is given by a relation similar to Eq. 4.15

$$\gamma_{m'_S m_S}^e = W_{m'_S m_S} \delta_{m_I, m'_I} \quad (4.24)$$

where δ is the Kronecker symbol. While the nuclear spin transitions due to spin-phonon interactions are given by (see Sect. 3.3):

$$\gamma_{m_I, m_I-1}^n = \frac{S^2 A_{\text{hyp}}^2 \Delta E_m^3 [I(I+1) - m_I(m_I-1)]}{6\pi\hbar^4 \rho c^5} \frac{\exp(\beta\Delta E_m)}{\exp(\beta\Delta E_m) - 1} \delta_{m_S, m'_S} \quad (4.25)$$

Thus, the transition rates between $|m_S, m_I\rangle$ and $|m'_S, m'_I\rangle$ are given by:

$$W_{m'_S, m'_I}^{m_S, m_I} = \gamma_{m_S, m'_S}^e + \gamma_{m_I, m'_I}^n \quad (4.26)$$

To obtain the characteristic relaxation time we find the eigenvalues of the transition matrix \bar{W} through numerical diagonalization. However, the presence of the hyperfine splitting results in two different time constants for the inter-well dynamics of comparable rates and thus the criterion we used before given by Eq. 4.21 cannot be applied.

To determine which mode dominates the relaxation process we use the eigenvectors of the transition matrix and compute the change in the magnetization induced by each mode in the $t \rightarrow \infty$ limit (see Fig. 4.13b), by using Eq. 4.20.

The computed relaxation time for the case when we don't consider the hyperfine splitting and the case when we do is shown in Fig. 4.13c. It is clearly seen that the hyperfine splitting leads to a significant increase in the relaxation rate. It is expected that a similar process explains the differences between the relaxation of the $^{163,164}\text{Dy}_2\text{bpm}$ isotopologues.

5 μ SQUID-EPR on Gd^{3+} SIMMs

Most Ln^{3+} single ion molecular magnets (SIMMs) are based on ions from the second half of the lanthanide series $n > 7$ due to their large magnetic moment and single ion anisotropy [164]. This is also reflected by the studies presented in this thesis, in Chap. 3 we investigated Tb compounds while in Chap. 4, Dy and Ho complexes were chosen as model systems. On the other hand Gd^{3+} compounds ($n = 7$) are heavily underrepresented with only a few examples reported in literature [165]. This is in striking contrast to the inorganic Gd^{3+} doped crystals that were used extensively in the past to elucidate the puzzle of S-state ion magnetic anisotropy [166].

Together with Eu^{2+} , Mn^{2+} and Fe^{3+} , Gd^{3+} is characterized by the half filled magnetic shell and thus a zero average orbital angular momentum. The theoretical interest in S-state ions was largely based on the desire to understand second order anisotropy inducing effects, that are observable due to $\langle L \rangle = 0$ property of these ions [167]. They were also used as local probes to study phase transition, spin currents in conductors and semiconductors, site symmetries and orientation of the host lattice.

In the above studies, one cannot overstate the importance of EPR technique as it was used to investigate the properties of the ions in a variety of host lattices [14, 166]. The success of the technique also pushed the edge of experimental innovation to the point where we now have a multitude of specialised EPR tools that are used in many branches of physical science [168]. The most common EPR devices operate at a fixed frequency and varying magnetic field. Even though, frequency variation devices were also developed, the use of the zero field method (ZFR) in the study of transition metal ions is scarce [169].

In this chapter we discuss μ SQUID-EPR measurements on diluted crystals of Gd^{3+} containing SIMMs. Besides the main objective of explaining the science behind the measurements, the following sections will also be used to display the power of this particular device to investigate the magnetic properties of molecular magnets.

In what follows we will investigate two variants of Gd^{3+} molecules, $Et_4N[^{160}GdPc_2]$ and $^{157}Gd(tmhd)_3Phen$, that are characterized by similar geometries (both show a distorted D_{4d} geometry) but differ in the nature of the ligated ions (Fig. 5.1 and 5.10). In particular, measurements on $Et_4N[^{160}GdPc_2]$ are used to display the

power of the combined μ SQUID and EPR techniques to rationalize the observed magnetic phenomenology while the investigation of $^{157}Gd(tmhd)_3Phen$ showcases the potential of these measurements to establish magnetostructural correlations. The two Gd^{3+} compounds were chosen as model systems due to their high spin value ($S = 7/2$) with the ligand field splittings in the microwave region that results in a large number of transitions in the $|H| < 1$ T field range.

We start by describing the chemistry of $Et_4N[^{160}GdPc_2]$ and its structural characteristics. Then, we continue with an overview of the theoretical tools used in the analysis with the emphasis on general principles behind spin Hamiltonian parametrization and their connection to the underlying physical processes.

In the experimental investigation of $Et_4N[^{160}GdPc_2]$ we start by presenting the "classical" μ SQUID measurements and expose some of the problems that one encounters when trying to rationalize its dynamics. To improve on these measurements, we introduce the EPR module that allows us to excite the sample with electromagnetic radiation while performing magnetization scans. The results are successfully fit to a set of spin Hamiltonian parameters. The "high resolution" of the obtained spin Hamiltonian is used to explain the magnetic phenomenology of the $Et_4N[^{160}GdPc_2]$ compound.

We finish by a short investigation of the $^{157}Gd(tmhd)_3Phen$ complex where we highlight its potential for magnetostructural analysis.

5.1 $Et_4N[^{160}GdPc_2]$ SIMM

Synthesis and chemical structure

The synthesis procedure, described in Ref. [8], gives diluted crystals of isotopically purified $Et_4N[^{160}GdPc_2](I = 0)$ in $Et_4N[YPc_2]$ with a concentrations of 5%, crystallized in regular block tetragonal red crystals. The X-ray diffraction analysis shows that the $Et_4N[^{160}GdPc_2]$ compound comprises a double-decker motif and crystallizes in the tetragonal $P4/nmm$ space group with one half of the molecule per asymmetric unit while two molecules reside in the entire unit cell. The Gd–N (Fig. 5.1) distances are in the range of 2.4394 – 2.4439 Å. Locally, each Gd^{3+} (III) ion possesses approximate D_{4d} coordination geometry with a continuous shape measure (CSM) of 0.695. The anionic complex is charge-balanced by a tetraethylammonium cation.

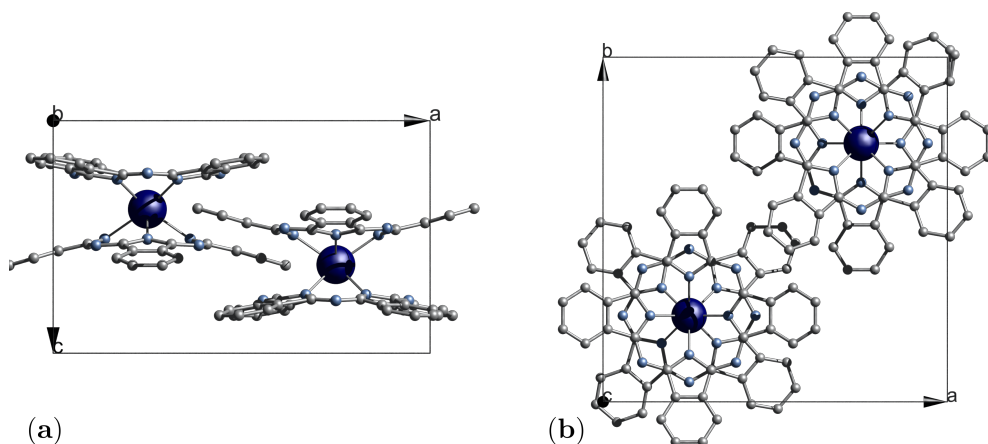


Figure 5.1: a) Side view and b) top view of the unit cell of $\text{Et}_4\text{N}[\text{}^{160}\text{GdPc}_2]$ showing the two molecules that reside in the unit cell. Hydrogen atoms have been removed for clarity. (Colour code: Gd, dark blue; O, red; N, cyan; C, grey).

Spin Hamiltonian

The Gd^{3+} ion at the core of $\text{Et}_4\text{N}[\text{}^{160}\text{GdPc}_2]$ is characterized by the $[\text{Xe}]4f^7$ electronic configuration which in the Russell-Saunders coupling scheme leads to the ${}^8\text{S}_{7/2}$ ground state separated by more than 30 kcm^{-1} from the first excited multiplet ${}^6\text{P}$. Due to the isotropic nature of the ground state, the degeneracy can be removed only by an odd perturbation, for example, the coupling to an external magnetic field through the linear Zeeman term: $\mathcal{H}_Z = g\mu_B \mathbf{B} \cdot \mathbf{S}$ where $g \approx 2$ is the value of the free electron.

The picture described above holds for the pure ${}^8\text{S}_{7/2}$ state while a small admixture with the first excited state ${}^6\text{P}$ gives a ground state that can be written as:

$$\sqrt{(1 - \alpha^2)} {}^8\text{S}_{7/2} + \alpha {}^6\text{P}_{7/2} + .. \quad (5.1)$$

with the corresponding g-value:

$$(1 - \alpha^2)g({}^8\text{S}_{7/2}) + \alpha^2g({}^6\text{P}_{7/2}) + .. \quad (5.2)$$

where $\alpha \sim 10^{-3}$. Thus, the spin orbit admixture in the ground state is responsible for the ligand field splitting effects, around two orders of magnitude smaller than in $\langle L \rangle \neq 0$ lanthanide molecular magnets. For a detailed account of anisotropy inducing interactions in S-state ions see Ref. [167].

The ligand field interaction can be modelled through the use of equivalent Steven's operator formalism (see Sect. 2.3):

$$\mathcal{H}_{\text{lf}} = \sum_{n=1}^3 B_{2n}^0 O_{2n}^0 + B_4^4 O_4^4 + B_6^4 O_6^4 \quad (5.3)$$

where O_q^k are the Steven's operators [14] and B_q^k are the ligand field parameters.

In what follows, we make a few observations regarding the form of \mathcal{H}_{lf} . First, the ligand field Hamiltonian contains only even terms in order to account for time reversal symmetry. Then, the axial terms, $B_{2n}^0 O_{2n}^0$, are invariant with respect to the point symmetry of the Gd^{3+} site (D_{4d}) while the non-axial terms $B_4^4 O_4^4$ and $B_6^4 O_6^4$ are the result of the deviation from the ideal square antiprismatic symmetry of the molecule (distortion of the 45° angle between the two Pc planes). If the symmetry is broken even further, for example through the loss of solvent molecules, as was observed for Mn_{12} -ac, an additional orthorhombic term $B_2^2 O_2^2$ needs to be added to Eq. 5.3. Finally, the choice of the principle axis is not unique: different sets of spin Hamiltonian parameters are related by rotational operations.

The complete Hamiltonian for $\text{Et}_4\text{N}[\text{}^{160}\text{GdPc}_2]$ is now the sum of the Zeeman and ligand field interaction:

$$\mathcal{H} = g\mu_B \mathbf{B} \cdot \mathbf{S} + \sum_{n=1}^3 B_{2n}^0 O_{2n}^0 + \left(B_2^2 O_2^2 + B_4^4 O_4^4 + B_6^4 O_6^4 \right) \quad (5.4)$$

μ SQUID on $\text{Et}_4\text{N}[\text{}^{160}\text{GdPc}_2]$

We start by discussing μ SQUID measurements performed on a micrometer sized monocrystals containing $\text{Et}_4\text{N}[\text{}^{160}\text{GdPc}_2]$ diluted in the isostructural, diamagnetic matrix of $\text{Et}_4\text{N}[\text{YPc}_2]$ with [Gd/Y] ratio of 5%. The crystals are placed on an array of μ SQUIDS and thermalized to sub-kelvin temperatures with the help of a $^3\text{He}/^4\text{He}$ dilution refrigerator. The field can be applied in any direction by using a 3d orthogonal coil system that allows to identify the easy axis of the molecules by using the transverse field method (for more details on the experimental procedure see Chap. 3).

Figure 5.2a shows the temperature dependence of the hysteresis loops measured at fixed field sweeping rate of 128 mT/s. The first observation regards the uniaxial character of the magnetic anisotropy of the molecule. The transition from open hysteresis loop to a superparamagnetic behaviour occurs at the blocking temperature $T_b \sim 0.3$ K. This means that, phonons have sufficient energy to induce overbarrier

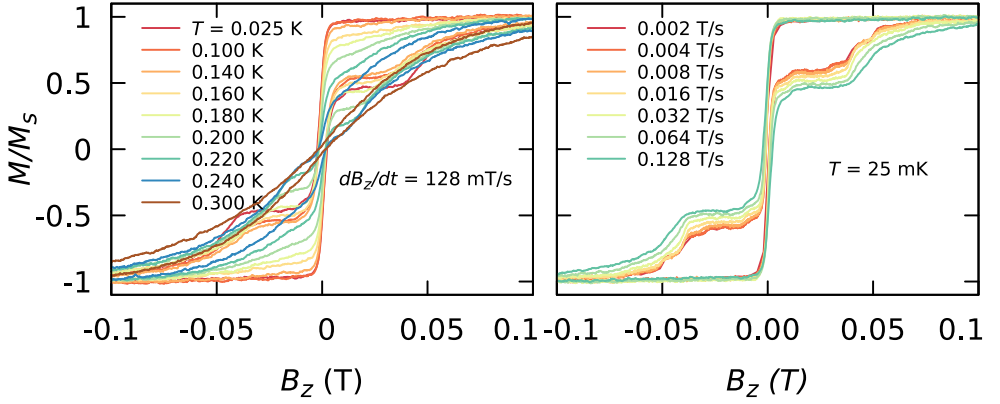


Figure 5.2: (left) Hysteresis loops of the isotopically purified $\text{Et}_4\text{N}[\text{}^{160}\text{GdPc}_2]$ ($I = 0$) in $\text{Et}_4\text{N}[\text{YPc}_2]$ with a concentrations of 5%, measured with μSQUID technique at temperatures between 0.025 and 0.3 K and at a fixed sweeping rate of 128 mT/s and (right) at a fixed temperature of 25 mK and different sweeping rates.

relaxation of the molecular spin and thermalize the sample on a timescale faster than the timescale of the experiment, about 10 s.

An estimation of the axial zero field splitting term from $k_B T_B \approx 3(|B_2^0|S^2 - |B_2^0|/2)$ gives $|B_2^0| = 8.5$ mK, which compares well with what one would expected from the previous discussion on the ligand field splitting of the S-state ions. For example, $|B_2^0| = 6.017$ K for TbPc_2 molecule (see Sect. 5) which is around three orders of magnitude larger than the value estimated for the $\text{Et}_4\text{N}[\text{}^{160}\text{GdPc}_2]$.

Another important feature is the butterfly shape of the hysteresis loops due to quantum tunneling of magnetization in zero magnetic field. Note that, the Gd^{3+} ion is characterized by a ground state with a half integer spin $S = 7/2$. Thus, according to Kramer's theorem (see Sect. 2), the ground state doublet $m = \pm 7/2$ should be degenerate. It is usually assumed that the coupling to environmental spins, both of electronic and nuclear origin, breaks the Kramer's degeneracy and thus makes the relaxation through QTM possible.

To estimate experimentally the magnitude of the tunnel splitting and evaluate the truth value of the above statement, we measure the dependence of the nonadiabatic transitions on the field sweeping rates at a fixed cryostat temperature of 25 mK (Fig.5.2b). For sweeping rates in the range [1..128] mT/s, the zero field relaxation step is practically constant. Which indicates that, under the specified experimental

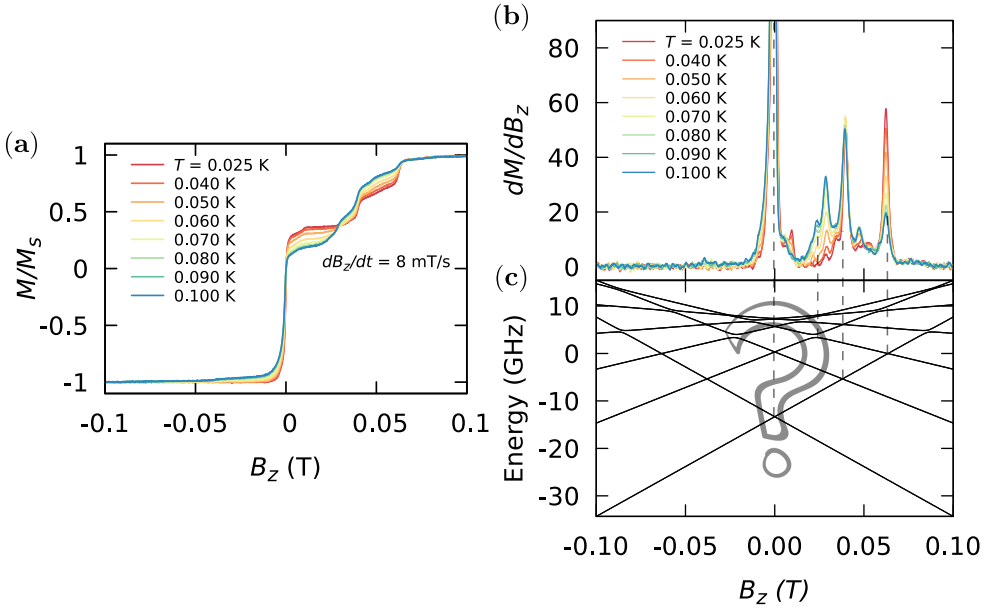


Figure 5.3: **a)** Temperature dependence of the magnetization curves and **b)** their derivatives for $T < 0.1$ K, at a fixed sweeping rate of 8 mT/s. The red dotted lines indicate the relaxation steps present even at the lowest temperature of $T \approx 25$ mK while the black dotted lines mark the steps that appear as T increases. **c)** The Zeeman diagram obtained by diagonalization of the Spin Hamiltonian given by Eq.5.4 with $g = 2$, $B_2^0 = -1.5 \times 10^{-2}$ K, $B_2^2 = 0.5 \times 10^{-2}$ K and $B_4^4 = -1.7 \times 10^{-5}$ K.

conditions, the system is in the adiabatic relaxation regime and larger field sweeping rates are needed to push the system in the Landau-Zener regime.

Another feature that can be observed in Fig.5.2b is the emergence of the fine structure in the magnetization curves at small sweeping rates. In order to investigate the origin of the observed structure, let's look closer at the temperature dependence of the magnetization curves and their derivatives in the temperature range where large variations occur, $T < 0.1$ K, at a fixed sweeping rate of 8 mT/s (Fig.5.3).

A first distinction can be made between steps present even at the lowest temperature of $T \approx 25$ mK, shown with red dotted lines, and the steps that appear as T increases, indicated with black dotted lines. Temperature dependence of these steps suggests that the ones at 0.048 and 0.067 mT depend only on the ground state population while the rest of the transitions are related to the population of the excited states that become occupied with increasing temperature.

In order to fit the spin Hamiltonian given by Eq. 5.4 to the shown fine structure, we may reasonably assume that the steps at 0.048 and 0.067 mT are due to crossings between the ground state $|7/2\rangle$ and first excited states $|-5/2\rangle$ and $|-3/2\rangle$, respectively. While the transitions that are not observed at $T = 25$ mK are due to collective dynamics, and not due to the direct anticrossing with the excited levels because the corresponding steps at negative fields are not observed. Note that, the relaxation in zero field doesn't induce excitations from $|\pm 7/2\rangle$ to $|\pm 5/2\rangle$ (and thus explain the new steps) because ground state quantum tunneling dynamics is a non-dissipative process.

By considering that the anisotropy is dominated by the axial terms (as it is usually the case for uniaxial SMMs) one obtains the following relation between the field value of the level crossings between $|m\rangle$ and $|m'\rangle$ and Stevens coefficients B_2^0 and B_4^0 :

$$H_n = \frac{3nB_2^0}{g\mu_B} \left[1 + \frac{B_4^0}{3B_2^0} ((m-n)^2 + m^2) \right] \quad (5.5)$$

where $n = m + m'$ is the order of the level crossing. And by adjusting the off-diagonal terms $B_2^2O_2^2$ and $B_4^4O_4^4$ we can make the thermally excited steps to correspond to spin-spin cross relaxation processes. The corresponding Zeeman diagram is shown in Fig.5.3c with a satisfactory fit to the measured fine structure. However, the obtained set of fit parameters is not unique as it is based on the assumptions made on the origin of the steps.

In fact, all the steps can originate from collective processes (which is actually suggested by the relative magnitude of the steps at zero/non-zero field) leading to a different set of parameters. Thus, for this particular system, additional information is needed in order to determine the ligand field coefficients. Also, one should point out that, the μ SQUID technique, in most cases, is not sensitive enough to obtain quantitative information on the off-diagonal terms.

To overcome this problems we enhance the μ SQUID technique with an EPR module, that is, we excite the system with microwave pulses while we continue to monitor the magnetization of the sample with the μ SQUID technique.

μ SQUID - EPR measurements on $\text{Et}_4\text{N}[\text{}^{160}\text{GdPc}_2]$

The proof of principle for the use of μ SQUID as a magnetic probe in an EPR experiment was shown in the past when the same setup was used to study resonant photon absorption in $S = 1/2$ systems, Cr_7Ni and V_{15} [64] and to investigate photon-assisted tunneling in Fe_8 [65, 63]. During my PhD I've worked on developing measurement protocols towards a more complete spectroscopic technique.

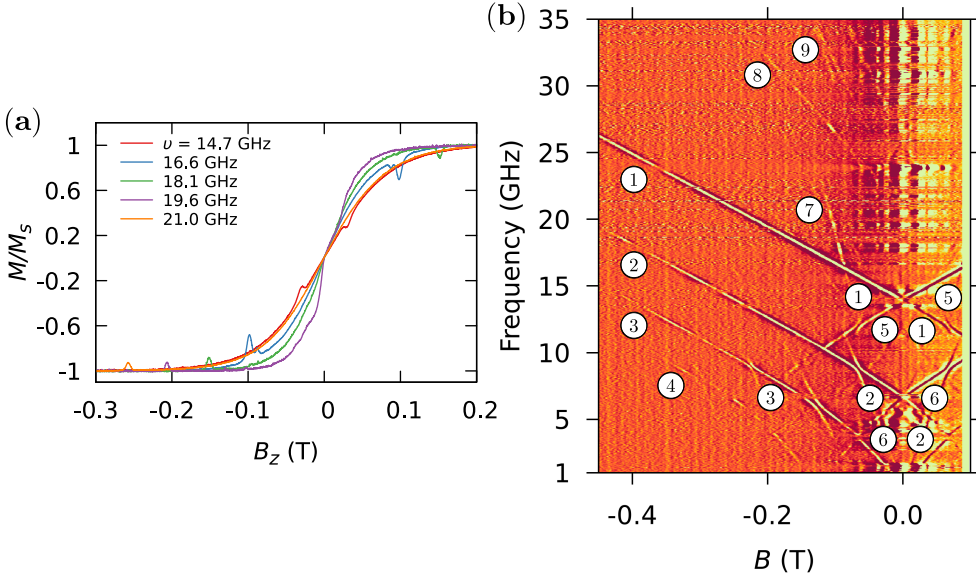


Figure 5.4: **a)** Magnetization curves as a function of the frequency of the RF source obtained while sweeping the magnetic field with a fixed sweeping rate of 8 mT/s and by applying pulses of 40 μ s width and 300 μ s period. **b)** Resonant maps obtained by sweeping the easy axis with a constant sweeping rate of 8 mT/s and applying RF pulses with 40 μ s width every 300 μ s. The labels correspond (m, m') transitions (see the main text).

We used the AnritsuMG369x frequency synthesizer triggered by a pulse generator that allows us to generate EM pulses with a width ranging from nanosecond to continuous radiation with powers up to 20 dBm. The generated signal is transmitted through a coaxial microwave cable which is thermalized between room temperature and 40 mK stage of the cryostat and then applied to the sample through a shortcuted wire suspended above the crystal. Thus, the RF magnetic field is roughly perpendicular to the easy axis of the crystal. The power is adjusted for each frequency to maximize the absorption of the RF signal.

Figure 5.4a shows magnetization curves as a function of frequency obtained while sweeping the magnetic field with a fixed sweeping rate of 8 mT/s and by applying RF pulses of 40 μ s width and a period of 300 μ s in between μ SQUID measurements. One can observe the resonant transitions as absorption dips in the magnetization curve, following the resonant condition: $h\nu = |E(m) - E(m')|$.

By applying a Gaussian filter to extract the absorption peaks and by plotting the set of measurements for $B \in [-0.5 : 0.1]$ T and $\nu \in [1 : 35]$ GHz as a color map where

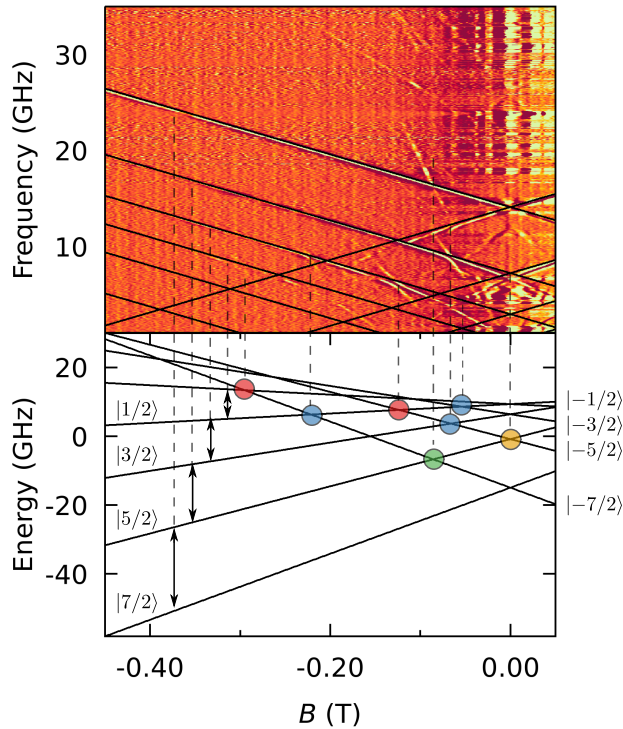


Figure 5.5: **a)** Linear fit of the resonance map by using: $g = 1.96$, $B_2^0 = -6.83 \times 10^{-1}$ GHz, $B_4^0 = -1.5 \times 10^{-3}$ GHz, $B_6^0 = 1.6 \times 10^{-8}$ GHz obtained from Eq. 5.7. $(m, m \pm 1)$ dipolar transitions are shown as black lines superimposed on the resonance map. **b)** Zeeman diagram with marked level anticrossing, according to the selection rules: $\Delta m = 4$ (blue), $\Delta m = 6$ (green), $\Delta m = 5$ (yellow) and $\Delta m = 3$ (red).

the color stands for the magnitude of the peak, we get Fig.5.4b. In what follows we will build first a qualitative understanding of the main feature seen in Fig.5.4b and then describe the fitting procedure based on a least square non-linear algorithm.

The resonance map is typical of a SMM with pseudo uniaxial magnetic anisotropy (i.e., an approximate linear dependence of the transition lines on the axial applied magnetic field) confirming the results of the structural analysis and previously presented μ SQUID measurements. This allows us to label different transitions by (m, m') where m are m' designates the eigenvalues of S_z operator: $S_z |m\rangle = m |m\rangle$. This notation works well for the transitions in high longitudinal magnetic fields and for large $|m + m'|$ values where the axial approximation holds.

The transition lines can be grouped in sets characterized by similar absolute value of the slope. Each group corresponds to transitions with different selection rule. Most of the transition lines are part of the set with the smallest absolute value of the slope (denoted by, ①, ②, ③, ..., in Fig.5.4) and correspond to 'allowed' dipolar transitions characterized by the selection rule $\Delta m = \pm 1$.

Amongst these transitions, the magnitude of the zero field splitting obtained from μ SQUID measurements, the linearity and the relative intensity of different lines, indicate that ① corresponds to the $(7/2, 5/2)$ transition. Thus, the subsequent lines results from $(5/2, 3/2)$, $(3/2, 1/2)$.., transitions. Also, ⑦, ⑧, and ⑨ designate higher order transitions allowed by the non-axial interactions. Additional features in the resonance map that indicate to the interactions that break the axial symmetry are the deviation from linearity at small fields, $|B| < 0.2$ T, and the direct observation of level anticrossing, marked with circles in Fig.5.5. With the above considerations in mind we can start the quantitative analysis.

Using the uniaxial nature of the system, we evaluate the magnitude of the g-value by fitting the linear (high field region) part of the spectrum and obtain:

$$g = \frac{h}{\mu_B} \frac{d\nu}{dB} = 1.96(1) \quad (5.6)$$

The main contributions to g-value for S-state ions, that are discussed in literature, are as follows:

- quantum electrodynamical value for a free electron: 2.0023
- mixing of 6P excited state in the ground state $^8S_{7/2}$: -0.0078
- Judd and Lindgren relativistic contributions: -0.0017

The final theoretical value of $g = 1.992(8)$ was confirmed by numerous experiments on Gd^{3+} doped in inorganic lattices.

The experimental value that we obtain, $g = 1.9(6)$ differs significantly from this theoretical prediction. However, before one tries to look seriously into this discrepancy, for example, by taking into consideration higher order Zeeman terms, the accurate calibration of the 3d-axes coil system should be performed because we estimate that the current experimental precision is not far of 2%.

Axial Ligand Field Interaction

We will now proceed with an initial evaluation of the diagonal ligand field terms by assuming an axial approximation. Extrapolating the linear high field region of the $(7/2, 5/2)$, $(5/2, 3/2)$, $(3/2, 1/2)$ transitions to zero field one gets the zero field resonant (ZFR) splittings, that we denote by: ν_{01} , ν_{02} and ν_{03} . And by using

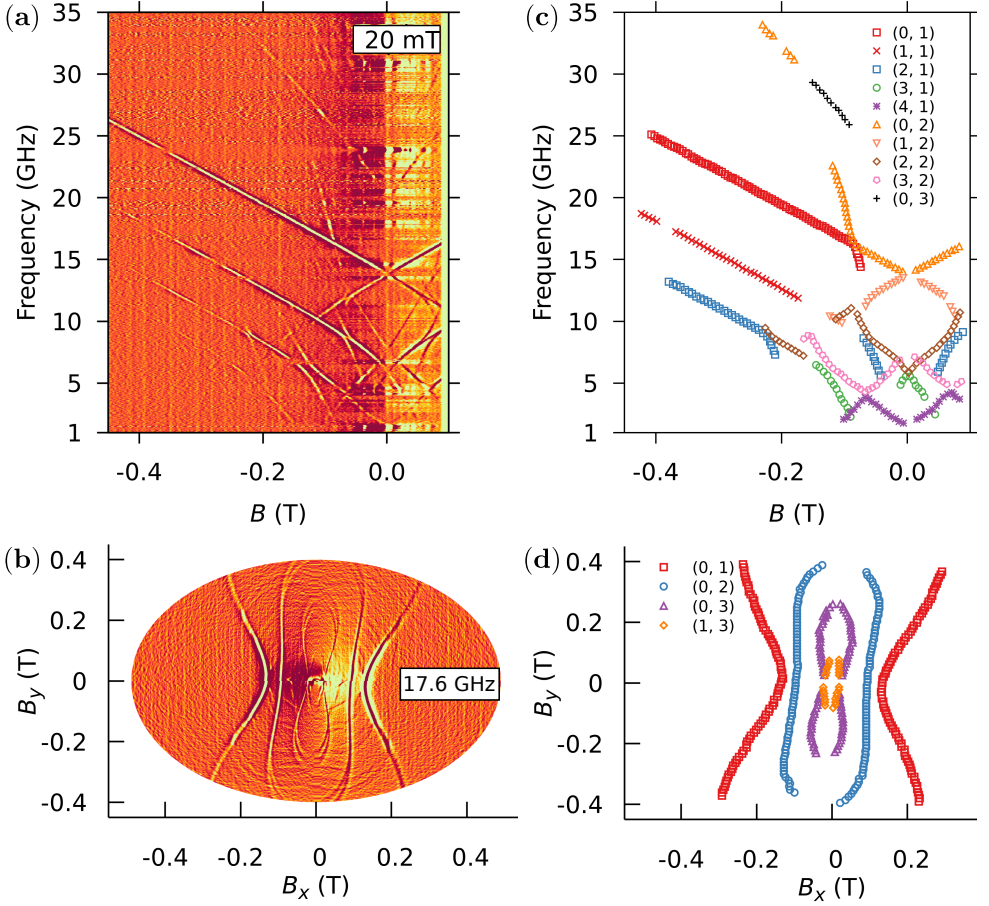


Figure 5.6: **a)** The resonance map when the field was swept along the easy axis with an additional, constant transverse field of 20 mT. **b)** The resonant map while sweeping different directions in the (easy-hard) plane at a constant frequency of 17.6 GHz. **c)** and **d)** shows the sampling of the resonance maps. $(k, \Delta m)$ denotes an individual transition with k being the order of the eigenvalue and Δm the corresponding selection rule.

the algebraic form of three axial O_{2n}^0 Steven operators, one obtains the following relations between ZFR values and the Steven's coefficients:

$$\begin{aligned}
 hv_{01} &= |-6B_2^0 + 720B_4^0 - 17640B_6^0| \\
 hv_{02} &= |-12B_2^0 + 600B_4^0 + 17640B_6^0| \\
 hv_{03} &= |-18B_2^0 + 1200B_4^0 - 7560B_6^0|
 \end{aligned} \tag{5.7}$$

which allows to solve exactly for B_{2n}^0 .

The eigenvalues of the axial Hamiltonian as a function of the applied magnetic field is shown in Fig.5.5 and the respective $(m, m \pm 1)$ dipolar transitions are shown as black lines superimposed on the resonance map. The observed, reasonably good agreement with the experimental points indicates that the hypothetical axial symmetry is a good approximation for $Et_4N[^{160}GdPc_2]$ and confirms the indexation of different transition lines. Also, we can now identify the observed higher order transitions in Fig.5.4. For example, (7) corresponds to the transition $(7/2, -7/2)$ and (8), (9), are $(7/2, 3/2)$ and $(7/2, 1/2)$, respectively.

Transverse interactions

When considering the off-diagonal interactions in Eq. 5.4 the eigenvectors of \mathcal{H} are no longer the eigenvector of S_z but instead they should be written as a linear combination of the $|m\rangle$ states. The exact analytical solution to the eigenvalue-eigenvector problem of a generalized spin Hamiltonian is often hard to find and a perturbative approach is preferred.

Two states, $|m\rangle$ and $|m'\rangle$ mixed by the transverse term of order k , BS_{\pm}^k , results in the following expression for the tunnel splitting:

$$\Delta_m^{m'} \sim B_2^0 S^2 [BS^k / (2B_2^0 S^2)]^{(m'-m)/k} \quad (5.8)$$

Note the spin parity effect, that is, the mixing between levels $|m\rangle$ and $|m'\rangle$ is possible only if the difference $|m - m'|$ is a multiple k . Thus, the admixing of different states is mostly significant for levels at the top of the barrier (small absolute value of m) and at level crossings where the axial and transverse interactions are comparable in magnitude. This makes the repelling regions in the parallel Zeeman pattern a central features for exploring non-axial interactions (see Table A.3 for the relation between the repelling points and the point symmetry of the ion).

In Fig.5.5 we indicate the anticrossings with circles in the Zeeman diagram. Note that, two repelling regions in the transition map correspond to the same anticrossing in the Zeeman diagram. The selection rule involved in the mixing of the energy levels is shown in the following color code: *blue* – $\Delta m = 4$, *green* – $\Delta m = 6$, *yellow* – $\Delta m = 5$ and *red* – $\Delta m = 3$.

It has been shown in the past that deviations from the ideal D_{4d} symmetry through an distortion angle between the Pc planes leads to $B_4^4 O_4^4$ and $B_6^4 O_6^4$ terms in the spin Hamiltonian. Thus, the expected anticrossings are the ones characterized by: $\Delta m = 4$ selection rule.

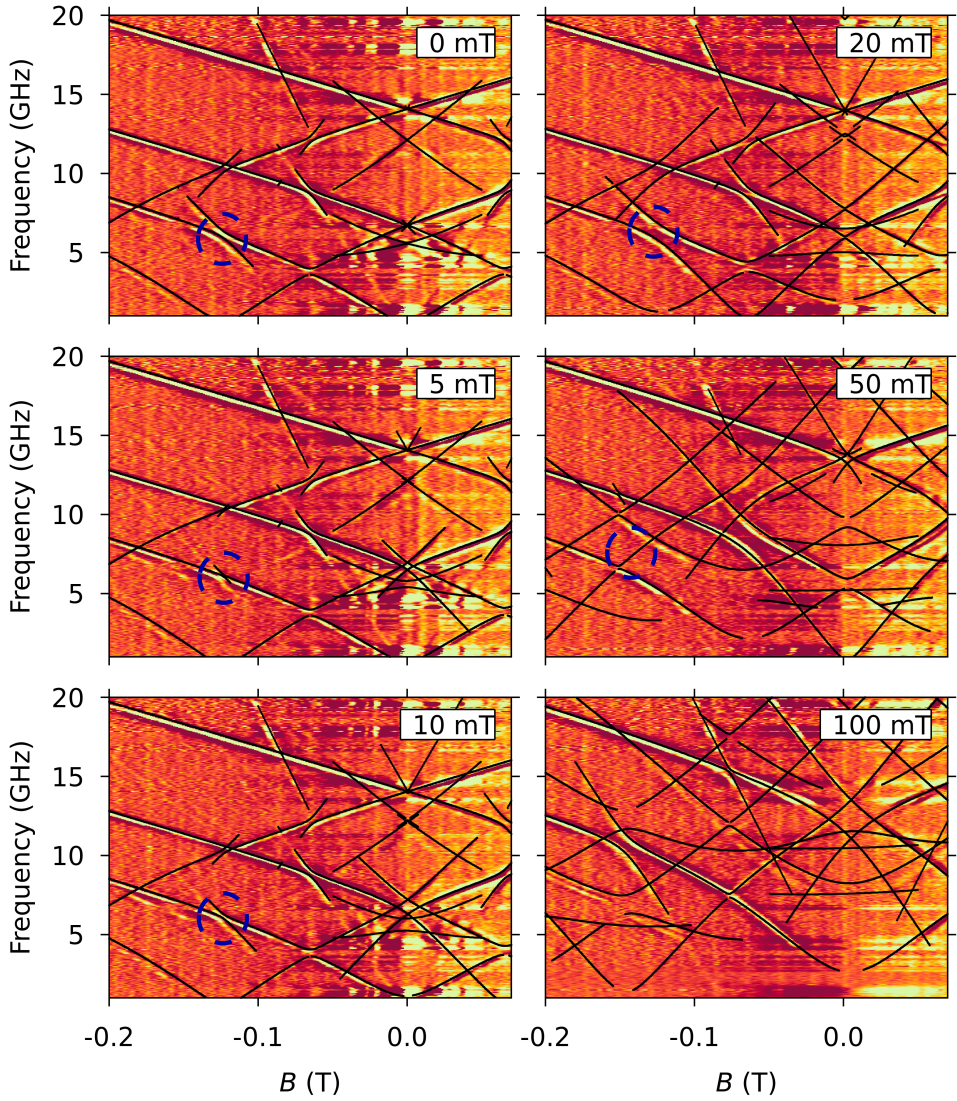


Figure 5.7: Fit of the transverse field maps with $g = 1.96$, $\phi = 3^\circ$, $B_2^0 = -6.80 \times 10^{-1}$ GHz, $B_4^0 = -1.57 \times 10^{-3}$ GHz, $B_6^0 = 1.6 \times 10^{-7}$ GHz, $B_2^2 = -2.75 \times 10^{-1}$ GHz and $B_4^4 = 3.38 \times 10^{-3}$ GHz. The fit lines were shifted upwards by 20 MHz to better visualize the experimental transitions. Blue circle indicates the oscillations of $\Delta_{-5/2}^{1/2}$ as a function of the applied transverse field bearing evidence to the phase interference effect.

The tunnel splitting, Δ , is the result of the linear combination of O_4^4 and O_6^4 interactions, without direct means to distinguish between them. For this reason in the following discussion $B_4^4O_4^4$ is the only term that will be considered but one should remember that it incorporates the $B_6^4O_6^4$ component.

All the other observed tunneling gaps cannot be explained by the direct application of $B_4^4O_4^4$ and a combination of odd and even transverse interactions has to be employed. For example, mixing of $|5/2\rangle$ and $|-5/2\rangle$ states with $\Delta m = 5$ is possible only if one includes an environmental magnetic field. While the anticrossings with $\Delta m = 3$ or 6 indicate to the orthorhombic interaction $B_2^2O_2^2$. As mentioned, when studying the dynamics at low T of the Mn_{12} -ac molecule, the O_2^2 term was found to originate in the loss of solvent molecules.

Control over the non-axial interactions

One big advantage of our technique is the control over the non-axial spin Hamiltonian through the application of a transverse magnetic field. Thus, two measurements will be discussed in the following:

- keep the direction of the applied field fixed and vary the frequency at different constant applied transverse field.
- fix the frequency and vary the direction of the applied magnetic field.

Fig.5.6a shows the resonance map where the field was swept along the easy axis with an additional, constant transverse field of 20 mT, applied. The effect of the transverse field is directly observed as an increase in the magnitude of the tunnel splittings.

Fig.5.6b shows the resonant map while sweeping different directions in the (easy-hard) plane at a constant frequency of 17.6 GHz. The angular dependence allows to determine the sign of the off-diagonal terms as the tunnel splittings gives access only to the magnitude of the ligand field coefficients.

Fitting procedure

We are now in position to discuss the fitting procedure to obtain the complete spin Hamiltonian. First, we have to reconsider the labeling system because as we increase the transverse field, a significant level mixing of the states occurs and (m, m') does not identify the transitions anymore. Thus, we relabel the observed transitions by using the order of the eigenvalue and the corresponding selection rule: $(k, \Delta m)$. Figures 5.6c,d, show the sampling of the resonance maps with the emphasis on the new labeling system.

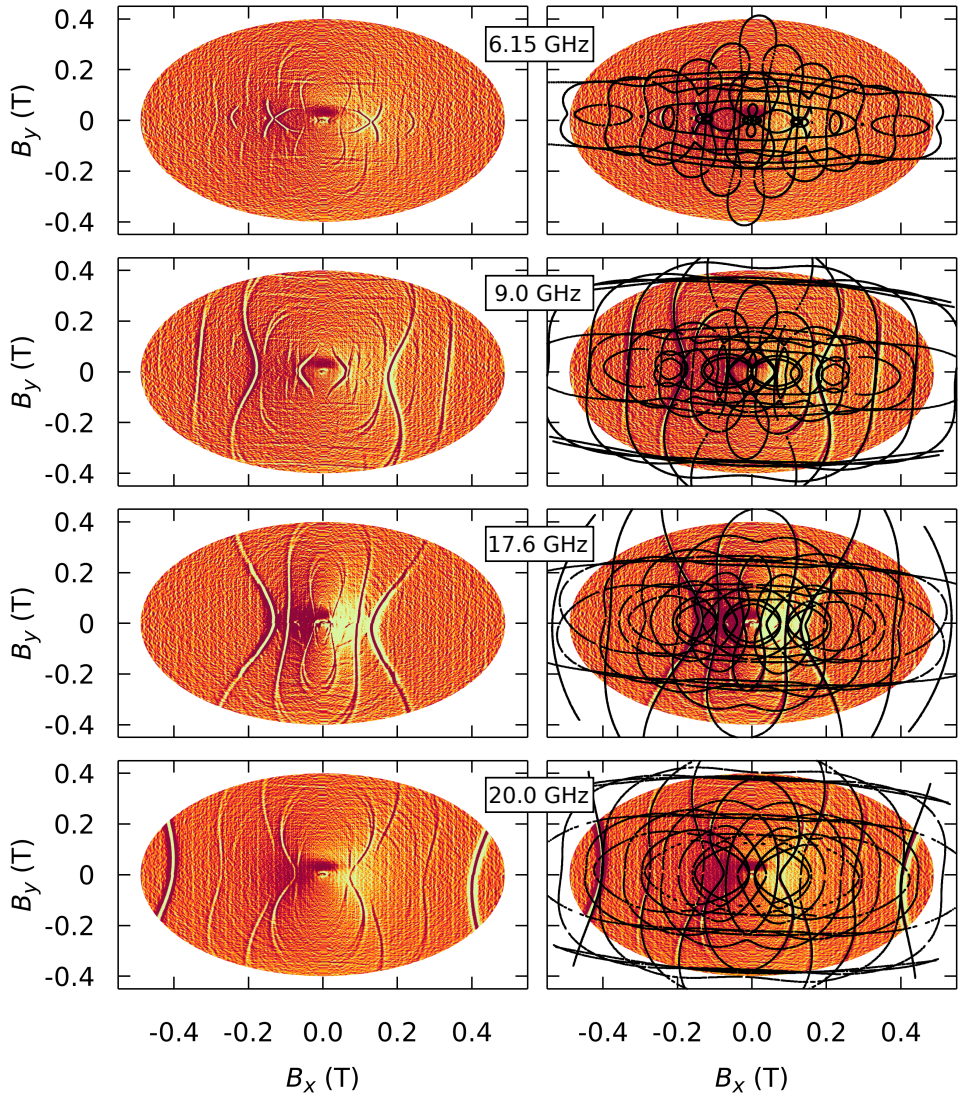


Figure 5.8: (*left*) Resonance maps obtained by sweeping the angle at fixed frequency of 6.15 GHz, 9 GHz, 17.6 GHz and 20 GHz. (*right*) Fit of resonance maps giving $g = 1.96$, $\phi = 3^\circ$, $B_2^0 = -6.80 \times 10^{-1}$ GHz, $B_4^0 = -1.57 \times 10^{-3}$ GHz, $B_6^0 = 1.6 \times 10^{-7}$ GHz, $B_2^2 = -2.75 \times 10^{-1}$ GHz and $B_4^4 = 3.38 \times 10^{-3}$ GHz.

In the following we discuss the numerical procedure used to fit the resonance maps. The initial set of parameters, B_k^0 , are obtained from the analysis made in the axial approximation, and take the transverse ligand field coefficients to be of

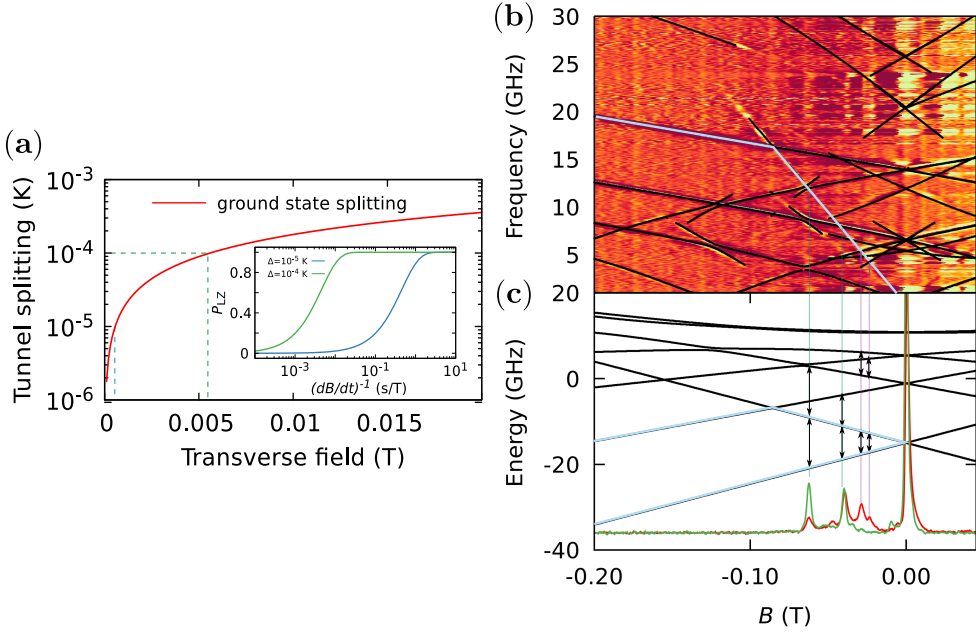


Figure 5.9: **a)** The magnitude of the ground state tunnel splitting as a function of an applied transverse magnetic field. (*inset*) Nonadiabatic transition rates when sweeping the zero field resonance, computed with the use of the LZS model. **b)** The fitted resonance map in zero transverse field and **c)** the corresponding Zeeman diagram obtained by the diagonalization of Eq. 5.4. Derivative of magnetization for $T = 25$ mK (*green*) and $T = 100$ mK (*red*) with the vertical dotted lines identify the position of the steps in the magnetization curve.

the same order as diagonal terms. We then diagonalize the spin Hamiltonian at the experimental points. We evaluate the deviation square between the theoretical prediction and experimental points: $\chi^2 = \sum (v_{exp} - v_{SHP})^2$ and minimize χ^2 in an iterative process by using the Marquardt-Levenberg nonlinear algorithm with: g , ϕ , B_2^0 , B_4^0 , B_6^0 , B_2^2 , B_4^4 as fit parameters.

Figures 5.7 and 5.8 show the simultaneous fit (black lines) of both the transverse field maps and angular maps, with $g = 1.96$, $\phi = 2.8^\circ$, $B_2^0 = -6.80 \times 10^{-1}$ GHz, $B_4^0 = -1.57 \times 10^{-3}$ GHz, $B_6^0 = 1.6 \times 10^{-7}$ GHz, $B_2^2 = -2.75 \times 10^{-1}$ GHz and $B_4^4 = 3.38 \times 10^{-3}$ GHz. One should notice that, the resonance lines broaden and then split at large transverse fields due to the presence of two inequivalent Gd^{3+} centers with a slight angle between their easy axis. Then, we obtain an unexpected large contribution of the orthorhombic term, that points to a low symmetry at the Gd^{3+} ion site. The $B_2^2 O_2^2$ term leads to the observation of the oscillation of the tunnel

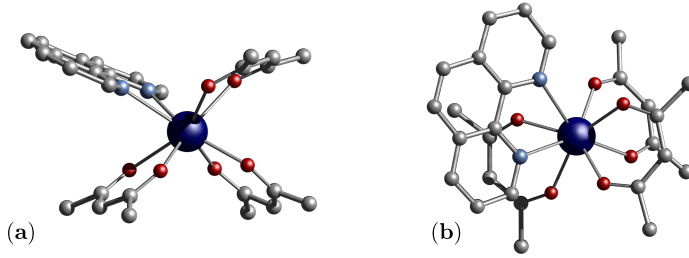


Figure 5.10: a) Side view and b) top view of $^{157}\text{Gd}(\text{tmhd})_3\text{Phen}$ molecule (Me and Hydrogen groups have been omitted for clarity. Colour code: Gd, dark blue; O, red; N, cyan; C, grey).

splitting between $|1/2\rangle$ and $|-5/2\rangle$ (blue circle in Fig.5.7) bearing evidence to the phase interference effect. Finally, we found a 2.8° angle misalignment ϕ between the swept plane and the easy axis of the complex that explains the mixing of levels with odd selection rule: $\Delta m = 3$ and $\Delta m = 5$.

Equipped with the detailed knowledge on the $\text{Et}_4\text{N}[\text{}^{160}\text{GdPc}_2]$ spin Hamiltonian, we are now in the position to solve the issues that were raised when we presented the μSQUID measurements.

Kramer degeneracy

When discussing the tunneling dynamics of $\text{Et}_4\text{N}[\text{}^{160}\text{GdPc}_2]$ in zero field it was hypothesized that the degeneracy predicted by Kramer's theorem is broken by environmental interactions, mainly spin-spin interactions of dipolar nature with other molecular or nuclear spins.

The precision of the spin Hamiltonian that we obtained by using the $\mu\text{SQUID-EPR}$ module allows us to evaluate the magnitude of the ground state tunnel splitting as a function of an applied transverse magnetic field (Fig.5.9a). As expected for a half integer spin systems, a sharp increase in Δ with the applied transverse field is observed. The dotted lines show the lower and upper bound estimates for environmental magnetic field that predicts a tunnel splitting in the $10^{-4} - 10^{-5}$ K range.

The corresponding nonadiabatic transition rates when sweeping the zero field resonance, computed with the use of the LZS model,

$$P_{\text{LZ}} = 1 - \exp\left(-\frac{\pi\Delta^2}{2\hbar\mu_0\mu_B|\delta m|dB/dt}\right)$$

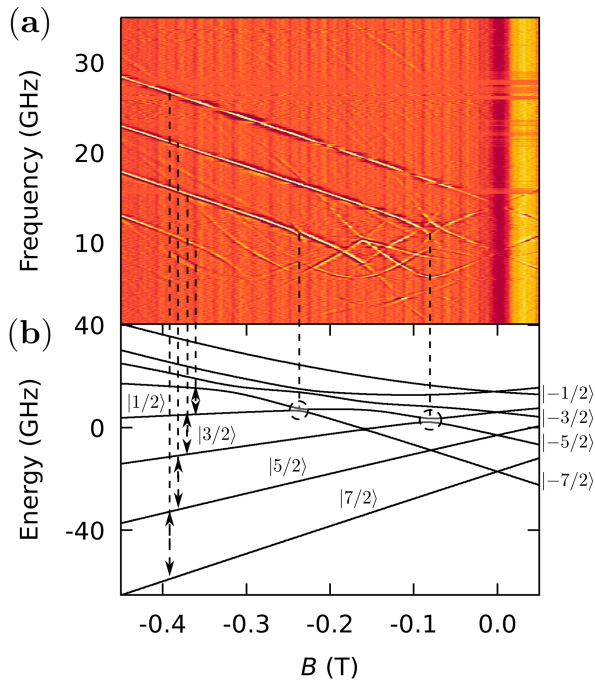


Figure 5.11: **a)** Resonant transition map and **b)** the Zeeman diagram when sweeping a direction close to the easy axis, with the following spin Hamiltonian parameters: $\phi = 18.67^\circ$, $B_2^0 = -8.0 \times 10^{-1}$ GHz, $B_4^0 = -3.42 \times 10^{-4}$ GHz, $B_6^0 = 1.5 \times 10^{-6}$ GHz, $B_2^2 = -4.23 \times 10^{-1}$ GHz, $B_4^4 = -1.2 \times 10^{-4}$ GHz, with $g_z = 2.27$, $g_x = 2.0$ and $g_y = 1.77$. with marked level anticrossings.

is shown in the inset of Fig.5.9a. From $P_{LZ}(dB/dt)$ curves can be seen that for sweeping rates smaller than 1 T/s, the tunnel probability is close to unity, that is, all molecules are expected to tunnel.

Note that, experimentally we measure only about 75% of molecules to relax in zero field. The difference can be attributed to environmental effects like the reshuffling of the local fields and to decoherence interactions that destroy the phase of the tunneling spin.

Spin-spin cross relaxation

The second feature that we discussed is the fine structure observed in the $B \in [0.02 : 0.08]$ T region. Figure 5.9b shows the fitted resonance map for zero transverse field and the corresponding Zeeman digram obtained by the diagonalization of Eq. 5.4.

The derivative of magnetization for $T = 25$ mK and $T = 100$ mK with the vertical dotted lines identify the position of the steps in the magnetization curve.

We immediately see that, our initial fit based solely on μSQUID measurements is incorrect. Instead, all observed transitions correspond to spin-spin cross relaxation transitions. The steps that are observed at the lowest accessible temperature correspond to the transitions: $|7/2, 7/2\rangle$ to $|-7/2, -5/2\rangle$ and $|7/2, 7/2\rangle$ to $|-7/2, -3/2\rangle$. While the steps that emerge with increasing temperature correspond to $|7/2, 5/2\rangle$ to $|-7/2, 3/2\rangle$ and $|7/2, 5/2\rangle$ to $|-7/2, 1/2\rangle$, transitions.

The latter processes require the $|5/2\rangle$ state to be populated and thus are not observed at $T = 25$ mK because all the molecules are in the ground state $|7/2\rangle$.

5.2 Measurements on $^{157}\text{Gd}(\text{tmhd})_3\text{Phen}$

Bellow we discuss measurements on the second Gd^{3+} molecule, $^{157}\text{Gd}(\text{tmhd})_3\text{Phen}$ and highlight the potential held by the μSQUID -EPR technique for magnetostructural analysis.

Synthesis and chemical structure

Similar to $\text{Et}_4\text{N}[^{160}\text{GdPC}_2]$ all the measurement were performed on micrometer sized diluted monocrystals containing $^{157}\text{Gd}(\text{tmhd})_3\text{Phen}$ in an isostructural, diamagnetic matrix of $\text{Y}(\text{tmhd})_3\text{Phen}$ with $[\text{Gd}^{3+} / \text{Y}]$ ratio of 5%. The $^{157}\text{Gd}(\text{tmhd})_3\text{Phen}$ molecule (Fig.5.10) crystallise in the triclinic space group with the entire molecule in the asymmetric unit. Two molecules reside in the unit cell (Fig.5.10). At the metal side, each metal ion possesses a N_2O_6 coordination geometry formed by six oxygen atoms from the tmhd groups and two nitrogen atoms of the Phen. The $\text{Gd}^{3+} - \text{O}$ distances range between 2.2994 Å to 2.3767 Å, whilst the $\text{Gd}^{3+} - \text{N}$ distances in both cases are longer, with values ranging from 2.6110 Å to 2.6151 Å. The coordination geometry around the dysprosium ions can be best described as a square antiprism with a CShM of 0.610.

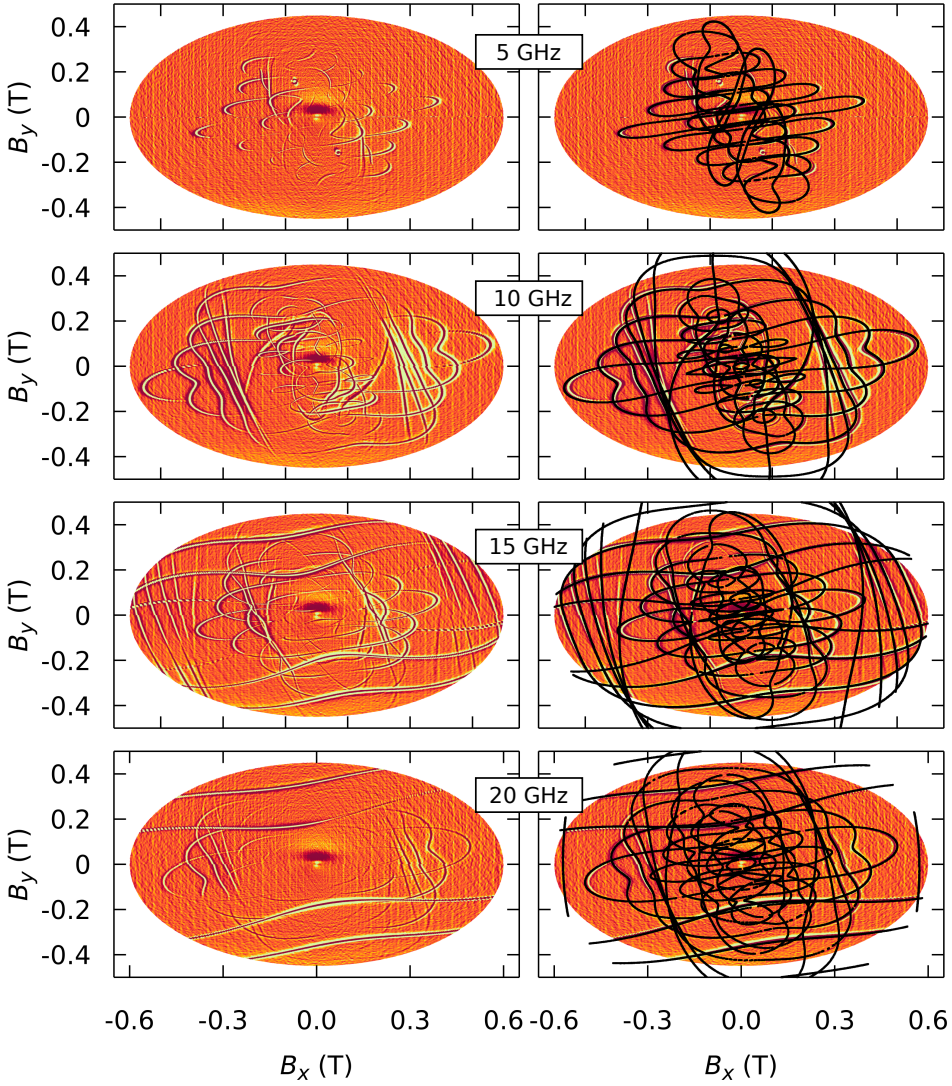


Figure 5.12: Fit of the angular resonance maps at different RF frequencies with the following parameters: $\phi = 18.67^\circ$, $B_2^0 = -8.0 \times 10^{-1}$ GHz, $B_4^0 = -3.42 \times 10^{-4}$ GHz, $B_6^0 = 1.5 \times 10^{-6}$ GHz, $B_2^2 = -4.23 \times 10^{-1}$ GHz, $B_4^4 = -1.2 \times 10^{-4}$ GHz, with $g_z = 2.27$, $g_x = 2.0$ and $g_y = 1.77$.

Figure 5.11 shows that the resonance map obtained while sweeping a direction close to the easy axis and Fig.5.12 displays the angular dependence maps.

To fit the resonance maps, we follow the same procedure as described for $\text{Et}_4\text{N}[\text{}^{160}\text{GdPc}_2]$. The resonances are fit with the following spin Hamiltonian parameters: $\phi = 18.67^\circ$, $B_2^0 = -8.0 \times 10^{-1}$ GHz, $B_4^0 = -3.42 \times 10^{-4}$ GHz, $B_6^0 = 1.5 \times 10^{-6}$ GHz, $B_2^2 = -4.23 \times 10^{-1}$ GHz, $B_4^4 = -1.2 \times 10^{-4}$ GHz, with $g_z = 2.27$, $g_x = 2$ and $g_y = 1.77$.

As one would expect from the crystal structure, the $^{157}\text{Gd}(\text{tmhd})_3\text{Phen}$ complex displays a lower symmetry at the Gd^{3+} site with significantly larger orthorhombic term. However, the striking difference was found in the Zeeman interaction which now is written as a function of an anisotropic g-value: $\mathcal{H}_Z = (g_z\mu_B B_z S_z + g_x\mu_B B_x S_x + g_y\mu_B B_y S_y)$ with $g_z = 2.27$, $g_x = 2.0$ and $g_y = 1.77$. With significant deviation from the isotropic free electron value, $g = 2.0023$. At the moment, it is still not clear if this is an artifact of the fitting procedure or if the ligand field is the cause of this anomaly.

6 Conclusions and Outlook

In this thesis I discuss quantum phenomenologies observed in mononuclear and dinuclear lanthanide single molecule magnets. Even though they have been under intense investigation in the last two decades, their chemical variety still makes for a scientifically rich landscape.

A perfect example of the depth of the field of molecular magnets is made by the TbPc_2 SMM that was central to the development of both the field of single molecule magnets and molecular spintronics. The analysis of its magnetic bistability proved that a molecular complex with a single magnetic center can exhibit a large effective energy barrier [134]. Shortly after, the possibility to dilute the TbPc_2 molecules in an isostructural diamagnetic matrix and the strong hyperfine interaction, characteristic of lanthanide ions, allowed to experimentally evidence the resonant quantum tunneling between mixed states of electronic and nuclear origin [135]. Furthermore, the planar structure of the molecule made possible its deposition on different substrates, and thus subsequent inclusion in spintronics devices [171, 136]. The TbPc_2 single molecule spin transistor was first used to read out and control both the electronic and the nuclear spin [133], and then to successfully implement quantum algorithms [12]. The same device provided the experimental means to explore how the effective character of the resonant tunneling changes when the dephasing of environmental or measurement origin is taken into account [146]. Despite being the central object in a great number of studies, we showed that many aspects of its dynamics were poorly understood.

We started by taking an in depth look at the potential non-axial interactions that can promote QTM transitions between the hyperfine states of the TbPc_2 SMM. The rare combination of strong uniaxial character of the ligand field with the tight hyperfine coupling results in characteristics that are substantially different from the ones in transition metal ion molecular compounds [172]. The nuclear spin dominates the dynamics of the molecular spin, as the usual suspects in the form of the environmental transverse magnetic field and non-axial ligand field interactions fail to explain the transitions that do not conserve the nuclear spin. It was then proposed through the non-axial quadrupolar interaction a potential mechanism that mixes the hyperfine states.

Crystal defects, solvent disorder, lattice mismatch between the YPC_2 and TbPC_2 molecules, and also the presence of a radical electronic spin non-uniformly distributed on the phthalocyanine ligands, are all factors that can lead to significant inhomogeneities in the electric field that can couple to the quadrupolar moment of the ^{159}Tb nucleus. The problem was investigated in a subsequent study [173] and indeed was found that molecular distortions leads to significant non-axial terms in the quadrupolar interaction, thus confirming our findings. This result is important both from an academic point of view as similar dynamics can be observed in other lanthanide single molecule magnets, and from a technological one as tunneling between hyperfine states can be used to initialize and read-out the nuclear spins when implementing quantum protocols.

We then present the novel approach by which we fit the magnetic hysteresis loops and study the Landau-Zener dynamics. The incoherent LZ dynamics was used to infer relevant information regarding the quantum dynamics in crystals of molecular magnets as both the tunneling time and dephasing time of different hyperfine anticrossings were determined through low temperature magnetometry. The powerful combination of μSQUID measurements with appropriate theoretical tools in the form of Lindblad operators was shown to have the potential to complement the resonant techniques used so far to study coherence in SMMs. It should be noted that, previous treatments of the dissipative Landau-Zener problem are known to theory [174], however the main advantage of the Lindblad formalism lies in the ability to study the decoherence process without requiring the detailed knowledge of the coupling between the molecular spin and the environmental degrees of freedom. Establishing the connection between the phenomenological model that uses Lindblad operators and a microscopic description that includes explicitly the environmental degrees of freedom is an important outlook of the present study.

The obtained insight in the LZ dynamics allowed us to investigate the thermalization of ^{159}Tb nuclear spin belonging to the TbPC_2 complex. Surprisingly, it was found that the observed relaxation is due to the phonon modulation of the hyperfine interaction. Then, it was argued that the direct contact of the nuclear spins to the phonon modes in lanthanide compounds is an important feature that has to be considered both in the continuous search for molecular compounds with optimized magnetic properties and fundamental investigations on the spin bath dynamics. The direct nuclear spin phonon relaxation rate also gives the lower bound for the relaxation rate of the nuclear spins in future candidates for molecular spintronics devices.

The resonant QTM has also been studied in a dimeric $\text{Tb}_2\text{Pc}^{\text{Hx8}}\text{PC}_2$ SMM. Low temperature μSQUID measurements allowed the determination of the hyperfine and quadrupolar parameters. The analysis of the magnetization characteristics showed

that the resonant QTM transitions can be ascribed to co-tunneling events of the Tb electronic spins. It is argued that the transitions that do not conserve the nuclear spins are induced by the nuclear quadrupolar interaction as it was the case for TbPc₂. The evidence of the relaxation of ¹⁵⁹Tb nuclear spins in the molecular environment of the Tb₂Pc₃ was presented and it was noticed that they thermalize on the same time scale as the ¹⁵⁹Tb spins in TbPc₂ complex. This is not a surprising result as the magnitude of the hyperfine interaction is similar in both compounds.

The effect of the nuclear isotopes on the molecular spin relaxation was studied through the use of two model system: Dy(tmhd)₃bpm and Ho^{III}F₂[15-MC_{Ni}-5]. Experimental evidence was provided to show that the presence of the nuclear spin leads to a significant increase of the relaxation rate at crossover temperatures, that is, when molecular spin tunneling and phonon assisted transitions occur with comparable rate. It was hypothesized that the missing ingredient for constructing a quantitative explanation of the observed dynamics is the thermal fluctuations of the nuclear spin. Thus, the characteristics of their relaxation process is explained by including nuclear spin fluctuations in the theoretical framework of phonon assisted tunneling. And it was found that, indeed, thermal fluctuations of the nuclear spins in lanthanide SMMs open additional relaxation channels for the molecular spin and thus leads to an exponential increase of the relaxation time.

Finally, resonant photon absorption in Et₄N[¹⁶⁰GdPc₂] and Gd(tmhd)₃Phen was investigated with a home built EPR device that uses the μ SQUID as a magnetic probe. The resonance transition maps are successfully fit to a set of spin Hamiltonian parameters and immediate results like, the true point symmetry at the Gd³⁺ site, the magnitude of the axial and non-axial interactions, the presence of two inequivalent centers, are pointed out. The "high resolution" of the obtained spin Hamiltonian is used to explain the broken Kramer's degeneracy in zero field, the fine structure in the magnetization curve as spin-spin cross relaxation processes. We finish by a short investigation of the ¹⁵⁷Gd(tmhd)₃Phen complex where we highlight its potential for magnetostructural analysis.

In this thesis, exploits in the investigation of the quantum phenomenologies related to the magnetic properties of molecular magnets are reported. Even though there still remain a number of open questions regarding the physics of these fascinating mesoscopic systems, both theoretical and experimental progress has been reported. This work represents another step towards understanding the complex dynamics of an ensemble of interacting quantum systems, so that we can get closer to functional devices that make use of their properties.

Bibliography

- [1] A. Caneschi, D. Gatteschi, R. Sessoli, A. L. Barra, L. C. Brunel, and M. Guillot, "Alternating current susceptibility, high field magnetization, and millimeter band epr evidence for a ground $s=10$ state in $[Mn_{12}O_{12}(CH_3COO)_{16}(H_2O)_4] \cdot 2CH_3COOH \cdot 4H_2O$," *Journal of the American Chemical Society*, vol. 113, no. 15, pp. 5873–5874, 1991.
- [2] R. Sessoli, H.-L. Tsai, A. R. Schake, W. Sheyi, J. B. Vincent, K. Folting, D. Gatteschi, G. Christou, and D. N. Hendrickson, "High-spin molecules: $[Mn_{12}O_{12}(O_2CR)_{16}(H_2O)_4]$," *Journal of the American Chemical Society*, vol. 115, no. 5, pp. 1804–1816, 1993.
- [3] J. R. Friedman, M. Sarachik, J. Tejada, and R. Ziolo, "Macroscopic measurement of resonant magnetization tunneling in high-spin molecules," *Physical review letters*, vol. 76, no. 20, p. 3830, 1996.
- [4] L. Thomas, F. Lioni, R. Ballou, D. Gatteschi, *et al.*, "Macroscopic quantum tunnelling of magnetization in a single crystal of nanomagnets," *Nature*, vol. 383, no. 6596, p. 145, 1996.
- [5] C. Sangregorio, T. Ohm, C. Paulsen, R. Sessoli, and D. Gatteschi, "Quantum tunneling of the magnetization in an iron cluster nanomagnet," *Physical review letters*, vol. 78, no. 24, p. 4645, 1997.
- [6] W. Wernsdorfer and R. Sessoli, "Quantum phase interference and parity effects in magnetic molecular clusters," *Science*, vol. 284, no. 5411, pp. 133–135, 1999.
- [7] D. Gatteschi and R. Sessoli, "Quantum tunneling of magnetization and related phenomena in molecular materials," *Angewandte Chemie International Edition*, vol. 42, no. 3, pp. 268–297, 2003.
- [8] J. R. Friedman and M. P. Sarachik, "Single-molecule nanomagnets," *Annu. Rev. Condens. Matter Phys.*, vol. 1, no. 1, pp. 109–128, 2010.
- [9] W. Lu and C. M. Lieber, "Nanoelectronics from the bottom up," *Nature materials*, vol. 6, no. 11, pp. 841–850, 2007.

- [10] W. Wernsdorfer, N. Chakov, and G. Christou, "Determination of the magnetic anisotropy axes of single-molecule magnets," *Physical Review B*, vol. 70, no. 13, p. 132413, 2004.
- [11] C. A. Goodwin, F. Ortu, D. Reta, N. F. Chilton, and D. P. Mills, "Molecular magnetic hysteresis at 60 kelvin in dysprosocenium," *Nature*, vol. 548, no. 7668, p. 439, 2017.
- [12] C. Godfrin, A. Ferhat, R. Ballou, S. Klyatskaya, M. Ruben, W. Wernsdorfer, and F. Balestro, "Operating quantum states in single magnetic molecules: Implementation of grover's quantum algorithm," *Physical review letters*, vol. 119, no. 18, p. 187702, 2017.
- [13] D. N. Woodruff, R. E. Winpenny, and R. A. Layfield, "Lanthanide single-molecule magnets," *Chemical reviews*, vol. 113, no. 7, pp. 5110–5148, 2013.
- [14] A. Abragam and B. Bleaney, *Electron paramagnetic resonance of transition ions*. OUP Oxford, 2012.
- [15] J. M. Clemente-Juan, E. Coronado, and A. Gaita-Ariño, "Mononuclear lanthanide complexes: Use of the crystal field theory to design single-ion magnets and spin qubits," *Lanthanides and Actinides in Molecular Magnetism*, pp. 27–60, 2015.
- [16] K. Stevens, "Matrix elements and operator equivalents connected with the magnetic properties of rare earth ions," *Proceedings of the Physical Society. Section A*, vol. 65, no. 3, p. 209, 1952.
- [17] N. Ishikawa, M. Sugita, T. Okubo, N. Tanaka, T. Iino, and Y. Kaizu, "Determination of ligand-field parameters and f-electronic structures of double-decker bis (phthalocyaninato) lanthanide complexes," *Inorganic chemistry*, vol. 42, no. 7, pp. 2440–2446, 2003.
- [18] O. Waldmann, "A criterion for the anisotropy barrier in single-molecule magnets," *Inorganic chemistry*, vol. 46, no. 24, pp. 10035–10037, 2007.
- [19] N. Ishikawa, M. Sugita, T. Ishikawa, S.-y. Koshihara, and Y. Kaizu, "Mononuclear lanthanide complexes with a long magnetization relaxation time at high temperatures: a new category of magnets at the single-molecular level," *The Journal of Physical Chemistry B*, vol. 108, no. 31, pp. 11265–11271, 2004.
- [20] S. K. Langley, D. P. Wielechowski, B. Moubaraki, and K. S. Murray, "Enhancing the magnetic blocking temperature and magnetic coercivity of {Cr III2 Ln III2} single-molecule magnets via bridging ligand modification," *Chemical Communications*, vol. 52, no. 73, pp. 10976–10979, 2016.

- [21] R. Layfield, F.-S. Guo, B. Day, Y.-C. Chen, M.-L. Tong, and A. Mansikamäkki, "A dysprosium metallocene single-molecule magnet functioning at the axial limit," *Angewandte Chemie International Edition*, 2017.
- [22] Y.-Z. Zheng, Z. Zheng, and X.-M. Chen, "A symbol approach for classification of molecule-based magnetic materials exemplified by coordination polymers of metal carboxylates," *Coordination Chemistry Reviews*, vol. 258, pp. 1–15, 2014.
- [23] D. Gatteschi, R. Sessoli, and J. Villain, *Molecular nanomagnets*, vol. 5. Oxford University Press on Demand, 2006.
- [24] S. Hill, S. Datta, J. Liu, R. Inglis, C. J. Milios, P. L. Feng, J. J. Henderson, E. del Barco, E. K. Brechin, and D. N. Hendrickson, "Magnetic quantum tunneling: insights from simple molecule-based magnets," *Dalton Transactions*, vol. 39, no. 20, pp. 4693–4707, 2010.
- [25] D. Gatteschi and A. Bencini, "Electron paramagnetic resonance of exchange coupled systems," 1990.
- [26] I. Tupitsyn and B. Barbara, "Quantum tunneling of magnetization in molecular complexes with large spins—effect of the environment," *Magnetism: Molecules to Materials: 5 Volumes Set*, pp. 109–168, 2001.
- [27] B. Barbara, "Quantum tunneling of the collective spins of single-molecule magnets: From early studies to quantum coherence," in *Molecular Magnets*, pp. 17–60, Springer, 2014.
- [28] A. Garg, "Topologically quenched tunnel splitting in spin systems without kramers' degeneracy," *EPL (Europhysics Letters)*, vol. 22, no. 3, p. 205, 1993.
- [29] R. Schilling, "Quantum spin-tunneling: a path integral approach," in *Quantum Tunneling of Magnetization—QTM'94*, pp. 59–76, Springer, 1995.
- [30] D. Garanin, "Spin tunnelling: a perturbative approach," *Journal of Physics A: Mathematical and General*, vol. 24, no. 2, p. L61, 1991.
- [31] F. Hartmann-Boutron, P. Politi, and J. Villain, "Tunneling and magnetic relaxation in mesoscopic molecules," *International Journal of Modern Physics B*, vol. 10, no. 21, pp. 2577–2637, 1996.
- [32] W. Wernsdorfer, T. Ohm, C. Sangregorio, R. Sessoli, D. Mailly, and C. Paulsen, "Observation of the distribution of molecular spin states by resonant quantum tunneling of the magnetization," *Physical review letters*, vol. 82, no. 19, p. 3903, 1999.

- [33] W. Wernsdorfer, A. Caneschi, R. Sessoli, D. Gatteschi, A. Cornia, V. Villar, and C. Paulsen, "Effects of nuclear spins on the quantum relaxation of the magnetization for the molecular nanomagnet Fe_8 ," *Physical review letters*, vol. 84, no. 13, p. 2965, 2000.
- [34] J. J. Alonso and J. F. Fernández, "Tunnel window's imprint on dipolar field distributions," *Physical review letters*, vol. 87, no. 9, p. 097205, 2001.
- [35] I. Tupitsyn, P. Stamp, and N. Prokof'ev, "Hole digging in ensembles of tunneling molecular magnets," *Physical Review B*, vol. 69, no. 13, p. 132406, 2004.
- [36] L. Landau, "Zur theorie der energieubertragung. ii," *Phys. Z. Sowjetunion*, vol. 2, no. 46, pp. 1–13, 1932.
- [37] C. Zener, "Non-adiabatic crossing of energy levels," in *Proceedings of the Royal Society of London A: Mathematical, Physical and Engineering Sciences*, vol. 137, pp. 696–702, The Royal Society, 1932.
- [38] E. Stueckelberg, "Theory of inelastic collisions between atoms(theory of inelastic collisions between atoms, using two simultaneous differential equations)," *Helv. Phys. Acta,(Basel)*, vol. 5, pp. 369–422, 1932.
- [39] S. Miyashita, "Dynamics of the magnetization with an inversion of the magnetic field," *Journal of the Physical Society of Japan*, vol. 64, no. 9, pp. 3207–3214, 1995.
- [40] S. Miyashita, "Observation of the energy gap due to the quantum tunneling-making use of the landau-zener mechanism," *Journal of the Physical Society of Japan*, vol. 65, no. 8, pp. 2734–2735, 1996.
- [41] M. Thorwart, M. Grifoni, and P. Hänggi, "Tunneling and vibrational relaxation in driven multi-level systems," *Phys. Rev. Lett.*, vol. 85, no. quant-ph/9912024, p. 860, 2000.
- [42] M. N. Leuenberger and D. Loss, "Incoherent zener tunneling and its application to molecular magnets," *Physical Review B*, vol. 61, no. 18, p. 12200, 2000.
- [43] W. Wernsdorfer, S. Bhaduri, A. Vinslava, and G. Christou, "Landau-zener tunneling in the presence of weak intermolecular interactions in a crystal of Mn_4 single-molecule magnets," *Physical Review B*, vol. 72, no. 21, p. 214429, 2005.
- [44] G. Taran, E. Bonet, and W. Wernsdorfer, "Decoherence measurements in crystals of molecular magnets," *Physical Review B*, vol. 99, no. 18, p. 180408, 2019.

- [45] P. Bruno, "Berry phase, topology, and degeneracies in quantum nanomagnets," *Physical review letters*, vol. 96, no. 11, p. 117208, 2006.
- [46] Y. N. Demkov and P. B. Kurasov, "Von neumann-wigner theorem: Level repulsion and degenerate eigenvalues," *Theoretical and Mathematical Physics*, vol. 153, no. 1, pp. 1407–1422, 2007.
- [47] J. Henderson, C. Koo, P. Feng, E. Del Barco, S. Hill, I. Tupitsyn, P. Stamp, and D. Hendrickson, "Manifestation of spin selection rules on the quantum tunneling of magnetization in a single-molecule magnet," *Physical review letters*, vol. 103, no. 1, p. 017202, 2009.
- [48] W. Wernsdorfer, S. Bhaduri, C. Boskovic, G. Christou, and D. Hendrickson, "Spin-parity dependent tunneling of magnetization in single-molecule magnets," *Physical Review B*, vol. 65, no. 18, p. 180403, 2002.
- [49] E. Del Barco, A. D. Kent, S. Hill, J. North, N. Dalal, E. Rumberger, D. Hendrickson, N. Chakov, and G. Christou, "Magnetic quantum tunneling in the single-molecule magnet Mn_{12} -acetate," *Journal of Low Temperature Physics*, vol. 140, no. 1-2, pp. 119–174, 2005.
- [50] H. De Raedt, S. Miyashita, K. Michielsen, and M. Machida, "Dzyaloshinskii-moriya interactions and adiabatic magnetization dynamics in molecular magnets," *Physical Review B*, vol. 70, no. 6, p. 064401, 2004.
- [51] B. D. Josephson, "Possible new effects in superconductive tunnelling," *Physics letters*, vol. 1, no. 7, pp. 251–253, 1962.
- [52] D. Koelle, R. Kleiner, F. Ludwig, E. Dantsker, and J. Clarke, "High-transition-temperature superconducting quantum interference devices," *Reviews of Modern Physics*, vol. 71, no. 3, p. 631, 1999.
- [53] Y. Aharonov and D. Bohm, "Significance of electromagnetic potentials in the quantum theory," *Physical Review*, vol. 115, no. 3, p. 485, 1959.
- [54] W. Wernsdorfer, M. Soler, G. Christou, and D. Hendrickson, "Quantum phase interference (berry phase) in single-molecule magnets of $[\text{Mn}_{12}]^{2-}$," *Journal of applied physics*, vol. 91, no. 10, pp. 7164–7166, 2002.
- [55] W. Wernsdorfer, N. Chakov, and G. Christou, "Quantum phase interference and spin-parity in Mn_{12} single-molecule magnets," *Physical review letters*, vol. 95, no. 3, p. 037203, 2005.

- [56] S. Adams, E. H. da Silva Neto, S. Datta, J. Ware, C. Lampropoulos, G. Christou, Y. Myasoedov, E. Zeldov, and J. R. Friedman, "Geometric-phase interference in a $m \times n \times 12$ single-molecule magnet with fourfold rotational symmetry," *Physical review letters*, vol. 110, no. 8, p. 087205, 2013.
- [57] H. M. Quddusi, J. Liu, S. Singh, K. Heroux, E. Del Barco, S. Hill, and D. Hendrickson, "Asymmetric berry-phase interference patterns in a single-molecule magnet," *Physical review letters*, vol. 106, no. 22, p. 227201, 2011.
- [58] C. M. Ramsey, E. Del Barco, S. Hill, S. J. Shah, C. C. Beedle, and D. N. Hendrickson, "Quantum interference of tunnel trajectories between states of different spin length in a dimeric molecular nanomagnet," *Nature Physics*, vol. 4, no. 4, pp. 277–281, 2008.
- [59] A.-L. Barra, P. Debrunner, D. Gatteschi, C. E. Schulz, and R. Sessoli, "Superparamagnetic-like behavior in an octanuclear iron cluster," *EPL (Europhysics Letters)*, vol. 35, no. 2, p. 133, 1996.
- [60] S. Mossin, M. Stefan, P. ter Heerdt, A. Bouwen, E. Goovaerts, and H. Weihe, "Fourth-order zero-field splitting parameters of $[mn(\text{cyclam})\text{br}_2]\text{br}$ determined by single-crystal w-band epr," *Applied Magnetic Resonance*, vol. 21, no. 3-4, pp. 587–596, 2001.
- [61] S. Bertaina, S. Gambarelli, T. Mitra, B. Tsukerblat, A. Müller, and B. Barbara, "Quantum oscillations in a molecular magnet," *Nature*, vol. 453, no. 7192, pp. 203–206, 2008.
- [62] L. Sorace, W. Wernsdorfer, C. Thirion, A.-L. Barra, M. Pacchioni, D. Mailly, and B. Barbara, "Photon-assisted tunneling in a Fe_8 single-molecule magnet," *Physical Review B*, vol. 68, no. 22, p. 220407, 2003.
- [63] M. Bal, J. R. Friedman, Y. Suzuki, K. Mertes, E. Rumberger, D. Hendrickson, Y. Myasoedov, H. Shtrikman, N. Avraham, and E. Zeldov, "Photon-induced magnetization reversal in the Fe_8 single-molecule magnet," *Physical Review B*, vol. 70, no. 10, p. 100408, 2004.
- [64] W. Wernsdorfer, A. Müller, D. Mailly, and B. Barbara, "Resonant photon absorption in the low-spin molecule $\nu 15$," *EPL (Europhysics Letters)*, vol. 66, no. 6, p. 861, 2004.
- [65] K. Petukhov, W. Wernsdorfer, A.-L. Barra, and V. Mosser, "Resonant photon absorption in Fe_8 single-molecule magnets detected via magnetization measurements," *Physical Review B*, vol. 72, no. 5, p. 052401, 2005.

- [66] I. I. Rabi, "Space quantization in a gyrating magnetic field," *Physical Review*, vol. 51, no. 8, p. 652, 1937.
- [67] M. Grifoni and P. Hänggi, "Driven quantum tunneling," *Physics Reports*, vol. 304, no. 5, pp. 229–354, 1998.
- [68] A. Schweiger and G. Jeschke, *Principles of pulse electron paramagnetic resonance*. Oxford University Press on Demand, 2001.
- [69] W. H. Zurek, "Decoherence, einselection, and the quantum origins of the classical," *Reviews of modern physics*, vol. 75, no. 3, p. 715, 2003.
- [70] S. Takahashi, I. Tupitsyn, J. Van Tol, C. Beedle, D. Hendrickson, and P. Stamp, "Decoherence in crystals of quantum molecular magnets," *Nature*, vol. 476, no. 7358, pp. 76–79, 2011.
- [71] J. Shim, S. Bertaina, S. Gambarelli, T. Mitra, A. Müller, E. Baibekov, B. Malkin, B. Tsukerblat, and B. Barbara, "Decoherence window and electron-nuclear cross relaxation in the molecular magnet v 15," *Physical review letters*, vol. 109, no. 5, p. 050401, 2012.
- [72] A. Ardavan, O. Rival, J. J. Morton, S. J. Blundell, A. M. Tyryshkin, G. A. Timco, and R. E. Winpenny, "Will spin-relaxation times in molecular magnets permit quantum information processing?," *Physical review letters*, vol. 98, no. 5, p. 057201, 2007.
- [73] J. M. Zadrozny, J. Niklas, O. G. Poluektov, and D. E. Freedman, "Millisecond coherence time in a tunable molecular electronic spin qubit," *ACS central science*, vol. 1, no. 9, pp. 488–492, 2015.
- [74] J. Yang, Y. Wang, Z. Wang, X. Rong, C.-K. Duan, J.-H. Su, and J. Du, "Observing quantum oscillation of ground states in single molecular magnet," *Physical review letters*, vol. 108, no. 23, p. 230501, 2012.
- [75] S. Takahashi, J. van Tol, C. C. Beedle, D. N. Hendrickson, L.-C. Brunel, and M. S. Sherwin, "Coherent manipulation and decoherence of $s = 10$ single-molecule magnets," *Physical review letters*, vol. 102, no. 8, p. 087603, 2009.
- [76] K. Bader, D. Dengler, S. Lenz, B. Endeward, S.-D. Jiang, P. Neugebauer, and J. van Slageren, "Room temperature quantum coherence in a potential molecular qubit," *Nature communications*, vol. 5, 2014.
- [77] M. Atzori, L. Tesi, E. Morra, M. Chiesa, L. Sorace, and R. Sessoli, "Room-temperature quantum coherence and rabi oscillations in vanadyl phthalocyanine: Toward multifunctional molecular spin qubits," *Journal of the American Chemical Society*, vol. 138, no. 7, pp. 2154–2157, 2016.

- [78] J.-P. Cleuziou, W. Wernsdorfer, V. Bouchiat, T. Ondarçuhu, and M. Monthieux, "Carbon nanotube superconducting quantum interference device," *Nature nanotechnology*, vol. 1, no. 1, pp. 53–59, 2006.
- [79] L. Bogani and W. Wernsdorfer, "Molecular spintronics using single-molecule magnets," *Nature materials*, vol. 7, no. 3, pp. 179–186, 2008.
- [80] N. Roch, S. Florens, V. Bouchiat, W. Wernsdorfer, and F. Balestro, "Quantum phase transition in a single-molecule quantum dot," *Nature*, vol. 453, no. 7195, pp. 633–637, 2008.
- [81] S. Sanvito and A. R. Rocha, "Molecular-spintronics: the art of driving spin through molecules," *Journal of Computational and Theoretical Nanoscience*, vol. 3, no. 5, pp. 624–642, 2006.
- [82] A. S. Zyazin, J. W. van den Berg, E. A. Osorio, H. S. van der Zant, N. P. Konstantinidis, M. Leijnse, M. R. Wegewijs, F. May, W. Hofstetter, C. Danieli, *et al.*, "Electric field controlled magnetic anisotropy in a single molecule," *Nano letters*, vol. 10, no. 9, pp. 3307–3311, 2010.
- [83] S. Thiele, R. Vincent, M. Holzmann, S. Klyatskaya, M. Ruben, F. Balestro, and W. Wernsdorfer, "Electrical readout of individual nuclear spin trajectories in a single-molecule magnet spin transistor," *Physical review letters*, vol. 111, no. 3, p. 037203, 2013.
- [84] M. Urdampilleta, S. Klyatskaya, J.-P. Cleuziou, M. Ruben, and W. Wernsdorfer, "Supramolecular spin valves," *Nature materials*, vol. 10, no. 7, pp. 502–506, 2011.
- [85] M. N. Leuenberger and D. Loss, "Quantum computing in molecular magnets," *Nature*, vol. 410, no. 6830, pp. 789–793, 2001.
- [86] M. N. Leuenberger and D. Loss, "Grover algorithm for large nuclear spins in semiconductors," *Physical Review B*, vol. 68, no. 16, p. 165317, 2003.
- [87] F. Meier, J. Levy, and D. Loss, "Quantum computing with spin cluster qubits," *Physical review letters*, vol. 90, no. 4, p. 047901, 2003.
- [88] F. Troiani, A. Ghirri, M. Affronte, S. Carretta, P. Santini, G. Amoretti, S. Piligkos, G. Timco, and R. Winpenny, "Molecular engineering of antiferromagnetic rings for quantum computation," *Physical review letters*, vol. 94, no. 20, p. 207208, 2005.
- [89] S. Carretta, P. Santini, G. Amoretti, F. Troiani, and M. Affronte, "Spin triangles as optimal units for molecule-based quantum gates," *Physical Review B*, vol. 76, no. 2, p. 024408, 2007.

-
- [90] F. Troiani and M. Affronte, "Molecular spins for quantum information technologies," *Chemical Society Reviews*, vol. 40, no. 6, pp. 3119–3129, 2011.
- [91] J. Lehmann, A. Gaita-Arino, E. Coronado, and D. Loss, "Spin qubits with electrically gated polyoxometalate molecules," *Nature nanotechnology*, vol. 2, no. 5, pp. 312–317, 2007.
- [92] J. Bartolomé, F. Luis, and J. F. Fernández, "Molecular magnets," *Physics and Applications*, 2014.
- [93] D. P. DiVincenzo *et al.*, "The physical implementation of quantum computation," *arXiv preprint quant-ph/0002077*, 2000.
- [94] D. Deutsch and R. Jozsa, "Rapid solution of problems by quantum computation," in *Proceedings of the Royal Society of London A: Mathematical, Physical and Engineering Sciences*, vol. 439, pp. 553–558, The Royal Society, 1992.
- [95] A. Steane, "Quantum computing," *Reports on Progress in Physics*, vol. 61, no. 2, p. 117, 1998.
- [96] L. K. Grover, "A fast quantum mechanical algorithm for database search," in *Proceedings of the twenty-eighth annual ACM symposium on Theory of computing*, pp. 212–219, ACM, 1996.
- [97] P. W. Shor, "Polynomial-time algorithms for prime factorization and discrete logarithms on a quantum computer," *SIAM review*, vol. 41, no. 2, pp. 303–332, 1999.
- [98] E. Abe, H. Wu, A. Ardavan, and J. J. Morton, "Electron spin ensemble strongly coupled to a three-dimensional microwave cavity," *Applied Physics Letters*, vol. 98, no. 25, p. 251108, 2011.
- [99] I. Chiorescu, N. Groll, S. Bertaina, T. Mori, and S. Miyashita, "Magnetic strong coupling in a spin-photon system and transition to classical regime," *Physical Review B*, vol. 82, no. 2, p. 024413, 2010.
- [100] C. Clauss, D. Bothner, D. Koelle, R. Kleiner, L. Bogani, M. Scheffler, and M. Dressel, "Broadband electron spin resonance from 500 mhz to 40 ghz using superconducting coplanar waveguides," *Applied Physics Letters*, vol. 102, no. 16, p. 162601, 2013.
- [101] M. Jenkins, T. Hümmer, M. J. Martínez-Pérez, J. García-Ripoll, D. Zueco, and F. Luis, "Coupling single-molecule magnets to quantum circuits," *New Journal of Physics*, vol. 15, no. 9, p. 095007, 2013.

- [102] S. Carretta, A. Chiesa, F. Troiani, D. Gerace, G. Amoretti, and P. Santini, "Quantum information processing with hybrid spin-photon qubit encoding," *Physical review letters*, vol. 111, no. 11, p. 110501, 2013.
- [103] M. Trif, F. Troiani, D. Stepanenko, and D. Loss, "Spin electric effects in molecular antiferromagnets," *Physical Review B*, vol. 82, no. 4, p. 045429, 2010.
- [104] F. Troiani, V. Bellini, A. Candini, G. Lorusso, and M. Affronte, "Spin entanglement in supramolecular structures," *Nanotechnology*, vol. 21, no. 27, p. 274009, 2010.
- [105] J. Nossa, M. Islam, C. M. Canali, and M. Pederson, "First-principles studies of spin-orbit and dzyaloshinskii-moriya interactions in the {Cu 3} single-molecule magnet," *Physical Review B*, vol. 85, no. 8, p. 085427, 2012.
- [106] M. J. Graham, J. M. Zadrozny, M. Shiddiq, J. S. Anderson, M. S. Fataftah, S. Hill, and D. E. Freedman, "Influence of electronic spin and spin-orbit coupling on decoherence in mononuclear transition metal complexes," *Journal of the American Chemical Society*, vol. 136, no. 21, pp. 7623–7626, 2014.
- [107] G. A. Timco, S. Carretta, F. Troiani, F. Tuna, R. J. Pritchard, C. A. Muryn, E. J. McInnes, A. Ghirri, A. Candini, P. Santini, *et al.*, "Engineering the coupling between molecular spin qubits by coordination chemistry," *Nature nanotechnology*, vol. 4, no. 3, pp. 173–178, 2009.
- [108] J. Ferrando-Soria, E. M. Pineda, A. Chiesa, A. Fernandez, S. A. Magee, S. Carretta, P. Santini, I. J. Vitorica-Yrezabal, F. Tuna, G. A. Timco, *et al.*, "A modular design of molecular qubits to implement universal quantum gates," *Nature communications*, vol. 7, 2016.
- [109] A. Ardavan, A. M. Bowen, A. Fernandez, A. J. Fielding, D. Kaminski, F. Moro, C. A. Muryn, M. D. Wise, A. Ruggi, E. J. McInnes, *et al.*, "Engineering coherent interactions in molecular nanomagnet dimers," *arXiv preprint arXiv:1510.01694*, 2015.
- [110] J. M. Zadrozny, J. Niklas, O. G. Poluektov, and D. E. Freedman, "Multiple quantum coherences from hyperfine transitions in a vanadium (iv) complex," *Journal of the American Chemical Society*, vol. 136, no. 45, pp. 15841–15844, 2014.
- [111] L. Tesi, E. Lucaccini, I. Cimatti, M. Perfetti, M. Mannini, M. Atzori, E. Morra, M. Chiesa, A. Caneschi, L. Sorace, *et al.*, "Quantum coherence in a processable vanadyl complex: new tools for the search of molecular spin qubits," *Chemical Science*, vol. 7, no. 3, pp. 2074–2083, 2016.

- [112] S. Gómez-Coca, A. Urtizberea, E. Cremades, P. J. Alonso, A. Camón, E. Ruiz, and F. Luis, "Origin of slow magnetic relaxation in kramers ions with non-uniaxial anisotropy," *Nature communications*, vol. 5, 2014.
- [113] M. Shiddiq, D. Komijani, Y. Duan, A. Gaita-Ariño, E. Coronado, and S. Hill, "Enhancing coherence in molecular spin qubits via atomic clock transitions," *Nature*, vol. 531, no. 7594, pp. 348–351, 2016.
- [114] J. S. Hodges, J. C. Yang, C. Ramanathan, and D. G. Cory, "Universal control of nuclear spins via anisotropic hyperfine interactions," *Physical Review A*, vol. 78, no. 1, p. 010303, 2008.
- [115] P. Santini, S. Carretta, F. Troiani, and G. Amoretti, "Molecular nanomagnets as quantum simulators," *Physical review letters*, vol. 107, no. 23, p. 230502, 2011.
- [116] Y. Zhang, C. A. Ryan, R. Laflamme, and J. Baugh, "Coherent control of two nuclear spins using the anisotropic hyperfine interaction," *Physical review letters*, vol. 107, no. 17, p. 170503, 2011.
- [117] G. F. Whitehead, B. Cross, L. Carthy, V. A. Milway, H. Rath, A. Fernandez, S. L. Heath, C. A. Muryn, R. G. Pritchard, S. J. Teat, *et al.*, "Rings and threads as linkers in metal–organic frameworks and poly-rotaxanes," *Chemical Communications*, vol. 49, no. 65, pp. 7195–7197, 2013.
- [118] A. Ueda, S. Suzuki, K. Yoshida, K. Fukui, K. Sato, T. Takui, K. Nakasuji, and Y. Morita, "Hexamethoxyphenalenyl as a possible quantum spin simulator: An electronically stabilized neutral π radical with novel quantum coherence owing to extremely high nuclear spin degeneracy," *Angewandte Chemie International Edition*, vol. 52, no. 18, pp. 4795–4799, 2013.
- [119] A. Candini, S. Klyatskaya, M. Ruben, W. Wernsdorfer, and M. Affronte, "Graphene spintronic devices with molecular nanomagnets," *Nano letters*, vol. 11, no. 7, pp. 2634–2639, 2011.
- [120] M. Urdampilleta, S. Klyatskaya, M. Ruben, and W. Wernsdorfer, "Magnetic interaction between a radical spin and a single-molecule magnet in a molecular spin-valve," *ACS nano*, vol. 9, no. 4, pp. 4458–4464, 2015.
- [121] A. Ghirri, F. Troiani, and M. Affronte, "Quantum computation with molecular nanomagnets: Achievements, challenges, and new trends," in *Molecular Nanomagnets and Related Phenomena*, pp. 383–430, Springer, 2014.
- [122] R. Piquerel, *Retournement de l'aimantation assisté par un champ micro-onde d'une nanoparticule individuelle*. PhD thesis, Grenoble, 2012.

- [123] W. Wernsdorfer, "From micro-to nano-squids: applications to nanomagnetism," *Superconductor Science and Technology*, vol. 22, no. 6, p. 064013, 2009.
- [124] J. Luzon and R. Sessoli, "Lanthanides in molecular magnetism: so fascinating, so challenging," *Dalton Transactions*, vol. 41, no. 44, pp. 13556–13567, 2012.
- [125] J. Tang and P. Zhang, *Lanthanide single molecule magnets*. Springer, 2016.
- [126] M. Ganzhorn and W. Wernsdorfer, "Molecular quantum spintronics using single-molecule magnets," in *Molecular Magnets*, pp. 319–364, Springer, 2014.
- [127] J.-L. Liu, Y.-C. Chen, and M.-L. Tong, "Symmetry strategies for high performance lanthanide-based single-molecule magnets," *Chemical Society Reviews*, 2018.
- [128] S. G. McAdams, A.-M. Ariciu, A. K. Kostopoulos, J. P. Walsh, and F. Tuna, "Molecular single-ion magnets based on lanthanides and actinides: Design considerations and new advances in the context of quantum technologies," *Coordination Chemistry Reviews*, vol. 346, pp. 216–239, 2017.
- [129] P. C. Stamp and A. Gaita-Arino, "Spin-based quantum computers made by chemistry: hows and whys," *Journal of Materials Chemistry*, vol. 19, no. 12, pp. 1718–1730, 2009.
- [130] A. Ghirri, A. Candini, and M. Affronte, "Molecular spins in the context of quantum technologies," *Magnetochemistry*, vol. 3, no. 1, p. 12, 2017.
- [131] M. Affronte and F. Troiani, "Potentialities of molecular nanomagnets for information technologies," in *Molecular magnets*, pp. 249–273, Springer, 2014.
- [132] F.-S. Guo, B. M. Day, Y.-C. Chen, M.-L. Tong, A. Mansikkamäki, and R. A. Layfield, "A dysprosium metallocene single-molecule magnet functioning at the axial limit," *Angewandte Chemie International Edition*, vol. 56, no. 38, pp. 11445–11449, 2017.
- [133] S. Thiele, F. Balestro, R. Ballou, S. Klyatskaya, M. Ruben, and W. Wernsdorfer, "Electrically driven nuclear spin resonance in single-molecule magnets," *Science*, vol. 344, no. 6188, pp. 1135–1138, 2014.
- [134] N. Ishikawa, M. Sugita, T. Ishikawa, S.-y. Koshihara, and Y. Kaizu, "Lanthanide double-decker complexes functioning as magnets at the single-molecular level," *Journal of the American Chemical Society*, vol. 125, no. 29, pp. 8694–8695, 2003.

- [135] N. Ishikawa, M. Sugita, and W. Wernsdorfer, "Quantum tunneling of magnetization in lanthanide single-molecule magnets: Bis (phthalocyaninato) terbium and bis (phthalocyaninato) dysprosium anions," *Angewandte Chemie International Edition*, vol. 44, no. 19, pp. 2931–2935, 2005.
- [136] T. Komeda, H. Isshiki, J. Liu, Y.-F. Zhang, N. Lorente, K. Katoh, B. K. Breedlove, and M. Yamashita, "Observation and electric current control of a local spin in a single-molecule magnet," *Nature communications*, vol. 2, p. 217, 2011.
- [137] R. Vincent, S. Klyatskaya, M. Ruben, W. Wernsdorfer, and F. Balestro, "Electronic read-out of a single nuclear spin using a molecular spin transistor," *Nature*, vol. 488, no. 7411, pp. 357–360, 2012.
- [138] H. Konami, M. Hatano, and A. Tajiri, "An analysis of paramagnetic shifts in proton nmr spectra of non-radical lanthanide (iii)-phthalocyanine sandwich complexes," *Chemical Physics Letters*, vol. 160, no. 2, pp. 163–167, 1989.
- [139] N. Ishikawa, "Functional phthalocyanine molecular materials," *Struct Bond*, vol. 135, pp. 211–228, 2010.
- [140] E. Del Barco, A. D. Kent, S. Hill, J. North, N. Dalal, E. Rumberger, D. Hendrickson, N. Chakov, and G. Christou, "Magnetic quantum tunneling in the single-molecule magnet mn 12-acetate," *Journal of Low Temperature Physics*, vol. 140, no. 1-2, pp. 119–174, 2005.
- [141] P. Stamp, "Environmental decoherence versus intrinsic decoherence," *Phil. Trans. R. Soc. A*, vol. 370, no. 1975, pp. 4429–4453, 2012.
- [142] R. Hanson, L. P. Kouwenhoven, J. R. Petta, S. Tarucha, and L. M. Vandersypen, "Spins in few-electron quantum dots," *Reviews of Modern Physics*, vol. 79, no. 4, p. 1217, 2007.
- [143] D. D. Awschalom, R. Epstein, and R. Hanson, "The diamond age diamond age of spintronics," *Scientific American*, vol. 297, no. 4, pp. 84–91, 2007.
- [144] J. J. Morton, D. R. McCamey, M. A. Eriksson, and S. A. Lyon, "Embracing the quantum limit in silicon computing," *Nature*, vol. 479, no. 7373, p. 345, 2011.
- [145] M. Atzori, L. Tesi, E. Morra, M. Chiesa, L. Sorace, and R. Sessoli, "Room-temperature quantum coherence and rabi oscillations in vanadyl phthalocyanine: toward multifunctional molecular spin qubits," *Journal of the American Chemical Society*, vol. 138, no. 7, pp. 2154–2157, 2016.

- [146] F. Troiani, C. Godfrin, S. Thiele, F. Balestro, W. Wernsdorfer, S. Klyatskaya, M. Ruben, and M. Affronte, "Landau-zener transition in a continuously measured single-molecule spin transistor," *Physical review letters*, vol. 118, no. 25, p. 257701, 2017.
- [147] A. Novelli, W. Belzig, and A. Nitzan, "Landau–zener evolution under weak measurement: manifestation of the zeno effect under diabatic and adiabatic measurement protocols," *New Journal of Physics*, vol. 17, no. 1, p. 013001, 2015.
- [148] G. Taran, E. Bonet, and W. Wernsdorfer, "The role of the quadrupolar interaction in the tunneling dynamics of lanthanide molecular magnets," *Journal of Applied Physics*, vol. 125, no. 14, p. 142903, 2019.
- [149] A. Morello and L. De Jongh, "Dynamics and thermalization of the nuclear spin bath in the single-molecule magnet Mn_{12} -ac: Test for the theory of spin tunneling," *Physical Review B*, vol. 76, no. 18, p. 184425, 2007.
- [150] E. Moreno-Pineda, S. Klyatskaya, P. Du, M. Damjanovic, G. Taran, W. Wernsdorfer, and M. Ruben, "Observation of cooperative electronic quantum tunneling: Increasing accessible nuclear states in a molecular qudit," *Inorganic chemistry*, vol. 57, no. 16, pp. 9873–9879, 2018.
- [151] N. Ishikawa, T. Iino, and Y. Kaizu, "Interaction between f-electronic systems in dinuclear lanthanide complexes with phthalocyanines," *Journal of the American Chemical Society*, vol. 124, no. 38, pp. 11440–11447, 2002.
- [152] N. Prokof'ev and P. Stamp, "Theory of the spin bath," *Reports on Progress in Physics*, vol. 63, no. 4, p. 669, 2000.
- [153] W. Yang, W.-L. Ma, and R.-B. Liu, "Quantum many-body theory for electron spin decoherence in nanoscale nuclear spin baths," *Reports on Progress in Physics*, vol. 80, no. 1, p. 016001, 2016.
- [154] A. Morello, "Quantum nanomagnets and nuclear spins: an overview," in *Quantum Magnetism*, pp. 125–138, Springer, 2008.
- [155] S. Tomsovic, *Tunneling in complex systems*, vol. 5. World Scientific, 1998.
- [156] N. Prokof'Ev and P. Stamp, "Low-temperature quantum relaxation in a system of magnetic nanomolecules," *Physical review letters*, vol. 80, no. 26, p. 5794, 1998.
- [157] W. Wernsdorfer, R. Sessoli, and D. Gatteschi, "Nuclear-spin–driven resonant tunnelling of magnetisation in Mn_{12} acetate," *EPL (Europhysics Letters)*, vol. 47, no. 2, p. 254, 1999.

- [158] Y. Furukawa, K. Watanabe, K. Kumagai, F. Borsa, and D. Gatteschi, "Magnetic structure and spin dynamics of the ground state of the molecular cluster $\text{Mn}_{12}\text{O}_{12}$ acetate studied by ^{55}Mn nmr," *Physical Review B*, vol. 64, no. 10, p. 104401, 2001.
- [159] A. Morello, O. N. Bakharev, H. B. Brom, R. Sessoli, and L. J. de Jongh, "Nuclear spin dynamics in the quantum regime of a single-molecule magnet," *Physical review letters*, vol. 93, no. 19, p. 197202, 2004.
- [160] Z. Jang, A. Lascialfari, F. Borsa, and D. Gatteschi, "Measurement of the relaxation rate of the magnetization in $\text{Mn}_{12}\text{O}_{12}$ -acetate using proton nmr echo," *Physical review letters*, vol. 84, no. 13, p. 2977, 2000.
- [161] E. Moreno-Pineda, G. Taran, W. Wernsdorfer, and M. Ruben, "Quantum tunnelling of the magnetisation in single-molecule magnet isotopologue dimers," *Chemical science*, vol. 10, no. 19, pp. 5138–5145, 2019.
- [162] S.-G. Wu, Z.-Y. Ruan, G.-Z. Huang, J.-Y. Zheng, V. Vieru, G. Taran, J. Wang, Y.-C. Chen, J.-L. Liu, L. T. A. Ho, *et al.*, "Field-induced oscillation of magnetization blocking in holmium metallacrown magnet," *arXiv preprint arXiv:2006.04401*, 2020.
- [163] M. N. Leuenberger and D. Loss, "Spin tunneling and phonon-assisted relaxation in Mn_{12} -acetate," *Physical Review B*, vol. 61, no. 2, p. 1286, 2000.
- [164] R. A. Layfield and M. Murugesu, *Lanthanides and actinides in molecular magnetism*. John Wiley & Sons, 2015.
- [165] M. Martínez-Pérez, S. Cardona-Serra, C. Schlegel, F. Moro, P. Alonso, H. Prima-García, J. Clemente-Juan, M. Evangelisti, A. Gaita-Ariño, J. Sesé, *et al.*, "Gd-based single-ion magnets with tunable magnetic anisotropy: molecular design of spin qubits," *Physical review letters*, vol. 108, no. 24, p. 247213, 2012.
- [166] H. Buckmaster and Y. Shing, "A survey of the epr spectra of Gd^{3+} in single crystals," *physica status solidi (a)*, vol. 12, no. 2, pp. 325–361, 1972.
- [167] G. Siu and D. Newman, "Contributions to the ground state splitting of s-state ions. i. the $8s_{7/2}$ state of Gd^{3+} ," *Journal of Physics C: Solid State Physics*, vol. 15, no. 33, p. 6753, 1982.
- [168] D. Goldfarb and S. Stoll, *EPR spectroscopy: fundamentals and methods*. John Wiley & Sons, 2018.
- [169] D. Newman and W. Urban, "Interpretation of s-state ion epr spectra," *Advances in Physics*, vol. 24, no. 6, pp. 793–844, 1975.

- [170] G. Taran, E. Bonet, E. Moreno-Pineda, V. Chibotaru, F. Balestro, M. Ruben, and W. Wernsdorfer, "High resolution anisotropy maps of molecular magnets," 2020, in preparation.
- [171] A. Cornia, A. C. Fabretti, M. Pacchioni, L. Zobbi, D. Bonacchi, A. Caneschi, D. Gatteschi, R. Biagi, U. Del Pennino, V. De Renzi, *et al.*, "Direct observation of single-molecule magnets organized on gold surfaces," *Angewandte Chemie International Edition*, vol. 42, no. 14, pp. 1645–1648, 2003.
- [172] J. Liu, E. del Barco, and S. Hill, "A microscopic and spectroscopic view of quantum tunneling of magnetization," in *Molecular Magnets*, pp. 77–110, Springer, 2014.
- [173] A. L. Wysocki and K. Park, "Nature of hyperfine interactions in tbc2 single-molecule magnets: Multiconfigurational ab initio study," *Inorganic Chemistry*, vol. 59, no. 5, pp. 2771–2780, 2020.
- [174] K. Saito, M. Wubs, S. Kohler, Y. Kayanuma, and P. Hänggi, "Dissipative Landau-Zener transitions of a qubit: Bath-specific and universal behavior," *Physical Review B*, vol. 75, no. 21, p. 214308, 2007.

List of Publications

- [1] G. Taran, E. Bonet, and W. Wernsdorfer, "Molecular magnetism: Single-molecule magnets and molecular quantum spintronics," *Handbook of Magnetism and Magnetic Materials*, pp. 1–31, 2020.
- [2] E. Moreno-Pineda, S. Klyatskaya, P. Du, M. Damjanovic, G. Taran, W. Wernsdorfer, and M. Ruben, "Observation of cooperative electronic quantum tunneling: Increasing accessible nuclear states in a molecular qubit," *Inorganic chemistry*, vol. 57, no. 16, pp. 9873–9879, 2018.
- [3] G. Taran, E. Bonet, and W. Wernsdorfer, "The role of the quadrupolar interaction in the tunneling dynamics of lanthanide molecular magnets," *Journal of Applied Physics*, vol. 125, no. 14, p. 142903, 2019.
- [4] E. Moreno-Pineda, G. Taran, W. Wernsdorfer, and M. Ruben, "Quantum tunnelling of the magnetisation in single-molecule magnet isotopologue dimers," *Chemical science*, vol. 10, no. 19, pp. 5138–5145, 2019.
- [5] G. Taran, E. Bonet, and W. Wernsdorfer, "Decoherence measurements in crystals of molecular magnets," *Physical Review B*, vol. 99, no. 18, p. 180408, 2019.
- [6] G. Taran, E. Bonet, and W. Wernsdorfer, "Thermalization of nuclear spins in lanthanide molecular magnets," *arXiv preprint arXiv:2110.00161*, 2021.
- [7] S.-G. Wu, Z.-Y. Ruan, G.-Z. Huang, J.-Y. Zheng, V. Vieru, G. Taran, J. Wang, Y.-C. Chen, J.-L. Liu, L. F. Chibotaru, *et al.*, "Field-induced oscillation of magnetization blocking barrier in a holmium metallocrown single-molecule magnet," *Chem*, vol. 7, no. 4, pp. 982–992, 2021.
- [8] G. Taran, E. Bonet, E. Moreno-Pineda, V. Chibotaru, F. Balestro, M. Ruben, and W. Wernsdorfer, "High resolution anisotropy maps of molecular magnets," 2021, in preparation.

Acknowledgements

If a PhD would be a sporting discipline, I would say, it's an endurance event, in many ways similar to the 'Tour de France'. By far the most important structure is the 'peloton' as having people 'riding with you' greatly helps to overcome resistance and make progress. It often feels like an adventure, exciting whenever the experiment deviates from one's expectation but also unpredictable and high stacked as a small mistake can make months worth of effort go to waste. Thus, having people to help you avoid the pitfalls and steer you in the right direction is of utmost importance. During my PhD, I was fortunate enough to have encountered such people that both supported and guided me but also encouraged to take risks and enjoy physics.

Most importantly, I want to thank my supervisor, Wolfgang Wernsdorfer, for giving me the opportunity to pursue this PhD program. Doing research with you was a real privilege. Your work ethic and dedication to science always inspired me and gave me the necessary courage to tackle even the most difficult problems. I greatly appreciate the freedom you gave me in pursuing the subjects I found interesting. I'm sure the practices I've learned from you will have a lasting impact on my life.

I'm very grateful to Edgar Bonet with whom I shared an office and whose expertise was invaluable in the progress that I report in this thesis. Your ability to identify the core of the problem and attack it in the most straightforward way never ceased to impress me.

I'm thankful to Franck Balestro who helped me with many administrative and technical issues at the Neel Institute and thus greatly facilitated my work.

I would like to thank Eufemio Moreno-Pineda who is responsible for the synthesis and structural characterization of a number of molecular systems that I investigated during my PhD. I always found our collaborations very productive and engaging. Your persistence and energy definitely helped in the advancing our projects.

I'm grateful to Mario Ruben who provided me with molecular crystals upon which I've built my PhD and who agreed to co-referee this thesis.

I would like to thank all my fellow students in our group who made my trips to Karlsruhe really enjoyable. As a newly formed group, I found all of you full of

energy and ambition. Building the experimental infrastructure from scratch is not a small endeavor but I'm convinced that your results will be greatly rewarding.

I'm deeply grateful to my high school teacher Liliana Alexandru who helped me discover and nurse my passion for physics. Your teaching modeled the way I approach problem-solving and your unconditioned support both through my high school and undergraduate years gave me an example that I'll always try to follow. All my thoughts and prayers are with you my dear teacher as I wish you never-ending power and hope against the disease that you battle at the moment.

There are no good words to express my love and gratitude towards my parents Victoria and Stefan and my sister Anastasia. You made countless sacrifices to help me reach this point in my life. I hope that through this work I make a small testimony of your efforts. Thank you for being there for me and for giving me the courage to always pursue the things I love.

Finally, I'm very grateful to my wife Andriana and my little girl Eliza. Thank you for the patience and understanding with the never-ending workdays and for the invaluable support that you gave me during my entire PhD. The last year, marked by the birth of our little one, was the happiest year of my life. You are my treasures and I'm looking forward to the new adventures that await us in the future.

Karlsruhe, October 2020

Gheorghe Taran

